Appendix A
Supplementary Information

A.1. Data Collections of the B-Form

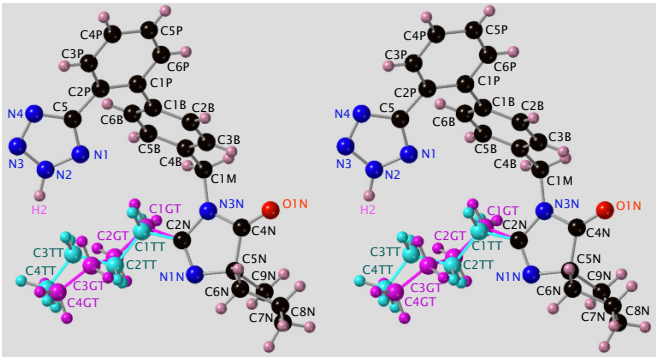

Figure S.1
The atom-numbering for the desmotrope **1**-B.

As examples we describe the X-ray-data collection (DC) at T = 235(1) K (BC5) and the neutron DCs at T = 293(1) K (N31) and at T = 125(1) K (N32) , but the lattice parameters (l.p.s) of all DCs are compiled in the Tables S.1, S.2, S.3, S.5 and S.4.

Let us first explain the abbreviations for the series of data collections used in the main text:

- BC: This series comprises *twelve* DCs at temperatures falling from 300 ↘ 100 K, carried out on the crystal K1, shown in the Figure S.3, using copper radiation, on a RIGAKU SuperNova Dual four-circle diffractometer at ISIC, equipped with an ATLAS CCD-detector, in November 2018 and summarised in the Table S.1.
- BD: This series comprises *nineteen* DCs at temperatures falling from 255 ↘ 90 K, carried out on the crystal K2, shown in the Figure S.4, using copper Kα radiation from a rotating-anode X-ray tube and a mirror (λ=1.54184Å), on a RIGAKU XtaLAB Synergy R, Dual-Wavelength four-circle diffractometer equipped with a Hybrid Pixel Array Detector HyPix-Arc 150, in October 2021 and summarised in the Table S.2.
- BU: This series comprises *seventeen* DCs at temperatures rising from 100 ↗ 260 K carried out on the crystal K2, shown in the Figure S.4, using the same device as for the series BD, in October 2021 and summarised in the Table S.3.
- BN: This series comprises *thirteen* DCs at temperatures falling from 220 ↘ 181 K in steps of 3 K, carried out on the crystal K3, shown in the Figure S.5, using copper Kα radiation from a micro-focus sealed X-ray tube (λ=1.54184Å), performed on a RIGAKU SuperNova Dual four-circle diffractometer at ISIC, equipped with an ATLAS CCD-detector, in November 2020 and summarised in the Table S.5
- BH: This series comprises *four* DCs at temperatures rising from 315 ↗ 360 K in steps of 15 K carried out on the crystal K4, shown in the Figure S.6, using copper Kα radiation from a micro-focus sealed X-ray tube (λ=1.54184Å), performed on a RIGAKU SuperNova Dual four-circle diffractometer at ISIC, equipped with an ATLAS CCD-detector, in January 2021 and summarised in the Table S.4.

Table S.1
The Series of DCs for **1**-B, named BC, for cooling. Measured on Crystal K1. Temperature falling, in steps of 10, 15 or 20 K, from 300 to 100 K, meaning twelve DCs. The phase transition at T_{c_4} = 208 K is indicated by a horizontal, dashed line.

T [K]	*a* [Å]	*b* [Å]	*c* [Å]	α [°]	β [°]	γ [°]	*V* [Å^3]	Time Stamp November2018	Filename IRB_B	CCDC Number
300	9.36842(25)	11.17291(62)	12.185501(78)	112.929(6)	90.788(6)	105.166(5)	1124.16(11)	Sun 18 12 : 28 : 39	_300K	2242176
290	9.35661(47)	11.16836(64)	12.17196(76)	112.897(6)	90.751(4)	105.204(5)	1121.18(11)	Sun 18 15 : 24 : 23	_290K	2242175
275	9.34197(50)	11.15860(70)	12.15460(83)	112.857(6)	90.672(5)	105.262(5)	1117.08(12)	Sun 18 18 : 42 : 04	_275K	2242174
255	9.32297(43)	11.15478(69)	12.13404(81)	112.802(6)	90.632(5)	105.315(5)	1112.80(11)	Sun 18 21 : 27 : 01	_255K	2242173
235	9.3118(33)	11.14876(43)	12.11438(51)	112.771(3)	90.601(3)	105.330(75)	1109.345(75)	Sun 18 23 : 47 : 25	_235K	2242172
215	9.30724(46)	11.14714(65)	12.09336(77)	112.831(6)	90.581(4)	105.339(5)	1106.17(11)	Mon 19 06 : 28 : 56	_215K	2242171
195	9.31952(42)	11.14878(72)	12.01482(6)	114.424(4)	90.636(5)	104.285(5)	1092.41(11)	Mon 19 08 : 55 : 55	_195K	2242170
175	9.31094(55)	11.14220(76)	11.99509(82)	114.7324(17)	90.5817(15)	104.0778(16)	1087.22(3)	Mon 19 11 : 47 : 26	_175K	2242169
155	9.31110(52)	11.13265(67)	11.98190(81)	114.800(6)	90.506(5)	104.144(5)	1084.51(12)	Mon 19 14 : 08 : 03	_155K	2242168
135	9.31054(47)	11.12145(61)	11.96372(85)	114.797(6)	90.427(5)	104.226(5)	1081.46(11)	Mon 19 16 : 33 : 18	_135K	2242167
115	9.305545(62)	11.119292(85)	11.94756(100)	114.818(8)	90.391(6)	104.258(6)	1078.92(14)	Mon 19 18 : 59 : 39	_115K	2242166
100	9.29631(51)	11.10697(70)	11.94009(77)	114.786(6)	90.305(5)	104.316(5)	1076.17(11)	Mon 19 23 : 07 : 25	_100K	2003109

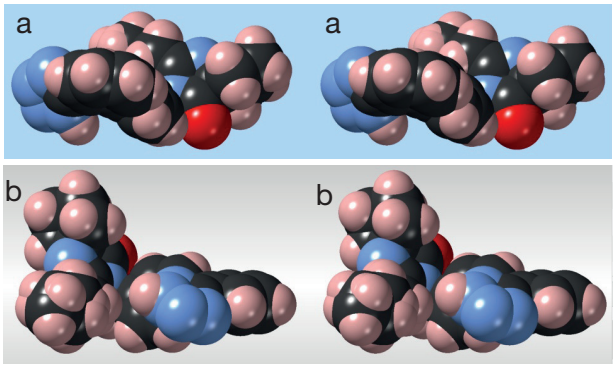

Figure S.2
The van der WAALS envelopes of **1** in the structures **1**-A (a) and **1**-B (b).

Table S.2
First Series of DCs, measured on Crystal K2, for **1**-B, named BD, for down. Temperature falling, in steps of 5 or 10 K, from 255 to 90 K, meaning nineteen DCs. The phase transition at T_{c_4} = 208 K is indicated by a horizontal, dashed line.

T [K]	a [Å]	b [Å]	c [Å]	α [°]	β [°]	γ [°]	V [Å^3]	Time Stamp Year 2021	Filename IRB_B	CCDC Number
255	9.3269(2)	11.1550(2)	12.1311(3)	112.802(2)	90.6081(19)	105.3165(19)	1113.08(4)	Fri Oct 08 16 : 29 : 13	_01_255_00	2243386
245	9.31984(16)	11.1515(2)	12.1237(2)	112.7797(18)	90.6166(15)	105.3379(16)	1111.25(4)	Fri Oct 08 16 : 52 : 11	_02_245_00	2243387
235	9.31590(17)	11.1517(2)	12.1207(2)	112.7857(17)	90.6004(15)	105.3546(16)	1110.41(4)	Fri Oct 08 17 : 15 : 00	_03_235_00	2243388
225	9.30979(17)	11.1493(2)	12.1091(2)	112.7983(17)	90.5892(15)	105.3471(16)	1108.34(4)	Fri Oct 08 17 : 37 : 53	_04_225_00	2243389
215	9.30561(17)	11.1474(2)	12.0957(2)	112.8677(17)	90.5920(15)	105.3016(17)	1106.09(4)	Fri Oct 08 18 : 00 : 56	_05_215_00	2243390
210	9.30514(18)	11.1467(2)	12.0862(2)	112.9725(17)	90.6128(15)	105.2210(17)	1104.62(4)	Fri Oct 08 18 : 21 : 17	_06_210_00	2243391
205	9.3250(3)	11.1516(3)	12.0356(2)	114.166(2)	90.667(2)	104.448(2)	1096.57(5)	Fri Oct 08 18 : 41 : 45	_07_205_00	2243392
195	9.32506(19)	11.1435(2)	12.0155(2)	114.5355(17)	90.6569(16)	104.1712(17)	1092.18(4)	Fri Oct 08 19 : 04 : 52	_08_195_00	2243393
185	9.3221(2)	11.1380(2)	12.0031(2)	114.6696(18)	90.6281(17)	104.1017(19)	1089.40(4)	Fri Oct 08 19 : 27 : 52	_09_185_00	2243394
175	9.3193(2)	11.1331(2)	11.9938(2)	114.7444(18)	90.5947(18)	104.0759(19)	1087.28(4)	Fri Oct 08 19 : 50 : 57	_10_175_00	2243395
165	9.3158(2)	11.1283(2)	11.9852(2)	114.7824(18)	90.5628(18)	104.075(2)	1085.36(4)	Fri Oct 08 20 : 14 : 02	_11_165_00	2243396
155	9.3125(2)	11.1232(2)	11.9765(2)	114.7970(19)	90.5389(19)	104.081(2)	1083.57(4)	Fri Oct 08 20 : 36 : 57	_12_155_00	2243397
145	9.3095(2)	11.1188(2)	11.9692(2)	114.8006(19)	90.5088(19)	104.096(2)	1082.10(4)	Fri Oct 08 20 : 59 : 58	_13_145_00	2243398
135	9.3061(2)	11.1150(2)	11.9617(2)	114.802(2)	90.475(2)	104.117(2)	1080.61(5)	Fri Oct 08 21 : 23 : 02	_14_135_00	2243399
125	9.3032(2)	11.1110(2)	11.9550(3)	114.800(2)	90.446(2)	104.143(2)	1079.22(5)	Fri Oct 08 21 : 46 : 23	_15_125_00	2243400
115	9.2990(2)	11.1049(2)	11.9438(3)	114.780(2)	90.413(2)	104.168(2)	1077.26(5)	Fri Oct 08 22 : 09 : 49	_16_115_00	2243401
105	9.2956(2)	11.1004(2)	11.9369(3)	114.764(2)	90.393(2)	104.193(2)	1075.87(5)	Fri Oct 08 22 : 36 : 00	_17_105_00	2243402
95	9.2958(2)	11.0979(2)	11.9312(3)	114.773(2)	90.3356(19)	104.239(2)	1074.94(4)	Fri Oct 08 23 : 09 : 41	_18_95_00	2243403
90	9.2944(2)	11.0967(2)	11.9282(2)	114.770(2)	90.3172(18)	104.253(2)	1074.38(4)	Fri Oct 08 23 : 39 : 02	_19_90_00	2243404

Table S.3
Second Series of DCs, measured on Crystal K2, for **1**-B, named BU, for up. Temperature rising, in steps of 10 K, from 100 to 260 K, meaning seventeen DCs. The phase transition at T_{c_4} = 208 K is indicated by the dashed line.

T [K]	a [Å]	b [Å]	c [Å]	α [°]	β [°]	γ [°]	V [Å^3]	Time Stamp Year 2021	Filename IRB_B	CCDC Number
100	9.2973(2)	11.1003(2)	11.9349(2)	114.7867(19)	90.3460(18)	104.2266(19)	1075.59(4)	Sat Oct 09 00 : 01 : 59	_20_100_00	2243402
110	9.2995(2)	11.1036(2)	11.9399(2)	114.790(2)	90.3773(18)	104.196(2)	1076.67(4)	Fri Oct 08 17 : 06 : 48	_21_110_00	2246772
120	9.3036(2)	11.1090(2)	11.9515(2)	114.804(2)	90.4118(19)	104.169(2)	1078.66(4)	Fri Oct 08 17 : 29 : 41	_22_120_00	2243400
130	9.3062(2)	11.1131(2)	11.9582(2)	114.812(2)	90.4421(19)	104.143(2)	1079.96(5)	Fri Oct 08 17 : 52 : 39	_23_130_00	2246773
140	9.3085(2)	11.1177(2)	11.9655(2)	114.8147(19)	90.4771(19)	104.113(2)	1081.40(4)	Fri Oct 08 18 : 15 : 33	_24_140_00	2246774
150	9.3118(2)	11.1209(2)	11.9728(2)	114.8009(19)	90.5092(19)	104.095(2)	1082.90(4)	Sat Oct 09 02 : 11 : 15	_25_150_00	2246775
160	9.3143(2)	11.1260(2)	11.9808(2)	114.7937(18)	90.5456(18)	104.081(2)	1084.45(4)	Sat Oct 09 02 : 34 : 05	_26_160_00	2246776
170	9.3176(2)	11.1310(2)	11.9899(2)	114.7652(18)	90.5754(18)	104.075(2)	1086.37(4)	Fri Oct 0819 : 19 : 39	_27_170_00	2246777
180	9.3206(2)	11.1356(2)	11.9987(2)	114.7059(18)	90.6094(17)	104.0845(19)	1088.39(4)	Fri Oct 0819 : 42 : 41	_28_180_00	2246778
190	9.3237(2)	11.1402(2)	12.0093(2)	114.6014(18)	90.6466(17)	104.1302(19)	1090.78(4)	Fri Oct 08 20 : 05 : 49	_29_190_00	2246779
200	9.32499(18)	11.1454(2)	12.0239(2)	114.3838(17)	90.6807(15)	104.2542(17)	1093.98(4)	Fri Oct 08 20 : 51 : 36	_30_200_00	2246780
210	9.30494(18)	11.1474(2)	12.0860(2)	112.9750(17)	90.6183(15)	105.2170(17)	1104.63(4)	Sat Oct 09 04 : 13 : 59	_31_210_00	2246781
220	9.30697(18)	11.1477(2)	12.1042(2)	112.8154(18)	90.5966(16)	105.3281(18)	1107.34(4)	Sat Oct 09 04 : 51 : 35	_32_220_00	2246782
230	9.31223(18)	11.1505(2)	12.1167(2)	112.7859(18)	90.5963(16)	105.3444(17)	1109.55(4)	Sat Oct 09 05 : 14 : 35	_33_230_00	2246783
240	9.31879(18)	11.1533(2)	12.1276(2)	112.7872(18)	90.6106(16)	105.3477(18)	1111.54(4)	Sat Oct 09 05 : 37 : 29	_34_240_00	2246784
250	9.32453(17)	11.1565(2)	12.1374(2)	112.7987(19)	90.6339(15)	105.3293(17)	1113.40(4)	Sat Oct 09 05 : 45 : 45	_35_250_00	2246785
260	9.33354(14)	11.16072(18)	12.1434(2)	112.8045(15)	90.6388(13)	105.3088(14)	1115.51(3)	Sat Oct 09 06 : 23 : 29	_36_260_00	2246786

Table S.4
The Series of DCs in **1**-B, named BH, for high. Measured on Crystal K4. Temperature rising, in steps of 15 K, from 315 to 360 K, meaning four DCs.

T [K]	a [Å]	b [Å]	c [Å]	α [°]	β [°]	γ [°]	V [Å^3]	Time Stamp Year 2021	Filename Up − ML −4− IRB_B	CCDC Number
315	9.37811(32)	11.17472(42)	12.19388(54)	112.9983(39)	90.8457(32)	105.1059(31)	1125.860(76)	Mon Jan 04 21 : 00 : 54	_315K	2225692
330	9.39646(45)	11.17809(60)	12.19435(77)	112.9755(57)	90.9302(45)	105.3418(13)	1128.82(11)	Mon Jan 04 23 : 13 : 17	_330K	2225693
345	9.40722(49)	11.17966(63)	12.21969(87)	113.0355(63)	90.9921(49)	104.9547(48)	1132.45(12)	Tue Jan 05 01 : 25 : 21	_345K	2225694
360	9.43097(55)	11.18972(68)	12.23021(88)	113.1165(65)	91.0491(53)	104.9119(54)	1136.66(13)	Tue Jan 05 08 : 51 : 33	_360K	2225695

Table S.5
Third Series of DCs for **1**-B, named BN, for narrow. Measured on Crystal K3. Temperature falling, in steps of 3 K, from 220 to 181 K, meaning fourteen DCs. The phase transition at T_{c_4} = 208 K is indicated by the horizontal, dashed line. Also keep in mind that only the DCs at 181, 190 and 211 K were normally long DCs.

T [K]	a [Å]	b [Å]	c [Å]	α [°]	β [°]	γ [°]	V [Å^3]	Time Stamp November 2020	Filename re–IRB_B	CCDC Number
220	9.3031(32)	11.1424(38)	12.0944(45)	112.816(34)	90.5691(29)	105.336(30)	1105.49(68)	Thu 05 11 : 36 : 37	−220K	
217	9.302(3)	11.142(4)	12.089(5)	112.81(4)	90.59(3)	105.33(3)	1104.9(7)	Thu 05 11 : 56 : 37	−217K	
214	9.302(3)	11.145(4)	12.083(5)	112.84(4)	90.58(3)	105.31(3)	1104.4(7)	Thu 05 12 : 15 : 24	−214K	
211	9.2956(5)	11.1436(6)	12.0790(6)	112.867(5)	90.611(4)	105.261(5)	1103.2(1)	Thu 0512 : 41 : 37	−211K	2242179
208	9.3267(63)	11.152(11)	12.0852(84)	113.239(77)	90.645(62)	105.186(71)	1105(2)	Thu 05 14 : 47 : 40	−208K	
205	9.3195(33)	11.1454(44)	12.02712(44)	114.18(4)	90.727(29)	104.373(36)	1094.7(8)	Thu 05 14 : 59 : 38	−205K	
202	9.3218(31)	11.1407(37)	12.0194(51)	114.271(36)	90.680(30)	104.250(28)	1093.82(69)	Thu 05 15 : 19 : 25	−202K	
199	9.3236(34)	11.1410(39)	12.0107(52)	114.361(38)	90.679(33)	104.220(31)	1092.62(73)	Thu 05 15 : 32 : 33	−199K	
196	9.3222(23)	11.1488(57)	12.0061(53)	114.432(46)	90.649(27)	104.262(31)	1091.96(78)	Thu 05 15 : 50 : 18	−196K	
193	9.3219(34)	11.1364(36)	12.0048(49)	114.542(35)	90.657(31)	104.136(30)	1090.27(69)	Thu 05 16 : 06 : 32	−193K	
190	9.31898(39)	11.13980(47)	12.00281(58)	114.6151(45)	90.6311(37)	104.1773(36)	1089.23(8)	Thu 05 16 : 34 : 14	−190K	2242178
187	9.31783(32)	11.13537(36)	11.995987	114.7880(19)	90.5233(16)	104.0837(17)	1083.63(4)	Thu 05 18 : 53 : 41	−187K	
184	9.3143(30)	11.1315(33)	11.9922(50)	114.660(34)	90.610(23)	104.087(27)	1087.08(66)	Thu 05 19 : 06 : 47	−184K	
181	9.3165(4)	11.1346(5)	11.99078(59)	114.7039(45)	90.5957(36)	104.1511(36)	1086.756(83)	Thu 05 19 : 29 : 33	−181K	2242177

A..1.1. The B-Form at 235K. A colourless prism-shaped crystal of dimensions 0.57 ×0.16 × 0.06 mm^3 was glued onto a KAPTON shovel. BRAGG-intensities were collected using a RIGAKU SuperNova dual diffractometer system equipped with an Atlas CCD detector and an OXFORD CRYOSTREAM operating at T = 235(1) K. The habit of the measured crystal consisted of the {001} and {02$\bar{1}$} pinacoids and the (10$\bar{1}$), (2$\bar{2}$1), ($\bar{2}$01) and ($\bar{1}\bar{1}$1) pedia. These compare quite nicely - in view of the high background and bad illumination - with the habitus computed by Taulelle et al. in CG&D (2009) who found {001}, {10$\bar{1}$}, {010} and {01$\bar{1}$} on a crystal grown by a temperature gradient from EtOH/water (80 : 20 wt%).

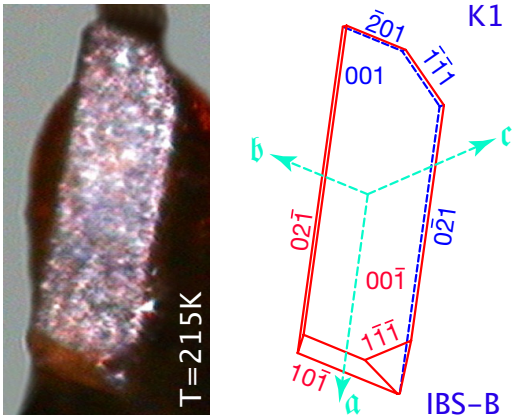

Figure S.3
A photograph and the habitus (Shape, 2011) of the crystal K1 of 1-**B** which was used for the first data collections in 2018.

Data were measured as ω scans using CuKα radiation. The total number of runs and images was based on the strategy calculation from the program ***CrysAlis***^{Pro} (Rigaku, V1.171.40.20a, 2018). The maximal resolution achieved was θ = 76.579°(0.792564 Å) and the maximal resolution of the full sphere was 0.83 Å. All but one of the 4612 maxima located on the frames could be indexed by the cell given in the Table above, which shows that the measured crystal was an SDS. The total number of runs and images was based on the strategy calculation from the program ***CrysAlis***^{Pro} (Rigaku, V1.171.40.20a, 2018) and the unit cell was refined using ***CrysAlis***^{Pro} (Rigaku, V1.171. 40.20a, 2018) on 7002 reflections, 50% of the observed reflections.

Data reduction, scaling and absorption correction were performed using ***CrysAlis***^{Pro} (Rigaku, V1.171.40.20a, 2018). The final completeness is 100.00% out to 76.579° in θ. A Gaussian absorption correction was performed with the help of ***CrysAlis***^{Pro} (1.171.40.20a, Rigaku Oxford Diffraction, 2018). The numerical absorption correction was based on Gaussian integration over a multifaceted crystal model using spherical harmonics as implemented in the SCALE3 ABSPACK scaling algorithm. The absorption coefficient μ of this material is 0.650 mm^{-1} at this wavelength (λ = 1.542Å) and the minimum and maximum transmissions are 0.548 and 1.000.

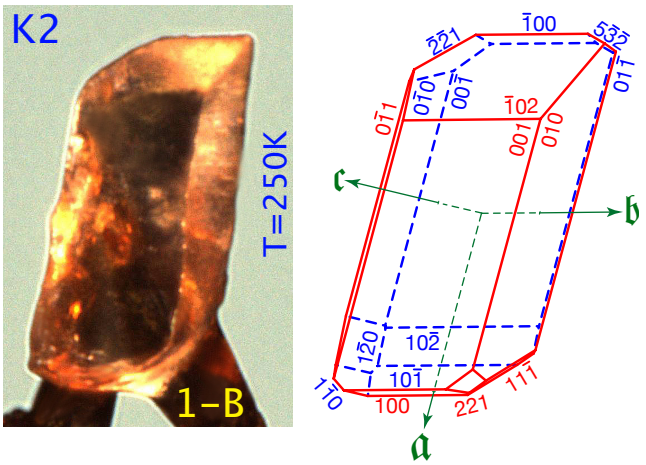

Figure S.4
A photograph and the habitus (Shape, 2011) of the crystal K2 of **1**-B which was used for the Series of Data Collections BD and BU. The pinacoid {100} is more likely due to faulty growth and approximations in the indexing rather than to physical reasons. Indeed, the desire to provide a snug fit of the polyhedron to the crystal sometimes leads to somewhat adventurous face-indices.

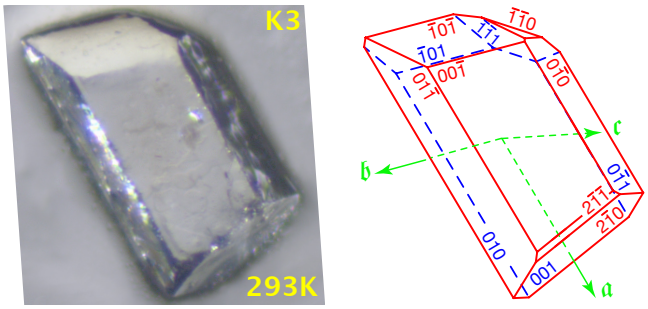

Figure S.5
A photograph (Zeiß STEMI 508) and the habitus (FaceIt, 2016; Shape, 2011) of the crystal K3 of **1**-B which was used for finer data collections around the phase transition, *i.e.* the Series of Data Collections BN.

Figure S.6
Photograph and habitus (Shape, 2011) of the crystal K4 of the desmotrope **1**-B at T = 315 K. Red indices indicate front-faces, blue ones back-faces. This crystal was used for the Series of Data Collections BH.

The structure was solved and the space group $P\bar{1}$ (#2) determined by the **ShelXT** (Sheldrick, 2015) structure solution program and refined by full matrix least squares on $|F|^2$ using version 2018/3 of **ShelXL** (Sheldrick, 2015). There is a single molecule in the asymmetric unit, which is represented by the reported sum formula. In other words: Z is 2 and Z' is 1. All non-hydrogen atoms were refined anisotropically. Most hydrogen atom positions were calculated geometrically and refined using the riding model, but some hydrogen atoms, such as the H2 on the tetrazole, were refined freely (d(N2-H2)=1.003(29)Å, U=0.087(9)Å^2).

After having refined anisotropically all atoms, but those of the n-butyl chains, the four strongest residuals clearly indicated a chain in the *all-trans* conformation. After refining this, the four strongest residuals, again, revealed another n-butyl chain, but in G$^+$T conformation. SADI (σ=0.005) restraints between corresponding bonds were necessary to confine the bond-lengths to acceptable values. But other than that the refinement was stable and did not require any further constraints nor restraints. Site occupancy factors of 0.700(5) and 0.300(5) for the TT and the G$^+$T chains were refined (Table S.6).

In the Figures S.12 and S.13 some more typical crystals of **1**-B are shown for completeness.

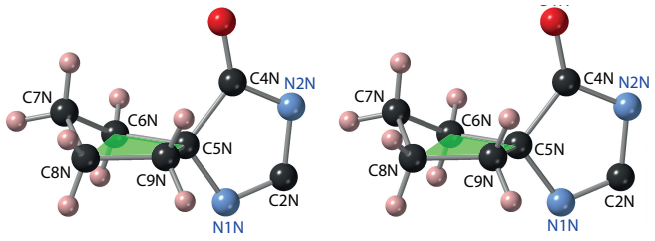

Figure S.7
The envelope of the cyclopentyl-ring in the desmotrope **1**-B. The green least-squares plane is $(173, 85, 271) \approx (213)$ with a deviation of $\Delta \approx 1^\circ$ and an RSS of 0.00324Å^2. The atom C7N lies +0.6295Å above this plane (in the direction of the plane normal **h**). (From the data collection BD1 at T=300K.)

A..1.2. The Neutron Experiment of the B-Form at 293K and 125K. Neutron experiments were carried out at the high flux reactor of the Institut Laue-Langevin (ILL, Grenoble), using the **V**ery- **I**ntense **V**ertical- **A**xis **L**aue **D**iffractometer (VIVALDI) situated at the end of the thermal-neutron-guide H22, constructed to serve submillimetric single crystal neutron diffraction. A detailed description of this instrument may be found in (McIntyre *et al.*, 2006) and more recent information in (Piltz, 2018). The crystals for the neutron diffraction experiments were most likely grown from hot, acid (pH=2) water (possibly seeded). Three crystal were studied altogether; the first two, N1 and N2, were glued to a thin, appropriately folded aluminum foil by means of KWIKFIL-glue and then fixed to a goniometer head, while the third one, N3, shown in the Figure S.8, was enveloped in PARATONE-oil and then mounted on a goniometer head. Diffracted neutrons were detected by image plates of the Niimura Special White series by Fuji. After a careful alignment of the instrument, the samples were then

fixed on appropriate thin Vanadium sticks, mounted on the vertical rotation φ-axis of the instrument and then cooled down to various temperatures provided by the much copied and envied orange cryostat conceived and constructed by Dominique Brochier and Serge Pujol (Brochier & Pujol, 1977).

Table S.6
Crystal Data of **1**-B, Space group is $P\bar{1}$, Z=2.

	T [K]	a [Å]	b [Å]	c [Å]	α [°]	β[°]	γ[°]	V [Å^3]	TT/G$^+$T-Ratio	Wavelength [Å]
B11	125	9.313(2)	11.123(2)	11.962(2)	114.82(3)	90.36(3)	104.21(3)	1081.7(5)	0.000/1.000	MoKα
B12	231	9.315(2)	11.159(2)	12.113(2)	112.81(3)	90.58(3)	105.34(3)	1110.3(5)	0.648(6)/0.352(6)	MoKα
B13	293	9.373(2)	11.180(2)	12.200(2)	112.90(3)	90.77(3)	105.19(3)	1126.9(4)	0.726(5)/0.274(5)	MoKα
Böcs	293	9.366(4)	11.170(5)	12.181(4)	112.92(3)	90.75(4)	105.24(4)	1122.9 (8)	0.659(12)/0.341(12)	CuKα
BC1	300	9.3684(4)	11.1729(6)	12.1855(8)	112.929(6)	90.788(5)	105.166(5)	1124.16(12)	0.727(4)/0.273(4)	CuKα
BC2	290	9.3566(5)	11.1684(6)	12.1720(8)	112.897(6)	90.751(5)	105.204(5)	1121.18(12)	0.724(4)/0.276(4)	CuKα
BC3	275	9.3420(5)	11.1586(7)	12.1546(8)	112.857(6)	90.672(5)	105.261(5)	1117.08(13)	0.721(4)/0.279(4)	CuKα
BC4	255	9.3230(4)	11.1548(7)	12.1340(8)	112.802(6)	90.632(5)	105.315(5)	1112.80(13)	0.711(4)/0.289(5)	CuKα
BC5	235	9.3119(3)	11.1488(4)	12.1144(5)	112.771(4)	90.601(3)	105.330(3)	1109.34(8)	0.688(4)/0.312(4)	CuKα
BC6	215	9.3072(5)	11.1471(6)	12.0934(8)	112.831(6)	90.581(5)	105.339(5)	1106.16(12)	0.637(6)/0.363(6)	CuKα
BC7	195	9.3195(4)	11.1488(7)	12.0148(7)	114.424(6)	90.636(4)	104.285(5)	1092.41(12)	0.151(4)/0.849(4)	CuKα
BC8	175	9.3109(5)	11.1422(8)	11.9951(8)	114.680(7)	90.558(5)	104.175(6)	1087.43(14)	0.060(4)/0.940(6)	CuKα
BC9	155	9.3111(5)	11.1326(7)	11.9819(8)	114.800(6)	90.506(5)	104.144(5)	1084.51(13)	0.027(3)/0.973(3)	CuKα
BC10	135	9.3105(5)	11.1214(6)	11.9637(9)	114.797(6)	90.427(5)	104.226(5)	1081.46(12)	0.018(3)/0.982(3)	CuKα
BC11	115	9.3055(6)	11.1193(9)	11.9476(10)	114.818(8)	90.391(6)	104.258(6)	1078.92(16)	0.014(3)/0.986(3)	CuKα
BC12	100	9.2963(5)	11.1070(7)	11.9401(8)	114.786(6)	90.305(5)	104.317(5)	1076.17(13)	0.014(3)/0.986(3)	CuKα
BH4	360	9.4310(6)	11.1897(7)	12.2302(9)	113.117(7)	91.049(5)	104.912(5)	1136.66(14)	0.737(5)/0.263(5)	CuKα

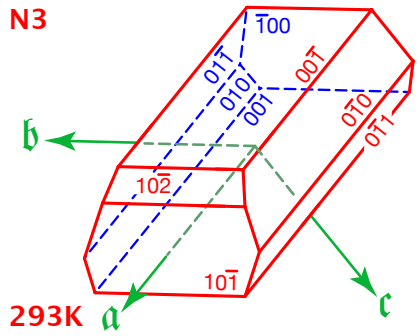

Figure S.8
The habitus of the crystal N3 *as* determined, at RT, on a Stoe IPDS-II with MoKα radiation. Lattice parameters of **1**-B were 11.207(9), 12.233(15), 9.399(13)Å, 90.91(9), 104.60(8) and 113.39(8)°. *Note*, that the orientation of these axes is different from that used elsewhere in the text, but the indices shown were transformed to these latter axes. Red indices indicate front faces, blue ones back faces. This crystal of which the dimensions were 0.68 × 0.344 × 0.20 mm, was used for the data collections N31 and N32.

Neutron beam collimation was fixed at 3 mm in diameter to achieve a homogeneous illumination fo crystals. During data collection, the crystal was stationary and the incident white neutron beam had wavelengths between 0.8 and 5.2 Å. Due to the small volume of the crystal, frames were exposed for 2 hours each. Ten frames were collected every 20 ° in φ in order to achieve good reciprocal space coverage as well as an adequate redundancy of equivalent reflections. Patterns were indexed using the program LAUEGEN by (Campbell, 1995; Campbell *et al.*, 1998) and the reflections were integrated using the program ARGONNE BOXES by (Wilkinson *et al.*, 1988) which uses a two-dimensional version of the 3D (I)/I algorithm by (Lehmann & Larsen, 1974) The wavelength dependent intensities were then normalised to a constant incident wavelength using the program LAUENORM by (Campbell *et al.*, 1986). Correction for absorption was deemed unnecessary in view of the small sample volume. The centring and calibration of the instruments were done by means of carbon tetraboride. The lattices parameters for the neutron data collections were taken from the X-ray data collections B11 for 125 K (Table S.6) and BC2 for 290 K (Table S.1).

Then the crystal N3 was heated to room temperature for a refill and the diffraction spots were seen to be no longer split. We, therefore, carried out another data collection, named N31, at this temperature (possibly using a different goniometer head). The data-set N31 was obtained, at T = 293 K, from ten images exposed for 13440 s each (CCDC-number 2248264). The lattice parameters for N31 were taken from the X-ray data-set at T = 290 K, BC2, (Table S.6).

After the whole molecule of **1** minus the *n*.b.c.s had been refined anisotropically (R_1 = 0.266), the four strongest residuals in a difference-map (between 2.4 and 4.2 eÅ^{-3}) revealed an *all-trans n*-butyl-chain lying roughly in π_{Imi}, the plane of the imidazole. Refining this chain isotropically without imposing any restrictions led to R_1 = 0.207; the positions of the residuals were stable, but corresponded to C—C distances lying between 1.41 and 1.57Å.

After two crystals of **1**-B had been cooled down to T = 125 K from r.t. and shown splitting of diffraction spots at different temperatures, the third crystal, named N3 and shown in the Figure S.8, was enveloped in PARATONE-oil, put inside the cryostat at T = 240 K and then ruthlessly/mercilessly/rapidly cooled down to T = 125 K. A second orientation or twin was seen in the images, but we nevertheless carried out a data collection.

This data-set N32, at T = 125 K, consists of ten images exposed for 7200 s each (CCDC-number 2248263). Two hundred

degrees of reciprocal space were covered in steps of 20° in this way. The lattice parameters for N32 were taken from the X-ray data-set B11 (Table S.6).

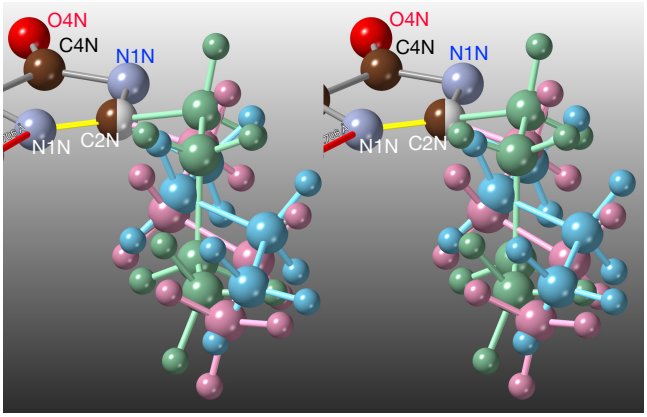

Figure S.9
The three chains-conformers of **1**-B found in the data collection N31 (mauve is T1, turquoise T2 and green GT); occupations numbers are 0.477(19), 0.300(19) and 0.224(10)), respectively.

Another difference-map then revealed that three strongest maxima (between 1.4 and 2.1 $eÅ^{-3}$) indicated the presence of another conformer, namely a $G^{+}T$ one (green in Figure S.9), lying roughly perpendicular to the TT one (mauve in said figure). The last atom appeared in a further difference-map. Again, this chain showed a stable convergence to $R_1 = 0.182$. Afterwards, another difference-map revealed yet another conformer of the *n*.b.c., this being another *all-trans* one (the three conformers are shown in the Figure S.9). Although not strictly necessary, the final refinement was carried out by some restraints, namely DFIX 1.54 0.03, DANG 0.04, SIMU 0.01 0.02 and SUMP 1 0.001. All methyl groups were allowed to rotate about their C—C bond and the C—H were allowed to shrink or extend (AFIX 138). Under these conditions the refinement, based on $|F|^2$, converged to $R_1 = 0.153$, and the occupation numbers: 0.477(19), 0.300(19) and 0.224(10) for the first and second *all-trans* and the *gauche* chains, respectively.

The diffraction pattern at T = 125 K presents split diffraction spots. These might be due to (i) the coexistence of both phases I and II, or (ii) a crack generated during the I⟶II transition and a block of crystal being slightly warped out its normal orientation. After the crystal had been re-heated up to room temperature (r.t.), the splitting of its spots disappeared. Since in none of our numerous X-ray diffraction patterns we had observed a superposition of the diffraction patterns of phases I and II, and since the transition had been shown to be perfectly *reversible* we rule out the possibility (i). The sophisticated neutron-cryostat clearly provides a more homogeneous and stabler environment than the nitrogen-flow used for X-ray diffraction. Notwithstanding this advantage, we lean towards possibility (ii), since we had observed such a phenomenon in the series BD of X-ray data collections. Indeed, we noticed that a not so negligible piece of crystal had simply disappeared. But the diffraction patterns kept being ever so pure. This mechanism might be favoured by the use of a seed-crystal for crystal-growth. But we need to remember that the splitting of the spots had completely disappeared upon heating up again to r.t. In order to gain confidence in this conclusion it will be necessary to index the second individuum at low temperature.

The data collection N31 was carried out at r.t.; it is the only one showing three conformers for the *n*.b.c. This may be due to the sheer size of the crystal and to a more pronounced domain-structure acquired the cooling and heating process, or to a slower dynamics of the conversion of confomers inside the more powerful cryostat. In any case, the Figure S.9 shows the *all-trans* conformers to be very similarly located. Furthermore, their occupation numbers add up to 0.78 and are, therefore, quite close to 3:1 found in the X-ray measurements.

On a more positive side, N31 furnishes precious information about the hydrogen atoms, such as a N2—H2 distance of 1.09(3)Å (note that this atoms was refined anisotropically and freely). Some distances and angles are compared in the Table S.7. We are happy to see that most everything is as expected, only better. Let us finally emphasize that the collection N31 looks quite trustworthy, despite a relatively small number of reflections and some experimental difficulties. Let us emphasise once more that no split reflections were observed at r.t. This is another strong indication of the reversibility of the II⟶I phase transition.

If we wish to have a closer look at some distances in the phase II at T = 125 K, it is fair to first, at least partly, list the restraints and constraints which were necessary to reach convergence of the least-squares procedure. Indeed, we had to use RIGU 0.006 0.006 $C, RIGU 0.006 0.006 C4N O1N and ISOR 0.006 0.012 for thirteen hydrogen atoms. In view of the data quality this is a rather modest number and they all mainly concern the U^{pq} components. A discussion of distances and angles should therefore not be thwarted by these subsidiary conditions. We find the following average-values: $C_{aromatic} - H = 1.094(9)Å$, $C_{methyl} - H_3 = 1.097(16)Å$, $C_{methylene} - H_2 = 1.096(20)Å$ and $N - H = 1.12(2)Å$. We may conclude that - despite the slightly suboptimal data collections - all C-H distances lie well within the ballpark staked out by the Union in the IT, Vol C, namely 1.083(11), 1.059(30), 1.092(13) and 1.009(19)Å. This certainly enhances our confidence in this measurement. On the other hand, the N-H distance is clearly bigger than the other ones reported. But in view of the special rôle of the N2-H2···O1N hydrogen bond, we do not take this as an error, but rather as a valuable piece of information. The atoms forming rings do also naturally lie on one plane to rather low sum of squares error. An interpretation of the ADPs would be more than questionable, unfortunately.

A..1.3. Powder Experiments on 1-B The synchrotron-radiation powder-experiments were obtained from the beamline ID31 at the ESRF in Grenoble, France, in two independent sessions. Two powders were investigated: a generic one from the production line (IN952_S13) and another one prepared to resemble the powder used for the SS NMR study as much as possible (IRBB_RMN). The sample IN952_S13 was measured in 2019

on beam-line ID31 and the powder IRBB_RMN in 2013 on the same beam-line.

Figure S.11 shows that the profiles of the reflections were quite regular indeed (*i.e.* narrow, symmetrical and homogeneous). The profiles were treated with the Jana2006 programs, using roughly four dozens of parameters in each case and reaching quite respectable R_{wp}-values. First, a good background was determined with the help of Chebychev-polynomials and then overlapping intensities were divided according to LeBail's algorithm and then the profile and lattice parameters were refined by a Le Bail-procedure. The resulting l.p.s are compiled in Table S.8. The refinements proceeded without any complication whatsoever, quite opposed to those on **1**-A. In view of the excellent agreement of the results from single crystals and powders, a Rietveld-refinement was judged unnecessary.

A comparison of the l.p.s from powders and single crystals reveals some minor inconsistencies between the values. This may be due to the not so trivial temperature-control in a capillary filled with powders. This hypothesis is somewhat supported by the fact that these inconsistencies are less pronounced at room temperature.

Table S.7
Hydrogen bonds (normalised for X-rays, unless H2 refined) and for neutrons in **1**-B (Å, °).

	T [K]	D − H···A	D − H	H···A	D···A	∠D − H···A	PBC/HB
X	116	N2 − H2···N1N^{j1}	1.01(2)	1.73(2)	2.7282(19)	168(2)	v_1 = [312]
N	125	N2 − H2···N1N^{j1}	1.12(2)	1.620(18)	2.730(9)	168.7(10)	v_1 = [312]
X	215	N2 − H2···N1N^{j1}	0.99(2)	1.79(2)	2.7685(17)	169(2)	v_1 = [312]
N	293	N2 − H2···N1N^{j1}	1.09(3)	1.71(2)	2.778(10)	167.6(13)	v_1 = [312]
X	116	C1M − H1MB···N4^{j2}	0.99	2.62	3.592(2)	168.2	v_5 = [1$\bar{1}\bar{2}$]
N	125	C1M − H1MB···N4^{j2}	1.102(10)	2.518(10)	3.590(7)	164.1(9)	v_5 = [1$\bar{1}\bar{2}$]
X	215	C1M − H1MB···N4^{j2}	1.089	2.584(8)	3.65(1)	165.0	v_5 = [1$\bar{1}\bar{2}$]
N	293	C1M − H1MB···N4^{j2}	1.06(3)	2.63(2)	3.655(10)	161.3(10)	v_5 = [1$\bar{1}\bar{2}$]
X	116	C6P − H6P···O1N^{j3}	1.089	2.404(1)	3.280(2)	136.4(1)	v_2 = [011]
N	125	C6P − H6P···O1N^{j3}	1.097(11)	2.373(12)	3.270(8)	137.7(9)	v_2 = [011]
X	215	C6P − H6P···O1N^{j3}	0.99	2.455(1)	3.285(2)	147.3(1)	v_2 = [011]
N	293	C6P − H6P···O1N^{j3}	1.055(19)	2.338(21)	3.286(18)	148.7(*E*)	v_2 = [011]

Symm. Ops : **j1** −x, 1 − y, 1 − z **j2** 1 − x, 1 − y, 1 − z **j3** 1 − x, 2 − y, 2 − z

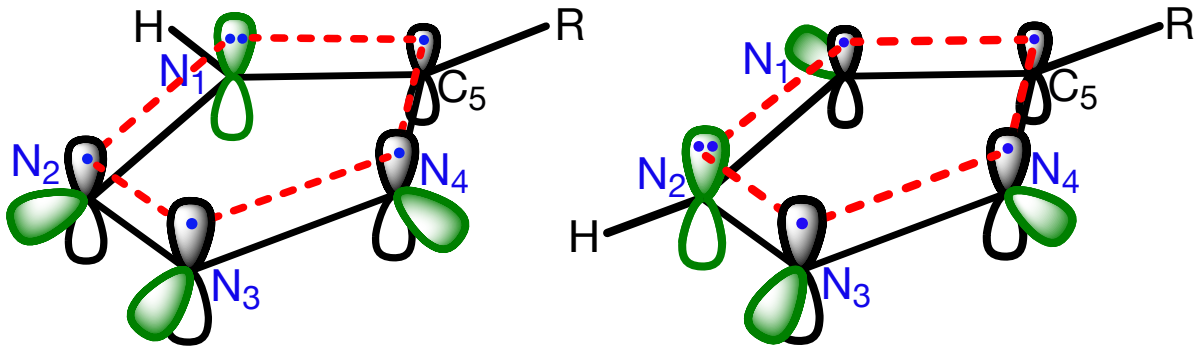

Figure S.10
The hybridisation of the nitrogens of the tetrazole-ring in the desmotropes **1** (**1**-A left, **1**-B right). All N are sp^2 + one lone pair (green); for all but the one carrying the proton, the lone pairs lie in the tetrazole-plane (in one of the sp^2-orbitals, actually). The one perpendicular to said plane participates in the π-system (dashed red), completing 4n+2 electrons ⟶ aromaticity (HÜCKEL).

But in any case the results from the powders do confirm that the single crystals investigated are typical for said powders.

Table S.8
The lattice parameters of **1**-B from synchrotron-radiation powder-diagrams compared to their crystallin counterparts (single crystal*).

$T[K]$	a	b	c	α	β	γ	*Volume*	*Method*	R_{wp}/ $wR(F^2)$	$\lambda[Å]$	*Échantilon*
100	9.31070(7)	11.11724(10)	11.95241(13)	114.7780(8)	90.3817(8)	104.2313(7)	1080.325(17)	*Jana*/*LeBail*	0.0602	1.0	*S*13_002
100	9.31072(8)	11.11726(11)	11.95244(13)	114.7780(8)	90.3818(8)	104.2313(7)	1080.333(18)	*Jana*/*LeBail*	0.0574	1.0	*S*13_003
100*	9.29631(51)	11.10697(70)	11.94009(77)	114.786(6)	90.305(5)	104.316(5)	1076.17(11)	*Olex*2	0.0462	*CuKα*	2003109
293	9.36596(8)	11.17217(10)	12.18398(11)	112.9163(5)	90.7704(6)	105.1819(6)	1123.708(24)	*Jana*/*LeBail*	0.0880	0.8	*RMN*
293	9.37522(30)	11.17918(37)	12.19926(41)	112.9496(14)	90.8273(14)	105.1183(13)	1126.879(102)	*Jana*/*LeBail*	0.0824	1.0	*S*13_002
293	9.37461(10)	11.17838(12)	12.19844(16)	112.9497(10)	90.8267(9)	105.1181(8)	1126.652(23)	*Jana*/*LeBail*	0.0707	1.0	*S*13_003
290*	9.35661(47)	11.16836(64)	12.17196(76)	112.897(6)	90.751(4)	105.204(5)	1121.18(11)	*Olex*2	0.0452	*CuKα*	2242175

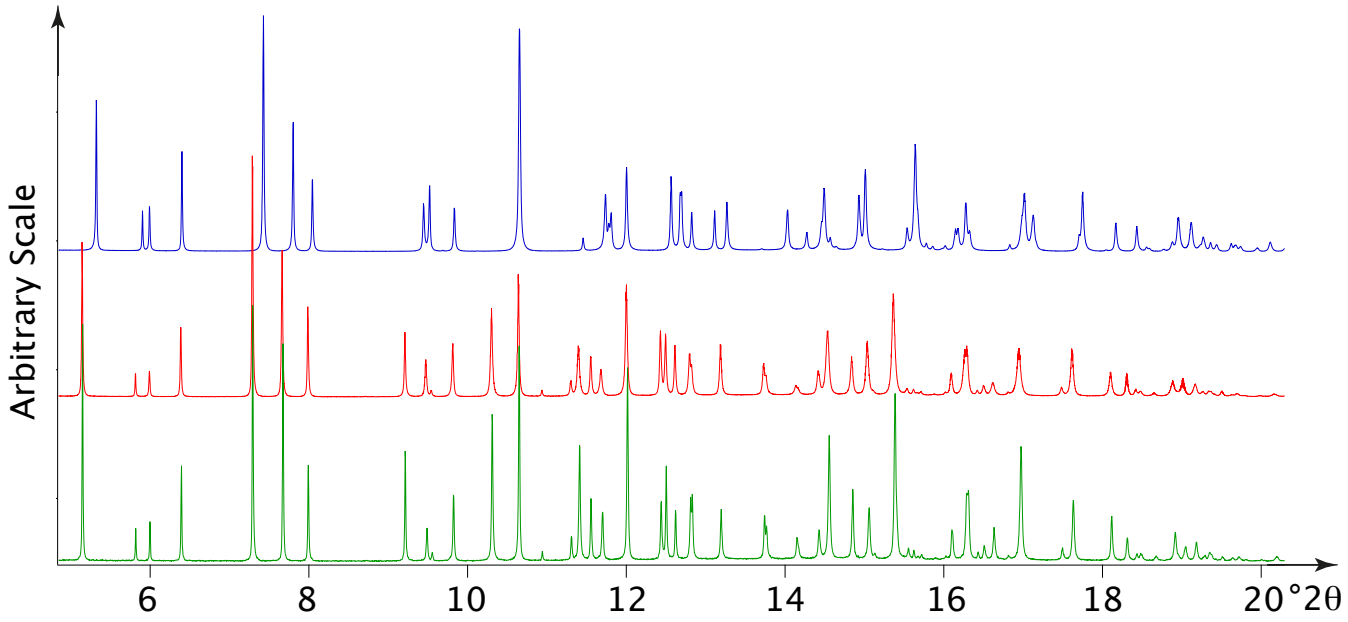

Figure S.11
The powder diagrams IN952_S13_irb_002_100K (λ = 1.0Å, blue) IN952_S13_irb_002_293K (λ = 1.0Å, red) and IRBB_RMN_293K (λ = 0.8Å, green, converted to λ = 1.0Å. Low angle region.

A..1.4. The Habiti of the B-Form. The very existence of columnar and tabular habiti growing from the same mother liquor (Garcia, 2000) had already indicated that the nucleation and growth of crystals **1**-B is a rather delicate matter. For our use we grew columnar crystals from hot acidic water, namely H1, H2, K3 and N3 of which the habiti are presented in Figures S.12, S.13, S.5 and S.8. In Table S.12 we give a summary of the effect of solvents. Albeit, all these crystals look quite different, every one of them contained the zone [100]= ($\{010\}, \{001\}, \{01\bar{1}\}$) predicted by the BFDH-model, as computed by the Mercury (Macrae *et al.*, 2006) program.

The situation is different for the zones [010]=($\{001\}$, $\{10\bar{1}\}$, $\{100\}$) and [001]=($\{100\}$, $\{010\}$, $\{1\bar{1}0\}$). Most of these pinacoids were at least partially observed on one crystal or another. Yet the dominant $\{100\}$ pinacoid of the BFDH-habitus was never observed, instead the $\{10\bar{1}\}$ pinacoid is prominent in our crystals. But the angle between these two faces is small enough for the latter face to still be the result of a layer-wise growth with some perturbations of various parameters during growth in a hot and churning liquid. The preponderance of the [100]-zone might therefore rather be due to this layer-wise growth and the weakest interactions along $\mathbf{a}^*$ than to a classical growth according to PBCs. In some crystals we also observed faces of which the indices were permuted with respect to BFDH, *e.g.* (110), (101), $(1\bar{1}\bar{1})$, or altogether different, *e.g.* $(\bar{1}02)$ or $(11\bar{1})$ which were all not predicted by BFDH (Bravais, 1866; Friedel, 1907; Donnay & Harker, 1937).

A..1.5. The Use of Resonance Structures for 1-B Since the tetrazole moiety (Figure S.10) in this desmotrope is governed by numerous, weak and ill-defined interactions affecting the geometry of the tetrazole, we add another representation for the convenience of the reader (Figure S.14).

In his «The Nature of the Chemical Bond» Linus Pauling shows that one can obtain quite impressive estimates of the bond lengths in complicated aromatic molecules from a graph of verified bond lengths plotted versus the corresponding bond number. This plot is based on the double-bond character of the bonds in benzene as derived from the two Kekulé-structures

representing benzene; this character is $\frac{1}{2}$ for every bond in this molecule, and it can be derived in the same manner for more complicated aromatic molecules.

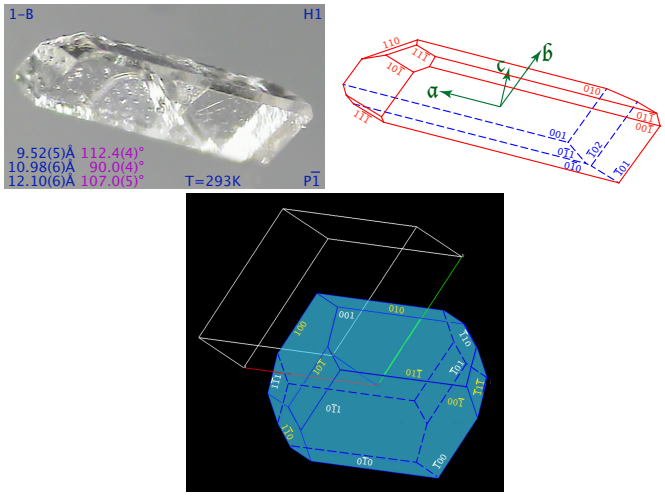

Figure S.12
Photograph, habitus (FaceIt, 2016; Shape, 2011) of the crystal H1 at T = 293 K and the BFDH-morphology (Macrae *et al.*, 2006) of the desmotrope **1**-B. Yellow or red indices indicate front-faces, white or blue ones back-faces.

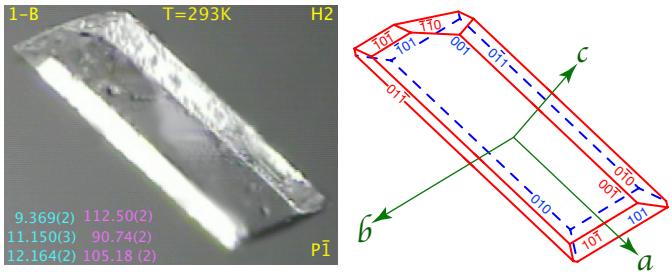

Figure S.13
Photograph, habitus (FaceIt, 2016; Shape, 2011) of the crystal H2 of the desmotrope **1**-B at T = 293 K. Red indices indicate front-faces, blue ones back-faces.

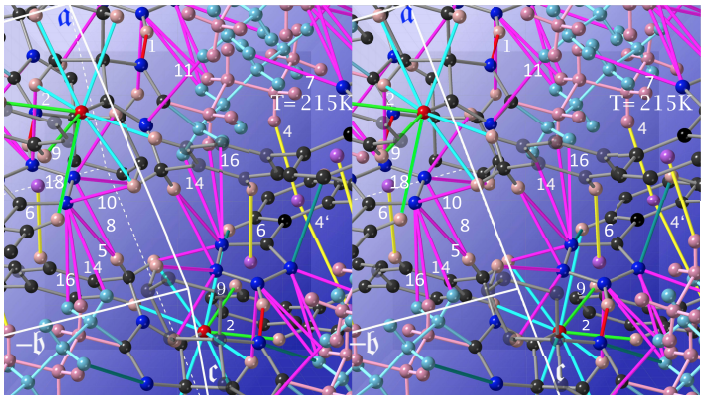

Figure S.14
The environment of the tetrazole moiety in the desmotrope **1**-B. Hydrogen bonds are red, C-H···N interactions mauve, C-H···π interactions yellow and C-H···O are green (inter) or turquoise (intra). View direction is [102] and the numbers refer to Table S.15.

For his basic plot this author uses the following, certified C—C bond lengths: 1.504Å for a single bond in the conjugated 1,3-butadiene and a double-bond character of 0, 1.421Å for the bonds in graphite with a double-bond character of $\frac{1}{3}$, 1.397 ± 0.001Å for the bonds in benzene from high-resolution RAMAN-spectroscopy and/or electron diffraction and a double-bond character of $\frac{1}{2}$, 1.334 ± 0.003Å for the double bond in ethylene from electron diffraction and a double-bond character of 1.

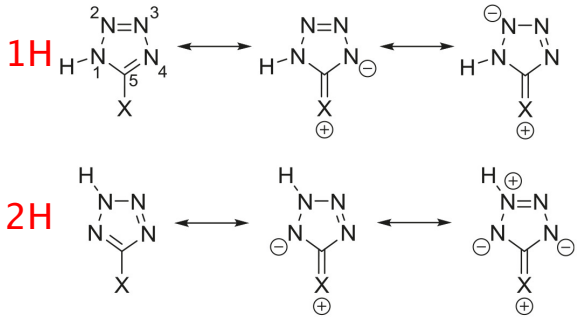

Figure S.15
The resonance structures proposed for Irbesartan by (Szatyłowicz, Stasyuk and Krygowsky, 2015).

In this context it is our pleasure to once again honour Pauling's illuminant resonance-structures (Figure S.15) which were brought to full blossom by (Szatyłowicz, Stasyuk & Krygowsky 2015) in their endeavour to explain the mysteris of tetrazole, and can also furnish satisfactory geometries for the observed values in both desmotropes.

While the observed bond lengths in **1**-A can be quite satisfactorily be explained by only the first, uncharged, of the resonance structures in the upper part of Figure S.15, the situation in **1**-B requires, at least, two such structures, namely the first and the third, charged ones. Indeed, the N2—N3 bond is always the shortest observed N—N one.

It is interesting to realise that another way of estimating the bond strengths, namely the **I**ntrinsic **B**ond **S**trength **I**ndex (Klein *et al.*, 2020), leads to the following relations of bond strengths:

$$\begin{aligned} \text{IBSI(A)}: &\quad \text{N2}-\text{N3} > \quad \text{N1}-\text{N2} > \quad \text{N3}-\text{N4} \\ \text{IBSI(B)}: &\quad \text{N2}-\text{N3} > \quad \text{N3}-\text{N4} > \quad \text{N1}-\text{N2} \end{aligned}$$

This order is quite compatible with our proposed choice of resonance-structures.

A..2. Data Collections of the A-Form

A..2.1. The Powder Data Collections of the A-Form. At the beam-line BM16 of the ESRF, a powder of **1**-A was placed in 1 mm-borosilicate-capillaries and used in Debye-Scherrer-geometry. The sample continuously span around the diffractometer axis. Data were collected in continuous scanning mode in order to avoid the dead-time of a conventional step-scan. After the data collection the counts from the nine detectors were summed and normalised to give the equivalent normalised step-scan.

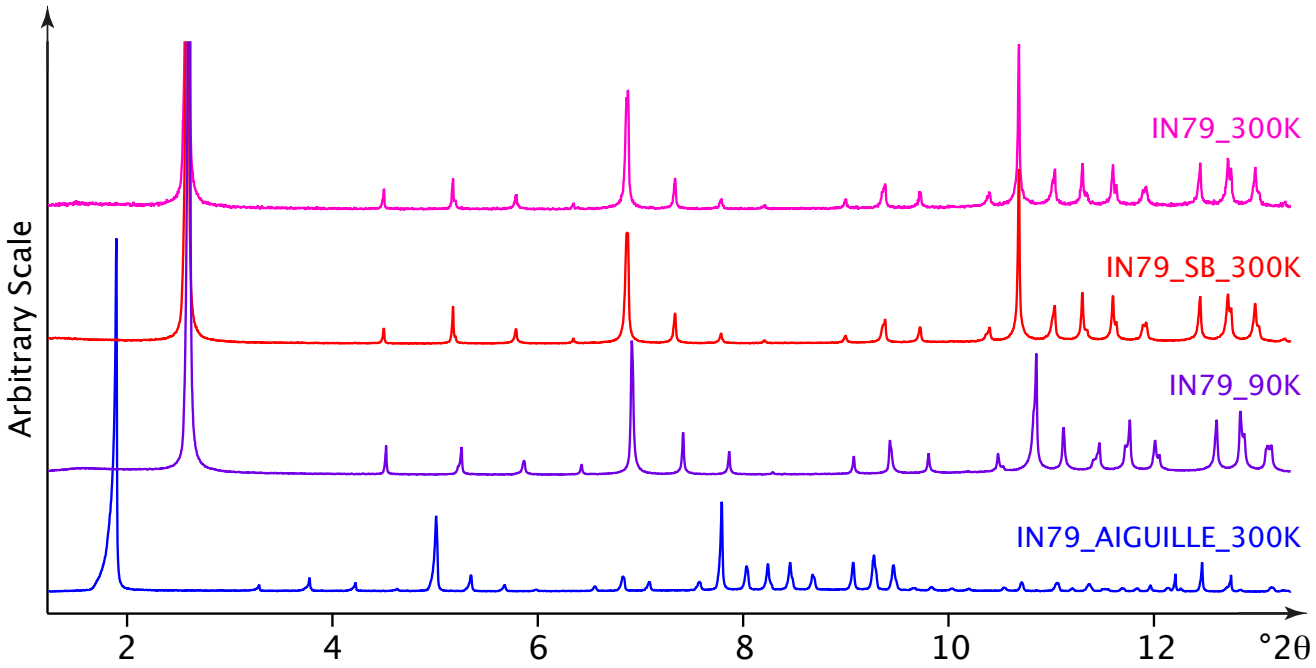

Figure S.16
The powder diagrams of **1**-A. Low angle region.

A cold-nitrogen blower equipped with a precise temperature-controller was mounted below the capillary-sample for the low temperature acquisition. The collection times for each diffraction pattern was between 10 and 12 hours in order to get statistics good enough for an *ab initio* structure determination.

Data were collected on two kinds of samples of **1**-A having grown in two different habiti, namely acicular and tabular. It was also observed that the acicular crystallites displayed a powder which was strongly electrostatic and preferentially oriented along the direction of the needles. Such effects were not observed for the tabular habit.

The following powder diffraction patterns were obtained: for the *acicular* variety IN79_AIGUILLE_300K (λ = 0.62Å, $-15.885 < 2\theta < +41.019^\circ$, 300 K), and for the *tabular* variety IN79_300K (λ = 0.850047Å, $-7.881 < 2\theta < +23.004^\circ$, 300 K) , IN79_SB_300K (λ = 0.850047Å, $-9.873 < 2\theta < 34.002^\circ$, 300 K) and, finally IN79_90K (λ = 0.850047Å, $-13.875 < 2\theta < +68.01^\circ$, 90 K), where SB stands for single bunch. Their low-angle-parts are shown in the Figure S.16.

The 21 first individual line positions were extracted from the overlapping peaks of the diffraction pattern by fitting pseudo-Voigt profile functions to the measured diffraction lines. This set of line positions were fed into the program TREOR working in index-space. A useful solution yielding good figures of merit M(21)=22.9 and F(21)=152.6 was found for the monoclinic cell a=10.955(7), b=18.802(8), c=9.52(2)Å; β=98.34(8)$^\circ$. Supposing this primitive cell filled by three units of $C_{25}H_{28}N_6O$, the calculated density is 1.10 g cm^{-3}, which is exactly the value obtained experimentally obtained by floatation. Unfortunately, this unit cell is not acceptable, as the monoclinic symmetry imposes an even number of molecules. Using instead the program DICVOL working in configuration space, a solution was found in the trigonal crystal system: a=b=37.496(5), c=9.832(2)Å.

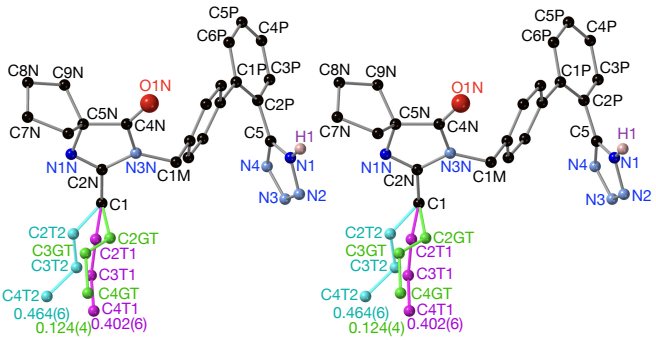

Figure S.17
Molecular conformation and atom-numbering for the desmotrope **1**-A at T = 293 K (crystal A4). The numbers near the chains indicate their s.o.f.s. in this stereoscopic view.

The corresponding figures of merit are excellent: M(26)=24.2 and F(26)=207.5. Moreover, the two cells are quite compatible. Writing the base vectors of the monoclinic cell as: a, b, c and those of the trigonal cell as: A, B, C we find:

$$\begin{pmatrix} A & B & C \end{pmatrix} = \begin{pmatrix} a & b & c \end{pmatrix} \begin{pmatrix} 3 & 0 & 0 \\ \overline{1} & 2 & 0 \\ 0 & 0 & 1 \end{pmatrix},$$

yielding: $||A|| = 37.863, ||B|| = 37.604, ||C|| = 9.52$Å; $\alpha = 90, \beta$=98.34(8), $\gamma = 119.774^\circ$. We understand that the cell found by TREOR describes only a sub-lattice of the trigonal one and is certainly the result of a wrong selection of the starting

base lines by the program (*e.g.* to assign the first line to $(010)_m$ instead of to $(\bar{1}20)_h$). Since the determinant of the matrix above is six, we find 18 molecules in the trigonal cell. Careful inspection of the lines indexed by DICVOL indicates systematic absences for lines not respecting the condition $-h + k + \ell \equiv 0 \pmod 3$. Three space groups were judged to be compatible: R3, R$\bar{3}$ and R32.

The synchrotron-radiation-powder experiments are described in section A..2.1. In order to assess whether the trigonal structural model from the single crystal (Figure S.9) truly did correspond to the powder of **1**-A, we refined a rigid-body model on powder-data. The indexation gave, indeed, a trigonal cell which we refined together with the profile and background parameters using LeBail's method. The synchrotron profile displayed quite asymmetric profiles and even shifts from the Bragg-positions (disorder of the second kind according to Guinier) and so it was no straightforward exercise to obtain meaningful l.p.s. Using a rigid model on the powder-data from 90K, the refinement was unsuccessful to furnish any information on the disorder of the *n*.b.c.s or the content of the [001]-channels.

Table S.9
Comparative Data of **1**-A, Space group is R$\bar{3}$, Z=18. s.c. stands for single crystal; AC for acicular, TA for tabular powders; LB for Le Bail-refinements.

	T [K]	*a* [Å]	*c* [Å]	History	Wavelength λ [Å]	Volume *V* [Å^3]	Id/CCSD / Section	wR_p(LB) R_1(F)(s.c.)
TA1	90	37.2416(2)	9.6686(1)	powder	0.850047	11,613(1)	A..2.1	N/A
A5	90	37.2454(8)	9.65133(17)	stored s.c.	CuKα	11,594.8(5)	IRB-A-TEMP_06_90; 2266410	0.0443
TA1	90	37.24202(75)	9.66841(24)	powder	0.850047	11,613.20(35)	A..2.1	0.0696
A1	114	37.2565(10)	9.6925(3)	*wet* s.c.	CuKα	11,651.2(7)	A..2.2.3	0.0445
AM1	133	37.247(5)	9.7000(19)	*wet* s.c.	MoKα	11,654(3)	*this work*	0.0665
A2	114	37.2303(4)	9.70850(20)	stored s.c.	CuKα	11,654.0(3)	A..2.2.2	0.0448
A3	231	37.3328(5)	9.7877(2)	stored s.c.	CuKα	11,813.9(4)	1999412	0.0365
A4	293	37.4596(7)	9.8361(2)	stored s.c.	CuKα	11,953.1(5)	A..2.2.1	0.0407
AC2	300	37.4145(10)	9.81486(31)	powder	0.62000	11,898.59(51)	A..2.1	0.1432
TA2	300	37.4977(4)	9.8310(1)	powder	0.850047	11,971(1)	A..2.1	N/A
TA2	300	37.4897(15)	9.82881(31)	single bunch	0.850047	11,963.43(70)	A..2.1	0.0964
TA2	300	37.4854(18)	9.82846(42)	multi-bunch	0.850047	11,960.28(92)	A..2.1	0.1488
A5	305	37.4794(13)	9.8448(4)	stored s.c.	CuKα	11,976.3(9)	RE-A-ONE_04_305; *next work*	0.0633

A..2.2. The Single Crystal Data Collections The crystals measured here, namely A1 and A2 (114 K), A3 (231 K), A4 (293 K) and A5 (various temperatures) stem from the same crystallisation (2006). The data collection A1 (114 K) was performed *immediately* after having fished out the crystal from its mother liquor (referred to as wet). The remaining crystals were handled without excessive care, but quickly put into PARATONE-oil and stored in a refrigerator (tagged as stored). The names of the atoms may be found in the Figures S.30, S.19 or S.21. Summarising we may write[9]:

Cryst.	Name	CCDC	Char.
A12	IRB_A_114K_WET_IND_OX	2268210	$\bar{S}$V$\bar{W}\bar{Z}$
A5	IRB_A_TEMP_06_90K_FINAL_NOMASK	2266410	$\bar{S}$V$\bar{W}\bar{Z}$
A4	IRB_A_293K_ZWITTER	1999413	SV$\bar{W}$Z
A3	IRB_A_231K_ZWITTER	1999412	SV$\bar{W}$Z
A2	IRB_A_114K_DRY_ZWITTER	1999411	$\bar{S}$V$\bar{W}$Z
A11	IRB_A_114K_WET	1999410	SV$\bar{W}$Z

We do not dedicate an own section to the collection A3, T=231K, CCDC-Number = 1999412, since it is was measured on the same crystal as A4, but at a different temperature. We therefore commence by giving a detailed description of the data collection on A4, then essential elements for A1 (giving rise to two different models A11 and A12), and A2 and finally conclude by an outlook on A5.

This last collection, A5, is part of the many complementary data collections of the desmotrope **1**-A which will be given in the already mentioned follow-up publication. But - notwithstanding this affirmation - we anticipate the interpretation of one of those collections, namely IRB-A-TEMP_06_90K_00_FINAL_NOMASK.CIF in this Supplementary Material; the reason is twofold, indeed: for establishing a cross-correlation of data collections from two different crystals, and also to provide the results from the lowest possible temperature, *i.e.* 90K. Indeed, the crystal, A5, giving this data collections stems from the same batch as the crystals A1,....,A4. The crystal grew from a mixture of water and ethanol in a sealed tube. More precisely, a column of water was filled into an NMR tube and a second column of ethanol saturated in **1**-A was gently overlaid atop it. Crystals of **1**-A then grew at the interface of the liquids. In particular, A5 has spent his life in PARATONE-oil, and has never been at a temperature above 25°C nor below 5°C.

The structure of **1**-A is rather complicated, since up to three processes control the thermal evolution (th. ev.) of its structure: (1) the disorder - both statistical and dynamical - of the *n*.b.c.s., (2) the water content of the [001]-channels and (3) a possible zwitter-ion of the kind $N_{tet} - H\cdots N_{imi} \longleftrightarrow N^-_{tet}\cdots H - N^+_{imi}$. Because of these complications we decided to keep a watchful eye on these details and use a possibly over-loaded tag-system for the description of the data collections.

[9] We use the following tags: S for squeezed, V for virgin, W for refined water molecules and Z for zwitter-ion. Negations are indicated by an overline.

A..2.2.1. Data Collection A4: T=293K, CCDC-Number = 1999413: A clear colourless prism-shaped crystal (for a view of a similar crystal and its habitus, see (Taulelle *et al.*, 2009) or Figure S.18) of **1**-A of dimensions $0.016 \times 0.017 \times 0.500\,\mathrm{mm}^3$ was glued to a drawn capillary using Super Glue 3; it was kept at 293(1) K by means of a CRYOSTREAM 700 cooler from OXFORD CRYOSYSTEMS for the data collection carried out with the help of the (BRUKER INSTR. SERV., 2016) program. Bragg-intensities were collected using a BRUKER APEX_DUO diffractometer system equipped with an APEX II CCD detector and an INCOATEC CuKα microsource operating at 50 kV and 0.7 mA.

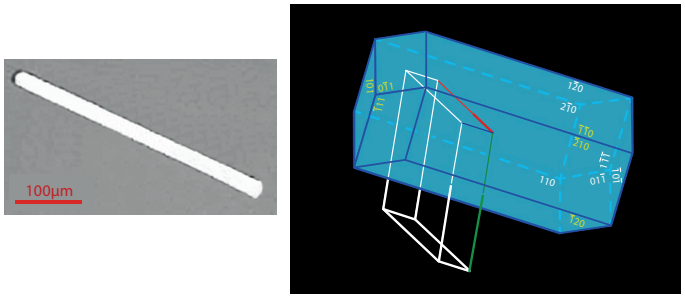

Figure S.18
Photograph of a typical crystal of **1**-A and the BFDH-morphology (Macrae *et al.*, 2006). Yellow indices indicate front-faces, white ones back-faces.

A total of 3487 frames was collected; the total exposure time was 34.87 hours. The frames were integrated with the Bruker (SAINT, 2013) software package using a narrow-frame algorithm. The integration of the data using a trigonal unit cell yielded a total of 37249 reflections to a maximum θ angle of 57.48 ° (0.91 Å resolution). The final cell parameters of a = b = 37.4597(7) Å, c = 9.8360(2) Å, volume = 11953.1(5) Å^3, are based upon the refinement of the XYZ-centroids of 9870 reflections above $20\,\sigma(\mathrm{I})$ with $4.718 < 2\theta < 114.6$ °. Data were corrected for absorption effects using the multi-scan method (SADABS, 2012); 19 reflections were rejected since their χ was bigger than 4. Additional spherical absorption correction applied with $\mu\,\mathrm{r} = 0.2$.

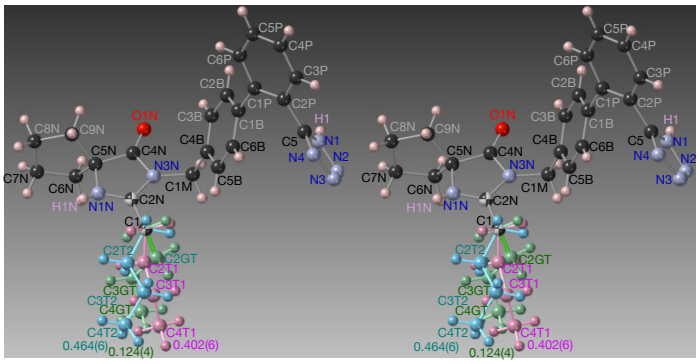

Figure S.19
The atom-numbering for the desmotrope **1**-A at T = 293 K. The numbers near the atoms C4T1 and C4T2 are the occupation numbers of the *n*.b.c.s.

Data reduction, scaling and absorption corrections were performed using (SAINT, 2013). The final completeness is 99.60 % out to 57.461 ° in θ. A multi-scan absorption correction was performed using (SADABS, 2012); $\mathrm{wR}_2(\mathrm{int})$ was 0.1579 before and 0.0469 after the correction. The ratio of minimum to maximum transmission was 0.867. The $\frac{\lambda}{2}$ correction factor was 0.0015. The absorption coefficient μ of this material is $0.543\,\mathrm{mm}^{-1}$ at this wavelength (λ = 1.54184Å) and the minimum and maximum transmissions are 0.6516 and 0.7513.

The structure was solved and the space group $\mathrm{R}\bar{3}$ (#148) determined by the ShelXT (Sheldrick, 2015*b*) structure-solution-program applying the dual-solution-method and by using OLEX2 (Dolomanov *et al.*, 2009) as the graphical interface. The model was refined by full matrix least squares on $|\mathrm{F}|^2$ using version 2018/3 of ShelXL (Sheldrick, 2015*a*). All non-hydrogen atoms were refined anisotropically. Most positions of the hydrogen atom were calculated geometrically and refined using the riding model, but some hydrogen atoms, such as the H1 on the tetrazole and a peak near the imidazole, were located in difference maps. The latter one might be interpreted as a hydrogen atom or a lone-pair electronic density on N1N. We decided to freely refine this H1N and obtained the following distances. (d(N1-H1)=0.89(3)Å, U(H1)=0.045(10)Å^2, s.o.f.(H1)=0.75(6); d(N1N-H1N)=0.76(9)Å, U(H1N)=0.04(3)Å^2, s.o.f.(H1N) = 0.24(5)). These N-H distances lie within what may be expected from X-rays, but the atom is slightly out of plane.

After having refined anisotropically all non-H atoms, but those of the *n*.b.c.s the four strongest residuals clearly indicated a chain in the *all-trans* conformation TT_1. After refining this, the four strongest residuals, again, revealed another n-butyl chain in *all-trans* conformation TT_2. Finally, after this a third n-butyl chain appeared, but this one in $\mathrm{G}^+\mathrm{T}$ conformation. SADI restraints between corresponding bonds were necessary to confine the bond-lengths to acceptable values. But other than that the refinement was stable and did not require any further constraints nor restraints. Site occupancy factors of 0.402(6), 0.464(6) and 0.124(4) for the TT1, TT2 and $\mathrm{G}^+\mathrm{T}$ chains were refined (Figure S.17 or S.19) using a SUMP restraint. A comparison between the Figures S.20 and S.22 illustrates convincingly the changes brought about by the creation of the $\mathrm{G}^+\mathrm{T}$-conformer.

Let us mention that the weak residuals in the [001]-channel did not warrant refining any individual water molecules and therefore the BYPASS mask procedure was applied.

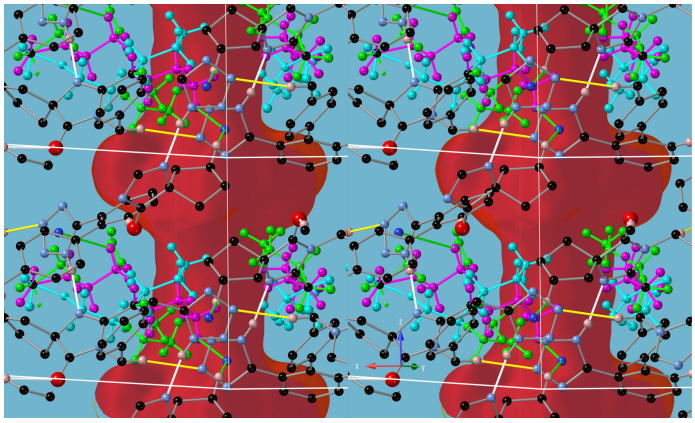

Figure S.20
The [001]-channels and some of the major (non normalised) interactions in **1**-A at T = 365 K.

Here is the list of interesting interactions at 293 K:

D-H···A	D-H	H···A	D-A	∠(D-H···A)
N1-H1···N1N	0.91(3)	1.87(3)	2.775(2)	176(2)
C1M-H1MB···N3	0.97	2.61	3.551(2)	164
C4T1-H4TB···COG0	0.96	3.440		
C8B–H8NA···COG0	0.97	3.153		

And here that at 231 K:

D-H···A	D-H	H···A	D-A	∠(D-H···A)
N1-H1···N1N	0.92(3)	1.78(3)	2.739(3)	174(3)
C1M-H1MB···N3	0.98	2.58	3.527(2)	1643
C4T1-H4TB···COG0	0.97	3.225		
C8B–H8NA···COG0	0.98	3.068		

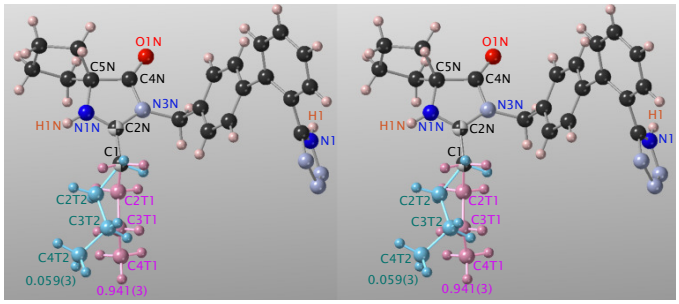

Figure S.21
The atom-numbering for the desmotrope **1**-A at T = 114 K. The numbers near the atoms C4T1 and C4T2 are the occupation numbers of the *n*.b.c.s.

A..2.2.2. Data Collection A2: T=114K, CCDC-Number = 1999411: Since at the end of the refinement (R_1 = 0.0448) no major residual appeared inside the [001]-channels in a difference-map, we decided that there was no need for a MASK-procedure. In other words, there was - as it should be - no trace of water in the structure in the crystal A2 and at this temperature. The occupation numbers of the *n*.b.c.s reached 0.918(3) for TT1 and 0.082(3) for TT2 at this temperature. This is the *all-trans* chain (mauve in Figure S.21) lying in the pseudo-mirror-plane of the imidazole moiety in **1**-A. Perhaps, these data were slightly less good than those from the data collections A3 and A4, since we had to use more restraints for successfully refining the zwitter-ion N1–H1···H1N-N1N, namely -1.2·U_N and AFIX 43 for H1N. This is, perhaps, a hint that our assignment of a zwitter-ion is less valid in this crystal. The occupation numbers of the hydrogen atom of the zwitter-ion are the same as at the other temperatures, *i.e.* 0.79(4) for H1 and 0.21(4) for H1N. Let us close by giving a list of the interesting interactions:

D-H···A	D-H	H···A	D-A	∠(D-H···A)
N1-H1···N1N	0.96(3)	1.78(3)	2.739(3)	174(3)
C1M-H1MB···N3	0.99	2.53	3.473(3)	160
C4T1-H4TB···COG0	0.98	3.0671		
C8B–H8NA···COG0	0.99	2.9074		

The third of these presents the largest shortening with temperature, as shown by a comparison with the values from 293 K and 231 K given in section A..2.2.1.

A..2.2.3. Data Collection A11: T=114K, CCDC-Number = 1999410: The data collection A11 stems from the crystal A1 which was fished out of its mother liquor and immediately placed into a flow of cold nitrogen gas at 114 K. The data collection A1 was done much in the same way as A4, and no description is therefore furnished here for this very reason. Again, the atom numbering may be found in Figure S.21.

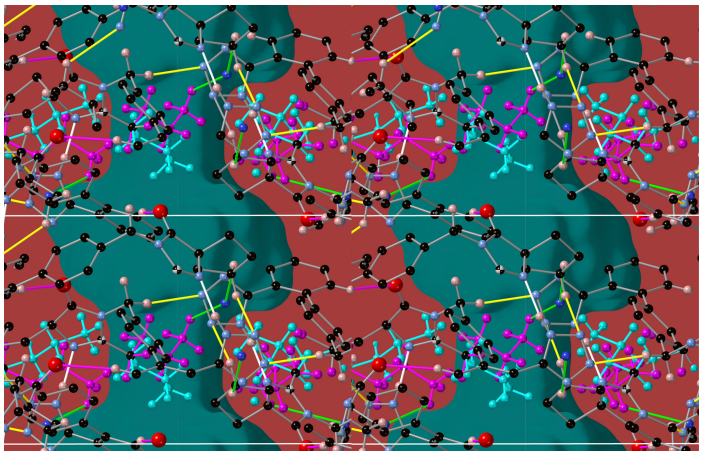

Figure S.22
The [001]-channels and some of the major (non normalised) interactions in **1**-A at T = 235 K.

The anisotropic refinement of the molecule of **1** without its tetrazole-hydrogen gave R_1 = 0.0565. The final values of the population parameters of the *n*.b.c.s were 0.940(3) for TT1 and 0.060(3) for TT2, and the following restraints were imposed on the refinement:

Restraint	1st Par.	2nd Par.	3rd Par.	Atoms
SADI	0.01			C2T1 C1 C2T2 C1 C2T1 C3T1 C2T2 C3T2
				C4T1 C3T1 C4T2 C3T2
SIMU	0.01	0.02	2	C1 C2T1 C2T2 C3T1 C3T2 C4T1 C4T2

In a subsequent difference-map we found the second strongest residuum, Q_2 = +0.6, lying near the nitrogen atom N1. This latter was therefore labelled H1 and the structure could be freely refined to R_1 = 0.0545. In a subsequent difference-map we found a weak residuum near the imidazole-nitrogen N1N. This atom is basically the acceptor of the N1-H1···N1N HB in

this structure. Remembering the wealth of electro-chemical objects reported by (Tosco *et al.*, 2008), we felt tempted, again, to refine this Q as a partial hydrogen atom on N1N anyway. Here are the results of this refinement:

Atoms	Distance	U(H)	PP(H)	Restraints
N1-H1	0.94(3)	0.034	0.82(3)	PP(H1)+PP(H1N)=1.0
N1N-H1N	0.86(12)	0.036	0.18(3)	U(H) = 1.2 U(N)

Since the N1N-H1N distance is closer to a classical N-H distance, **1**-A therefore takes the form of a Zwitter-ion in this crystal.

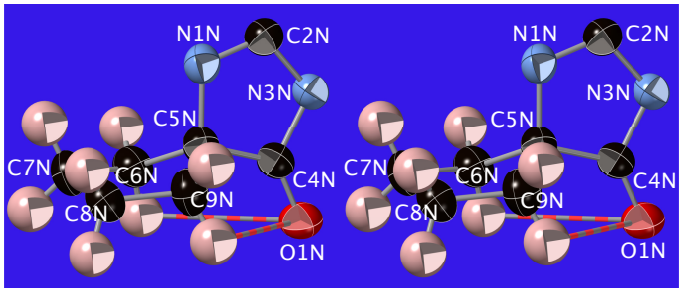

Figure S.23
The envelope of the cyclopentyl-ring in the desmotrope **1**-A (from the data collection A2 at T=114 K) and the weak C—H···O1N «hydrogen bonds».

Ring puckering of the cyclopentane (Cp) ring (C5N to C9N) was examined for **1**-A at this temperature. A half-boat conformation (Fig. S.24) was detected. The atoms C6N, C7N, C8N and C9N span a plane of RMS^2=0.01104Å^2 and the atom C5N lies 0.6060Å above this plane (towards nitrogen N1N). The torsion angle $\angle$(C6N − C7N − C8N − C9N) is -10.7(3)° at 114 K and -14.8(2)° at 293 K; maybe this indicates a fluxional disorder at still higher temperature (like in the desmotrope B)? Note that faintest C-H···O1N hydrogen bonds might further stabilise this conformation (see Figure S.23).

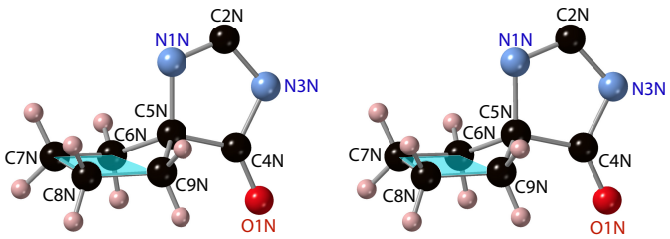

Figure S.24
The envelope of the cyclopentyl-ring in the desmotrope **1**-A (from the data collection A2 at T=114 K). The turquoise plane can be described by $(\bar{4}3\bar{1})$.

After the final refinement (R_1 = 0.0546), the four strongest residua (between 0.84 and 0.5 eÅ^{-3}) appeared inside the [001] channels (Figure S.25). A solvent mask was calculated with the help of the solvent-masking program in OLEX2 (Dolomanov *et al.*, 2009) and 177.0 electrons were found in a volume of 1632.0 Å^3 in one void. These can naturally be related to the presence of one water molecule per formula unit of **1**-A which accounts for 180.0 electrons. The R_1-value thus dropped to 0.0446. Note that both water positions mentioned by Chandrappa (Chandrappa, 2011) can be seen in Figure S.25, namely that near the *n*.b.c.s and that in the centre of the channels. After removing the disordered water the strongest residua were 0.5 eÅ^{-3} and they lie, again, near the atoms C4T1 and C4T2.

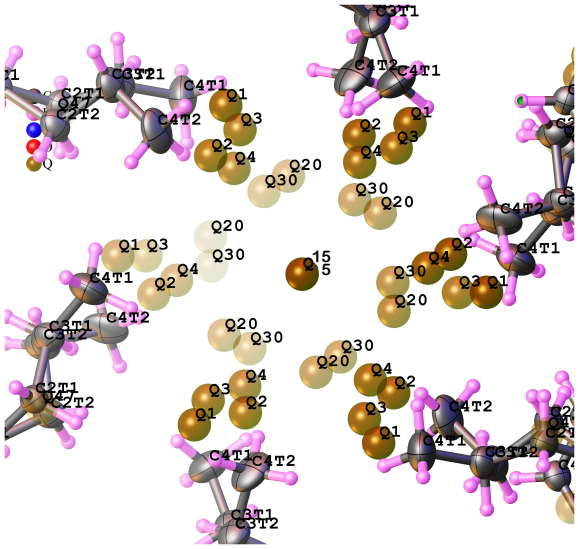

Figure S.25
The residua (labelled Q) in the [001]-channels of the desmotrope **1**-A at T = 114 K at R_1 = 0.0545.

The BYPASS-procedure furnishes roughly one molecule of water per molecules of Irbesartan compared to 0.4 for the collections A2, A3 and A4 (Section A..2.2.2, A..2.2.1). Since the former crystals had years of time to lose their waters, we take this as an indication that the interactions between the water and the walls of the channels are extremely weak. This, perhaps, also furnishes a further clue to the solution features of **1** in water.

Let us now discuss in more details the treatment of the contents of the [001]-channel. The values of $\Delta\rho(x)$ lay between +0.475 and −0.205 eÅ^{-3} and that RMS(ρ) was 0.041 eÅ^{-3}. The corresponding values for the desmotrope **1**-B at 215 K in which there clearly is no water at all are: +0.247, -0.199 and 0.046 eÅ^{-3}. Five strong residua (from +0.8 to +0.3) lie in the channels, but there are other, weaker peaks as well (Fig. S.25). From the growth-history we are led to believe that these could correspond to partial water molecules. In a first model we named seven of these peaks Ne(=O+2H), gave them a common displacement parameter and refined their PPs, using a huge damping factor. This gave R_1 = 0.0462, U=0.20(3)= and $\sum \mathrm{PP_j} \approx \frac{2}{3}$.

This sum is more or less proportional to the number of pseudo-atoms used. In a difference-map, we found the strongest maximum, Q_1 = +0.3, on the C-C bond adjacent to the tetrazole and the highest residua in the channel were only Q_{13} = +0.21 and Q_{15} = +0.20, which is still significantly above the average value. Since this refinement was a bit on the unstable side, we decided to trust (van der Sluys & Spek, 1990) and their BYPASS algorithm in a second model. This lead to R_1 = 0.0440,

but in a difference-map we still found peaks of +0.41, were we had found such of +0.8 without eliminating the regions of disordered solvents. This feature may partly be due to the fact that these peaks lay very close to the border of the region of solvents. This approach led to *one* molecule of water per one of **1**.

Summarising we find: the pseudo-atom model gives a flatter difference-map and a smaller quantity of water, but the BYPASS model yields a better R_1 = 0.0440. Which should we prefer?

The refinement by the pseudo-atoms is slightly unstable and the choice of the number and positions of the pseudo-atoms is slightly arbitrary. Possibly, should one include enough pseudo-atoms in the model, the number of waters might converge towards that found by BYPASS. One should probably also compute group-scattering-factors for water according to Debije's formula. On the other hand, interaction in the channels are relatively weak and BYPASS is certainly apter to model the compound disorder. This water-story would actually require a more serious and deeper study, but since all water has been exorcised in the final industrial product, we decided against such a in this work. albeit, some fascinating features/questions might be connected to this quantity, such as «Can crystals of **1**-A grow without anything in the channels?».

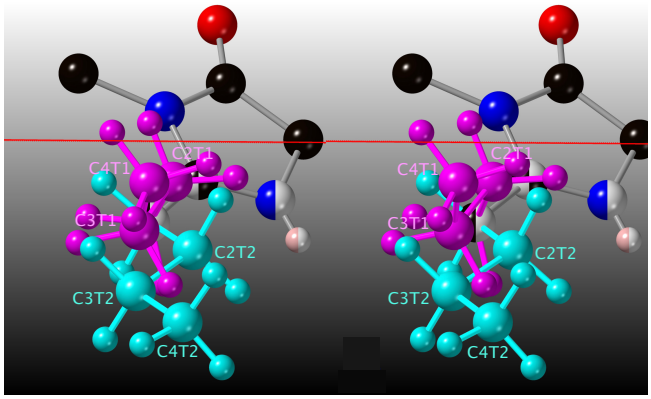

Figure S.26
The conversion of the turquoise *n*-butyl chain into the mauve one. The most likely process probably involves successive rotations, of 50°, around the C—C bonds of the chain. View direction is $[\bar{1}20]$. The red line is the trace of the (001)-plane. The dihedral angles between (001) and the zig-zag-planes of the turquoise and mauve conformers are 27.7 and 57.0°, and the angle between them is 55.654°.

In view of the experimental challenges in determining the quantity of water in the channels and having found between $\frac{2}{3}$ and one molecule of water per molecule of **1**, we can, rather proudly and notwithstanding Puschmann's observation [10], claim to have obtained a reasonable estimation of the water in the [001] channels of **1**-A in this crystal.

A..2.2.4. Data Collection A12: T=114K, CCDC-Number = 2268210: Although the hypothetical water-molecules in the [001]-channels of **1**-A do not offer any straightforward interpretation - especially in view of their history-dependence, it might still be interesting for some colleague to have the individual oxygen-positions available. We started from the refinement A11 (CCDC-number = 1999410) and removed the solvent-mask and the partial hydrogen atom H1N. This raised the R_1-value from 0.0445 to 0.0546. The seven strongest residua in a subsequent difference-map lay between +0.84 and +0.25 eÅ^{-3} and they all lay in the channel.

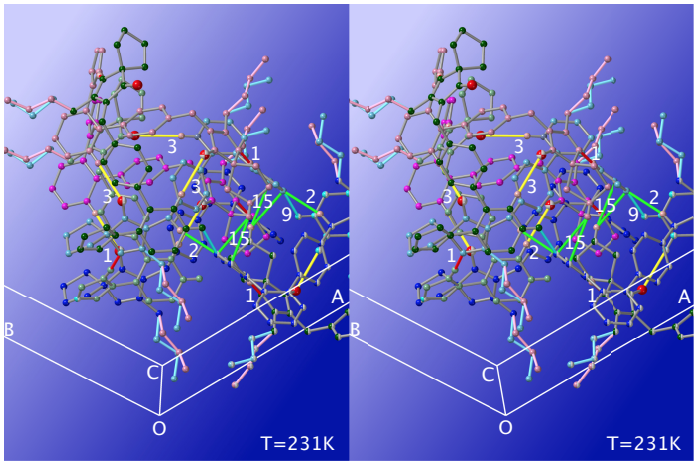

Figure S.27
The nucleus of the desmotrope **1**-A. The numbers near the bonds refer to the **u**-vectors in the Table S.14.

We then refined them isotropically (including their occupation numbers), imposing only:

Restraint	1st Par.	2nd Par.	3rd Par.	Atoms
ISOR	0.005	0.01		O1 > O7

, which refinement converged to R_1 = 0.0439. The resulting occupation numbers lay between 0.42(8) and 0.09(4), and the IDPs between 0.57(6) and 0.15(3). This situation is shown in the Figure S.28.

We then computed the total number of oxygen atoms per unit cell according to: $N_{Ox} = \sum_j ON_j \cdot M_j$, (j = 1, . . . 7), where ON is the refined occupation number and M the multiplicity of the position according to the space group. This yielded 1.2 which is a pleasant number, since it all but confirms the number found by the MASK-procedure. We can finally state with confidence that there are between 1.0 and 1.2 molecules of water in the channels per molecule of Irbesartan in a crystal grown from ethanol/water, rapidly taken out of the mother liquor and mounted in the cold stream.

[10] In his talk in Regensburg Horst Puschmann mentioned that BYPASS slightly underestimates the number of electrons in the regions of disordered solvents.

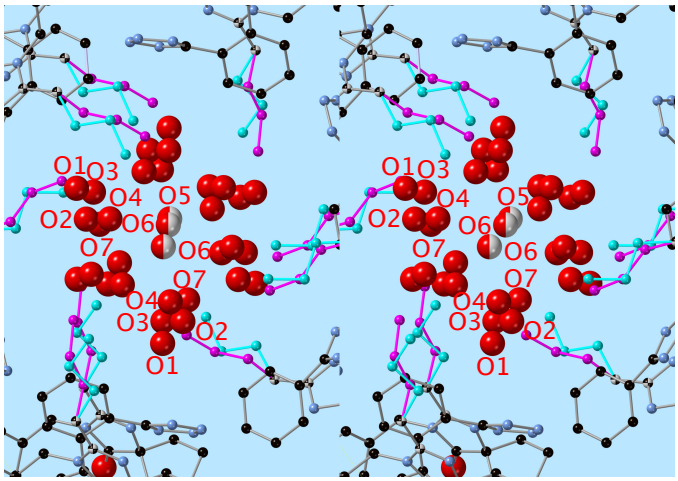

Figure S.28
The solvent-water-molecules in the [001]-channels of **1**-A. The entirely red balls lie on general positions, the red-and-white balls on special positions, O5, in particular, lies on the inversion centre of the threefold inversion axis. The major *n*.b.c. is mauve, the minor one turquoise.

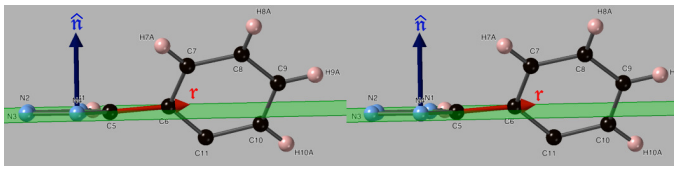

Figure S.29
The non-planarity of the $\overrightarrow{C_5C_6}$ bond with the plane of the tetrazole-ring in the desmotrope **1**-A.

A..2.5. Data Collection A5: T=90K, CCDC-Number = 2266410 : Here we only summarise a few key-results of the refinement A5; atom names may be taken from Figure S.21. In view of the long storing of the crystal it is hardly surprising that after the refinement of all the atoms, no residual stronger than $+0.12\,e\text{Å}^{-3}$ appeared in a difference map of the channels. This finding seems quite compatible with the 0.3 molecules of water per molecule of Irbsartan estimated by the MASK-procedure, especially since the R_1-values are quite the same (0.0443 *vs* 0.0453). It mostly confirms the difficulty of measuring the water contents in such a crystal. The occupation number of the minor *n*.b.c. (turquoise) reaches 0.036(2) at this temperature, and it may be conjectured that the chain will have all but disappeared around T = 50 K. Regarding the distances in the Tet one can see that those at 90 K are quite similar to those at 114 K, albeit slightly larger, as it should be. Contrariwise, intermolecular distances change considerably between 255 K and 90 K, some a bit and others a lot: *e.g.* the hydrogen bond (HB) C1M–H1MA···N3 (from 2.590(3) to 2.53Å) and the C–H···π interaction C4T1—H4TB···COG0 (from 3.476(1) to 3.0214(1)Å). The Figure S.26 also illustrates that the zig-zag-plane of the major chain lies more or less in the pseudo-mirror-plane of the imidazole moiety.

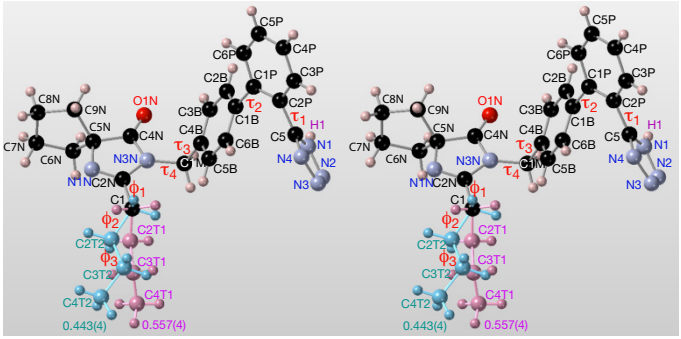

Figure S.30
The atom-numbering for the desmotrope **1**-A at T = 231 K. The dihedral angles defined by (Kellici *et al.*, 2016) are also shown; the angle τ_o lies between the tetrazole and the imidazole. The numbers near the atoms C4T1 and C4T2 are the occupation numbers of the *n*.b.c.s.

A..3. The PBCs

Six weak periodic bond chains (PBCs) (Hartman & Perdok, 1955*a*), (Hartman & Perdok, 1955*b*) in **1**-A are compiled in Table S.15 and shown in Figure S.27. It should be noted that the $\mathbf{u}_2$, a weak $C_{methylene} - H\cdots N3$ hydrogen bond, is the only classical equatorial PBC, but the other ones also add to the cohesion of the structure.

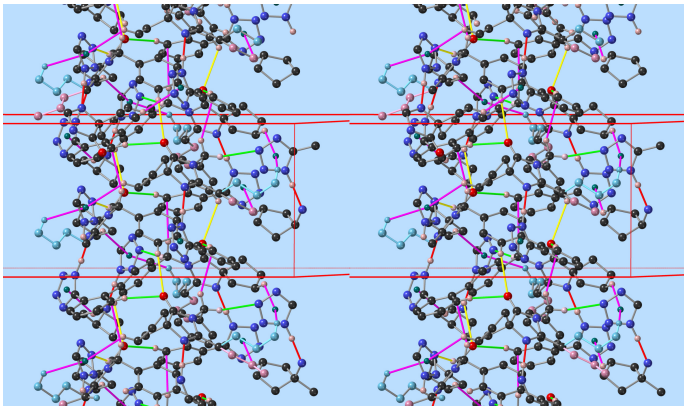

Figure S.31
The interactions stabilising the $\not\perp 113_1$ rods in **1**-A. N – H···N hydrogen bonds are red, axial C – H···O hydrogen bonds are yellow and equatorial ones are green, C – H···π interactions are mauve.

The strongest PBC $\mathbf{u}_1$, the $N_{Tet} - H\cdots N_{Imi}$ HB (Table 1), lies roughly parallel to **c** and thus explains the rapid growth of the (001) face which, of course, does not appear on the growth habit. The oxygen atoms are turned to the inside of the helices and participate in crucial intramolecular $C_{phenyl} - H\cdots O4N$ HBs ($\mathbf{u}_3$). The *n*.b.c.s extend away from it, *i.e.* towards the [001]-channels around the $\bar{3}$ axes. The remaining PBCs lie roughly in the «a, b» plane and contribute essentially to the lateral cohesion of the structure. These would lead to the F-faces $(2\bar{1}0)$ and (111); the former is part of the observed {110}

prism and the latter part of the observed {111} rhombohedron (Taulelle *et al.*, 2006), (Taulelle *et al.*, 2009).

But one must bear in mind that nobody actually seems to have indexed the faces; this is understandable in view of the thinness of the prisms, but nevertheless this information is missing. Not even the indices of the hexagonal prism are utterly certain: in (Taulelle *et al.*, 2009)'s SEM-photograph one can find {110}, whereas Figure S.33 would rather suggest the form {100}. But, of course, dispersion forces are also present in **1**-A and one would need preciser attachment energies in order to better explain the growth shape. The growth of the faces of the {110} prism and the {111} rhombohedron is plagued with agglomeration, macro-steps, faulted 2D nucleation, synosis and rough surfaces (Taulelle *et al.*, 2006). We suspect that this is the very effect of the weak PBCs perpendicular to the hexagonal axes in **1**-A. This habitus (Figure S.18) is well explained by BFDH (MERCURY), except for the aspect ratio, and even more perfectly by the attachment energies calculated by (Taulelle *et al.*, 2009). We should, perhaps, emphasise that the cross-products for the F-faces do not always yield small indices according to Bravais's rule. This is due to the approximations involved in finding the components of the **u**-vectors. But, since in all cases, the observed faces are very near the products of two PBC's, we conclude, by Stranski's inverse analysis (Kern, 1990), that our PBC's do correspond to real and important forces active in building-up the crystalline edifice. Finally, one can readily understand the high aspect-ratio: the lateral PBCs are much weaker than the axial ones, and can only result in a slow growth of the hexagonal prism.

A..3.1. The Zwitter-Ion The water-content in the [001]-channel goes hand in hand with the locking-in of the proton of the N1-H1···H1N-N1N hydrogen bond. Indeed, it was in the crystal A5 (wet) in which we succeeded to refine an N1N-H1N distance of 0.86(12)Å.

As we describe in more detail in section A..2.2.3, we found a weak residual near the atom N1N in the imidazole moiety. Since this maximum and the hydrogen H1 could be freely refined to give meaningful atomic parameters, we decided to include it into the model. We are aware that - in view of the smallness of the residual (0.09e $Å^{-3}$) - this zwitter-ion needs to be checked by, *e.g.* IR, EPR or a similar spectroscopy. But a number of intriguing observations in **1**-A awaiting elucidation, seduced us to include it as a possible contribution to the behaviour of **1**-A. Let us again emphasise an elusive feature. Quite complex acid-base equilibria of **1** in water have been reported by (Tosco *et al.*, 2008), and an irreversible chemical reduction of **1** in water/methanol (7:3) by (Bozal *et al.*, 2009). Both processes are said to depend on the pH, and might likely also influence the dynamics of the N1-H1···N1N HB as already reported by (Oszczapowicz & Czuryłowska, 1984).

A..4. The Calorimetry of 1

The thermal behaviour of **1** and its constituent Tet has already been the subject of quite a few studies above room temperature. Indeed, melting temperatures, T_m, enthalpies, ΔH_m, thermogravimetry, decomposition and its modelling have been reported by (Sanofi, 1994, Figure S.34), (Kiselev *et al.*, 2011), (Zong *et al.*, 2018). Some pertinent data on the desmotropes of **1** are compiled in the Table S.10. We shall comment on some features of the existing data, but also explore the low-temperature-region by two novel series of measurements, M1 and M2 (Figure S.35).

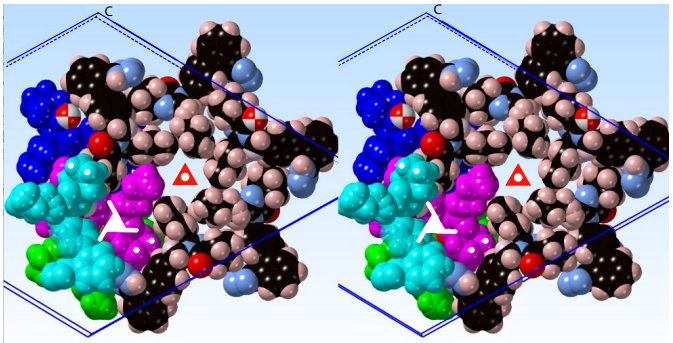

Figure S.32
The $p113_1$ columns at $(\frac{2}{3}\,\frac{2}{3}\,z)$ and the [001] channels at $(\frac{1}{3}\,\frac{2}{3}\,z)$ in **1**-A. The turquoise and mauve molecules also explain our nickname for the molecule, namely puppy.

M1: from a METTLER-TOLEDO instrument DSC3^+ available at the LMOM-laboratory at EPFL using ethanol as a cooling medium ($T_m = -114.5\,^\circ$C). Heating rates between 5 and 10 °C min^{-1} were chosen and a few [mg]s of **1**-B of ill-defined batch number were weighed into aluminum pans. Since the heating runs began at 20 °C or below, the crucibles were left open and a nitrogen purge was used in all measurements,

M2: from a METTLER-TOLEDO instrument DSC30 at the Solid State Laboratory of Universität Bern, using liquid nitrogen as the cooling medium. The scan speed was 10 °C min^{-1} for all scans. 40μL aluminium crucibles were used with a hole in their lids, and N_2 was used as a purging gas. One crucible of the desmotrope B was weighed in (658, 10.001 mg), and two of the polymorph A (659, 4.373 mg, 664, 7.669 mg). Should we mention that the polymorph B appeared very fine-grained and easily «flowing» upon transferring it into the crucibles, despite a tendency for being hygroscopic sometimes observed on single crystals? The desmotrope A, on the other hand, presented itself as quite a pasty and sticky substance not so keen on entering the crucible.

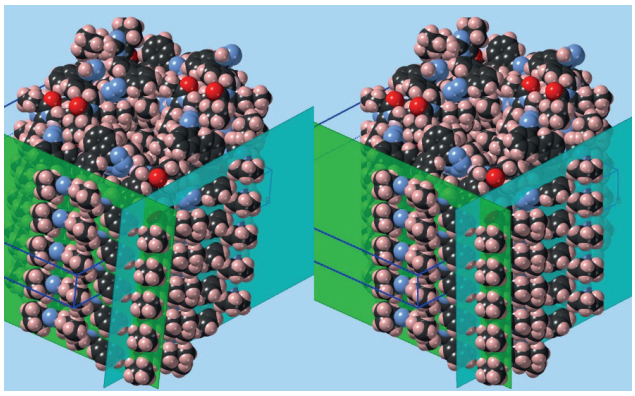

Figure S.33
The lipophilic polarity of the {100} faces in **1**-A.

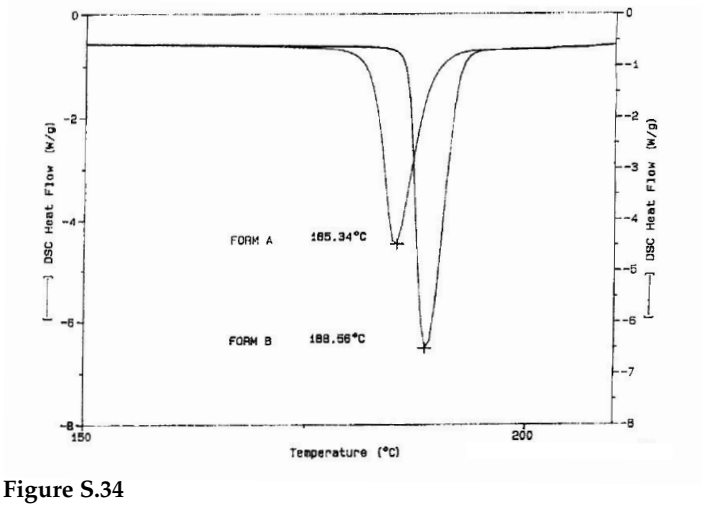

Figure S.34
DSC-heating runs, on a DUPONT 910, of the two desmotropes of **1** (SANOFI).

A..4.1. 1-B: (i) A unique fusion-peak at 187.0 °C in M1 confirmed that it was the pure desmotrope **1**-B. The melting points, T_m, of Sanofi, Frey and Ochsenbein (Table S.10) agree well, but that of Zong is questionable: not only is the melting peak very asymmetric and its value considerably below that of the other three measurements, but these authors do not reveal much about their sample either: indeed, they might have studied a mixture of the two desmotropes. For this reason, we do not include their values into the means reported here. We first notice that the measured melting temperatures T_m, are quite consistent (but we are reminded that some standard uncertainties are seriously underestimated). Indeed, we find: $T_m B = 187.5 \pm 1.2$ °C. Even the melting enthalpies, ΔH_m, from different calorimeters are quite comparable: we find: $\Delta H_m B = 51.6 \pm 2.5$ kJ mol^{-1}.

(ii) In the *very* first experiment of M1, the pan (2.46 mg of desmotrope B) was first cooled down to −95 °C from room temperature, then heated up from −95 °C to 200 °C (Figure S.35a,b,e). We find a clear peak typical for a first order transition at T_{c_4} = 208 K (Figure S.35a/top, dashed violet line), a quite unusual shoulder on the low-temperature-side (filled turquoise area) during cooling-cycles and a melting transition at $T_m B$= 187.0°C. The integration of the peak in this experiment was not very satisfactory, since the baselines were quite unforeseeable. For this reason we did not venture to even estimate anything. The shoulder on the low-temperature side (Figure S.35b/top) can also be perceived in the series M2; the area of the peak could be estimated with the help of the peak as it appeared during heating-runs and, to a good approximation, 3.5 kJ mol^{-1} is a valid estimate for $\Delta H_{II\to I}$. The I→II transition at T_{c_4} is perfectly reproducible, even in multiple cycles, with a hysteresis never exceeding 1°.

(iii) A very minor hysteresis of the I⟶II transition was observed in both series M1 and M2, *viz.* one degree for the former and two for the latter. A hysteresis is generally thought to be linked to a first order phase transition, which is obviously confirmed in this case.

Let us finally emphasise, though, that these stochastic behaviours does not invalidate in any major way the functioning of the diffuse thermal process described above.

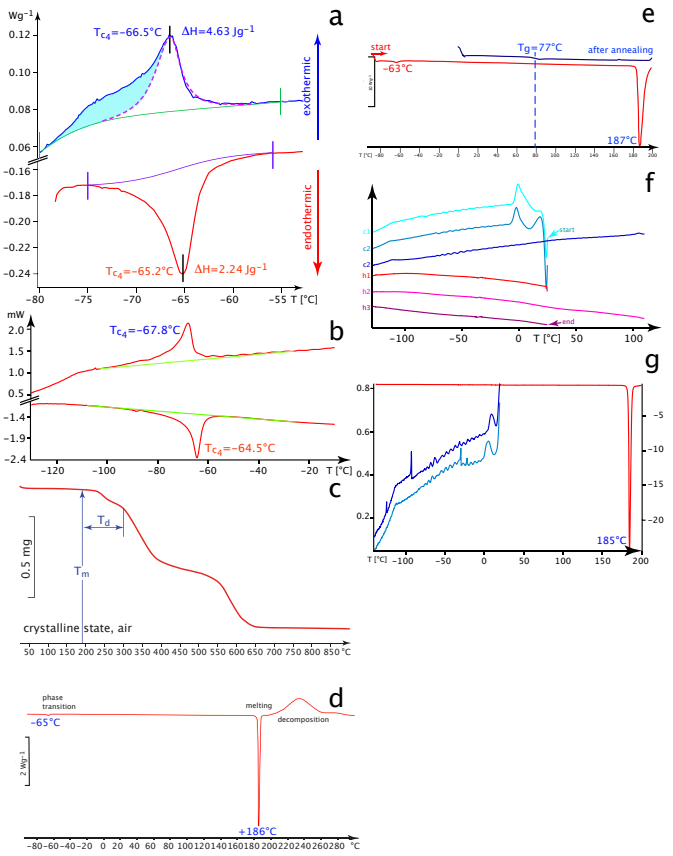

Figure S.35
(a) The I↔II transition in **1**-B in Experiment M1 using ethanol to cool, (b) The I↔II transition in **1**-B in Experiment M2 using liquid nitrogen to cool, (c) The *typical* three-step decomposition in **1**-B demonstrated by thermogravimetry, (d) Melting and decomposition in **1**-B, (e) The recrystallisation behaviour of **1**-B and the glass transition, (f) Three cycles of DSC for **1**-A (experiment A664) below the melting temperature. (g) A cycle and a half of DSC of **1**-A (experiment A659) showing possible artefacts in cooling-runs and the melting transition.

(iv) We can confirm that no mass loss (Figure S.35c) was observed below the normal melting process. Zong give a lower limit of 204.7 °C below which no mass loss was detected. This limit is roughly confirmed by Sanofi and *This work*. The width of our melting transition (Figure S.35b) is about two degrees and a half, comparable to 2 to 3 °C in pure indium, therefore

quite typical of a pure crystalline solid. Sanofi provided completer information and details of their experiment; their values of T_m = 188.9 °C and ΔH_m= 126.4 Jg^{-1} lay very close to ours (Table S.10).

(v) Anticipating some results of the next section, we summarise: The I→II transition consists in a cooperative deformation of the whole structure taking place within a few degrees, but for understanding the G$^+$T/TT conversions, we must accept the idea that each heart of a madeleine is in a conformational state totally unpredictable and energetically slightly different from the surrounding hearts. The whole conformational conversion is spread over a large temperature domain such that at each individual temperature the absorbed energy is so small that it does not generate an observable signal. Or in other words: the transformation is *not* collaborative at all: there is too little coupling between neighbouring cells for producing even tiniest regions transforming together. Each cell does its own thing and uses a little energy at a particular temperature. But, under certain conditions, it might happen that larger, homogeneous domains are created which would then yield a detectable signal. Finally, from the presence of the shoulder upon cooling, and its absence during a heating-run, we must conclude that the distortions and distributions of the hearts are quite different in the two regimes on either side of the transition at T_{c_4}.

A..4.2. 1-A: First we notice that the melting temperatures, T_m, of the samples 659 (4.373 mg) and 664 (7.669 mg) of the experiment M2, do indeed corroborate the nature of the desmotrope **1**-A. This should come as no surprise, since the samples were *certified* by the supplier (SANOFI). Indeed, Table S.10 furnishes the following mean-values: T_mA = 184.68 ± 0.56 °C (and a width of 3°) and $\Delta H_m A$ = 39.6 ± 1.7 kJ mol^{-1}. Our next and main interest was to enquire whether any thermal event could be associated with the discontinuity of the *a* l.p. at T_3.

Figure S.35f shows that in this particular experiment no major nor reproducible thermal events could be seen. Nevertheless, we must refrain from any conclusions at this point, since α) we are not sufficiently certain of the presence or quantity of water, and β) in the experiment 659 (Figure S.35g) there were some transients and spikes, glitches and oscillations we were unable to explain so far (nor even their nature: ghost or real? possibly masking weak thermal events). So, unfortunately, we must again entice our friendly readers into waiting for the already promised, enlightening follow-up publication. At this point, we can only confirm the existence of the melting transition, but cannot give any details about the decomposition, solvent content or thermogravimetry. In other words: we must study a powder, by DSC, obtained in exactly the same way as the crystals A1,A2;. . .,A5, namely by diffusion of ethanol into water.

In the experiment 664, we weighed in 7.669 mg of **1**-A/crtfd in an aluminium crucible, cold-sealed it, made a little hole in its lid and started cycling.

In view of the [001]-channels present in the desmotrope A, it appears reasonable that less energy should be required to bring the molecules to a totally disordered state, compared to the compact desmotrope B.

Table S.10
Calorimetric Phenomena in **1**, M_r = 428.53 g mol^{-1}. Positive values do correspond to exothermic phenomena.

Sample	Batch	Desmo-trope	Nature	Onset [°C]	Enthalpy [J g^{-1}]	ΔH [kJ mol^{-1}]	T_m [°C]	Entropy [J g^{-1}K^{-1}]	Reference
Aladdin Chem.		A,B?	Fusion		65.2		175.6		(Zong *et al.*, 2018)
SR47436-A	93-06	A	Fusion	182.4	96.7	-41.439	185.3		Sanofi (1994)
SR47436		A/certfd	Fusion	183.02	-91.35	-39.146	184.53		Béatrice Frey (M2, 2023)
CALOX		A	Fusion		89(2)	-38.139	184.2(2)	0.48	(Araya-Sibaja *et al.*, 2019*a*)
CALOX		B	Fusion		115(3)	-49.281	186.7(1)	0.62	(Araya-Sibaja *et al.*, 2019*a*)
SR47436-B	94-01	B	Fusion	185.5	126.4	-54.166	188.9		Sanofi (1994)
SR47436		B/certfd	Fusion	175	119.73	-51.308	187.0		This Work (M1, 2021)
SR47436		B/certfd	Transition I→II	-65.17	3.42	1.466	-67.80		Béatrice Frey (M2, 2023)
SR47436		B/certfd	Transition II→I	-68.025	-3.53	-1.513	-64.525		Béatrice Frey (M2, 2023)
SR47436		B/certfd	Glas Transition	-43.33	1.79		+77.8		This Work (M1, 2021)

A..4.3. Molecular Integrity The melting transition seems to presents a serious undercooling. (Zong *et al.*, 2018) were the first to document an exothermic decomposition process right above the normal melting (Figure S.35c). Seeing that at 260.8 °C, we cannot talk of Irbesartan any more, it becomes clear that we must stop heating at 200 °C, if we ever hope to recrystallise **1** form the melt. Unfortunately, this is more complicated, since under no circumstances, we were able to ever obtain **1** again after passing the melting transition. Indeed, for **1**-B no re-crystallisation-peak was seen, but a difference in the heat capacity at T_g= 77 °C appeared; we interpret this as the glass transition which was exploited by (Skotnicki *et al.*, 2021). This confirms, once more, the weakness of the intermolecular interactions. Notice that (Zong *et al.*, 2018) were able to ascribe the first decomposition-step to the opening of the tetrazole and imidazole rings. This finds further support by the small Δ_{iso} = 12 kcal mol^{-1} computed by (Alkorta, 2010) for the ring↔chain isomerism.

Not knowing the viscosity of the molten **1**, we can only speculate about the glass transition at T_g and the re-cristallisation at T_m. We have already mentioned that intermolecular forces are quite weak in **1**, especially at 190 °C. This weakness is cer-

tainly not helpful for growing bigger domains of **1**-B in phase I, should it even ever nucleate at such high recrystallisation rates. The strongest interaction, the $N_{tetrazole} - H\cdots N_{imidazole}$ hydrogen bond, is mainly used for building up the dimers. But even it may have become too weak at the melting temperature. In any case, this glass state makes our diffuse model within the phase I of **1**-B all the more seducing.

A..5. The Thermal Expansion in 1

A..5.1. 1-A: We have carried out fifty data collections on a single crystal of **1**-A from 2006, named A5K, in the temperature-range from 90 to 365 K (as fuller explained in the follow-up publication). We have refined lattice parameters (l.p.) at various temperatures; their thermal evolution (th. ev.) are shown in the Figures A.4, S.37 and the occupation numbers of the n-butyl-chains (*n*.b.c.) in the Figure S.36. Eigenvalues and -vectors of the α tensor for 20 temperatures between 265 and 90K were computed with the help of the TEV program (Version 1.0.2) by (Langreiter & Kahlenberg, 2015) and further analysed with the help of IgorPro 9 (WaveMetrics, 2021).

We have previously mentioned that a certain degree of irreversibility might exist in the th. ev. of the desmotrope **1**-A. This suspicion is clearly confirmed by a look at the Figure S.36, but

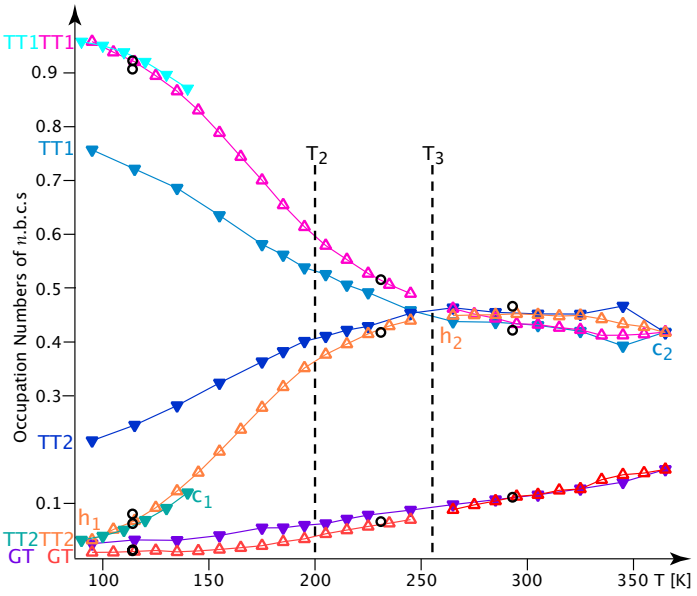

Figure S.36
The th. ev. of the occupation numbers of the three conformers in the desmotrop **1**-A. ↘ Open △s appear in heating runs and full ▼in cooling runs; all measurements stem from the crystal K2. *c1* refers to the first cooling run (140 ↘ 90 K), *h1* to the first heating run (95 ↗ 255 K), *h2* to the second heating-run (265 ↗ 365 K) and *c2* to the second cooling-run (365 → 95 K). Black ○s refer to the data collections A1, A2, A3 and A4, mauve, orange and red △s refer to TT1, TT2 and GT on heating; and polar, royal and turquoise blue ▼s to the same upon cooling. The occupation numbers of the GT-conformer of the series c1 were not plotted at all, since they very nearly coincided with those of the series *h1*.

we must keep in mind that we do not have enough information about the thermal history of the crystal A5K for considering this a certainty, and many more complementary experiments are still needed to confirm this idea.

Let us then gather the pieces of information we already have available. Since the interconversion of TT2⟷GT is most likely a thermally activated process, we can still surmise that the wreath of *n*.b.c.s will retain its shape from crystallisation-time at temperatures below room temperrature (r.t.), despite the presence of a GT conformer. If we cool down such a crystal - as in the cooling run *c1* - down to 90 K, the TT2 (0.03203) and GT (0.00927) conformers will all but disappear. It is in the subsequent heating run *h1* that we observe a perfectly reversible behaviour (Figure S.37).

But once one has heated above a certain critical temperature, T_c, things do change. (This temperature might lie around 345 K at which we observe a mild deviant behaviour of the curves of the occupation numbers (Figure S.36).) The wreath of *n*.b.c.s will be distorted and change the whole behaviour of the system when cooling down in the cooling-run c2.

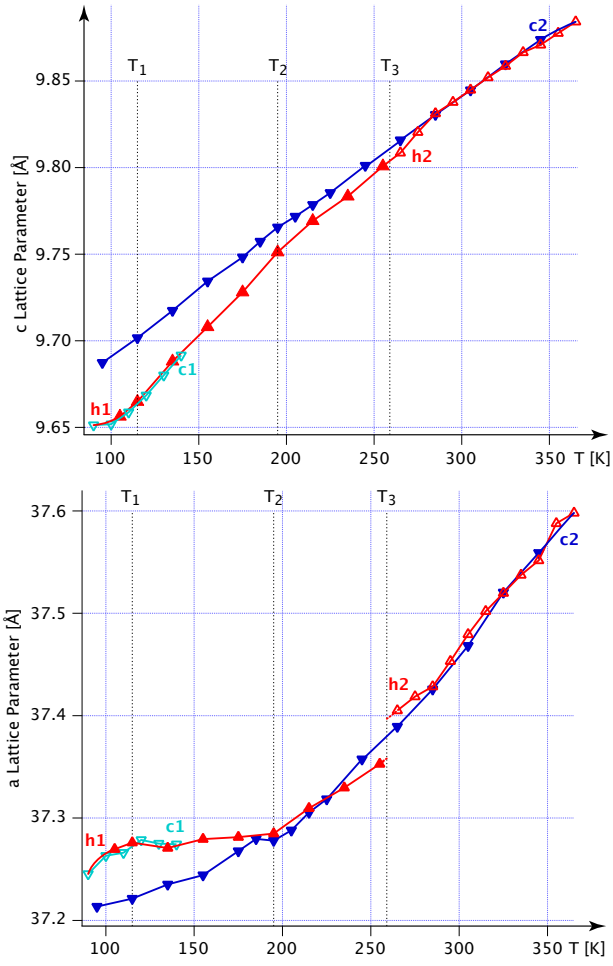

Figure S.37
c1 means first cooling (140 → 90 K), *h1* first heating (95 → 255 K), *h2* second heating (265 → 365 K), *c2* second cooling (365 → 95 K). Full scale of measurements.

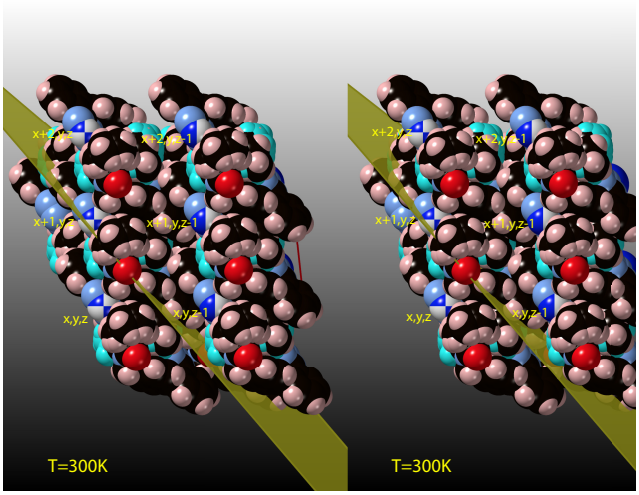

Figure S.38
A block of the desmotrope **1**-B presenting the cash-box-like stacking of the madeleines along the **a**-axis. The green plane is the least-squares plane of the madeleines, *i.e.* $(\overline{5}48)$ if one is willing to accept a deviation of 1.8°.

The downward th. ev. of $V(T)$ in Figure S.39a looks roughly linear, but a closer inspection reveals a general curvature, and the data points 1 and 2, defined by two vertical mauve lines, seem to lie off the general tendency. As always, we try to find a simpler function for describing the observed tendency, which would keep the quintessence of the information, while getting rid of statistical fluctuations. It is well-known that higher order polynomials oscillate quite a lot and, often, also smooth out too much. Smoothing splines, on the other hand, contain a least-squares term and a penalty-function controlling unevenness; they can be fine-tuned by a parameter λ according to the problem at hand. We shall show below that they are very useful indeed.

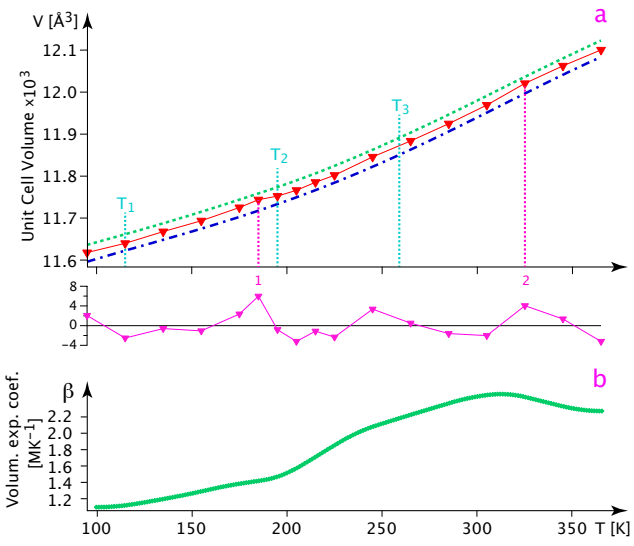

Figure S.39
a) The observed unit-cell volumes $V(T)$ (series c2) at temperatures *decreasing* from 365 to 95 K (red ▼s). Approximations by a fourth order polynomial (blue, dot-dashed line) and smoothing spline (S=0.01) (green dotted line). b) The *volumetric*, β, expansion coefficient computed as the numerical derivative of the smoothing spline approximation shown in the sub-figure a.

Now, the individual volumes are certainly very precise (their error-bars are well hidden inside the red triangles), so much so that we, following (Hamilton & Abrahams, 1970), multiplied the standard uncertainties by a factor of three. Their accuracy is, of course, more difficult to assess. Ideally, one should measure several crystals under as different conditions as possible in order to obtain an estimation for the exterior standard uncertainty. This is not quite feasible, for obvious reasons, and even more so, since we do not have any pristine crystals left. So, we try to identify the intrinsic features of the system, and ignore the other ones. One reason for an erratic or unpredictable behaviour might be that some relaxation time in our experiment was substantially longer than the time between the experiment at neighbouring temperatures.

It turned out that both the polynomial and the smoothing spline do extirpate or smooth the questionable points 1 and 2. Since in the derivative from the smoothing spline, at least some discontinuities remained to be seen, we decided that the curve in Figure S.39b was best suited for representing the complex processes in **1**-A. But we must never lose sight of the somewhat hidden feature in this system.

One might use a rational function, but we chose to use two fourth-order polynomials we glued together (anyway, the effect would be the same, namely a discontinuity at T_3 (see Figures S.37). The numerical derivative $\frac{\partial a(T)}{\partial T}$ presents *five* minor maxima; these clearly reflect some tiny fluctuations in the $a(T)$-curve. Picking up a thread developed in the discussion of the $V(T)$-curve, we decided to pay cursory attention to these minor effects at best, which will leave us with the only major effect at T_3.

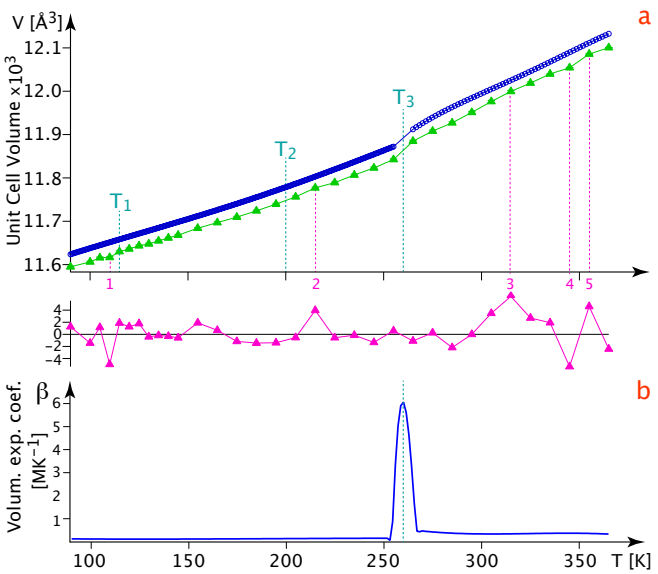

Figure S.40
a) The original volumina of the desmotrope **1**-A as a function of *increasing* temperature in the first heating-run (green ▲) and their approximation (blue ∘) by two fourth degree polynomials glued together (shifted by 10Å^3 for better visibility). b) The *volumetric* expansion coefficient, β, computed as a numerical derivative of the polynomial approximation interpolated by means of a smoothing spline (S=0.5).

The upward th. ev. of $V(T)$ in Figure S.40a presents a mi-

nor discontinuity at T_3 = 265 K; this can also seen in $a(T)$, but less clearly in $c(T)$ (Figure S.37). The parts of $V(T)$ below and above T_3 could be appropriately modelled with the help of a fourth-order polynomial; but it must be noted that the residuals (mauve) do reveal some minor, but essential deviations. We shall deal with them in the already announced follow-up publication. For the present purposes we note that there is a discontinuity at T_3, but this statement clearly needs to be confirmed by a study combining Karl-Fischer and scanning calorimetry for monitoring the water content. Let us close by a slightly conjectural summary: The desmotrope **1**-A presents a certain degree of irreversibility (between the *c2*- and *c1*-runs) (Figure S.36) and a possible existence of a meta-stable phase. The latter seems to be related to the precise manner of crystallisation. Applying the same numerical methods for $a(T)$ and $c(T)$, we can confirm this irreversibility which will be presented in many more details in our follow-up publication.

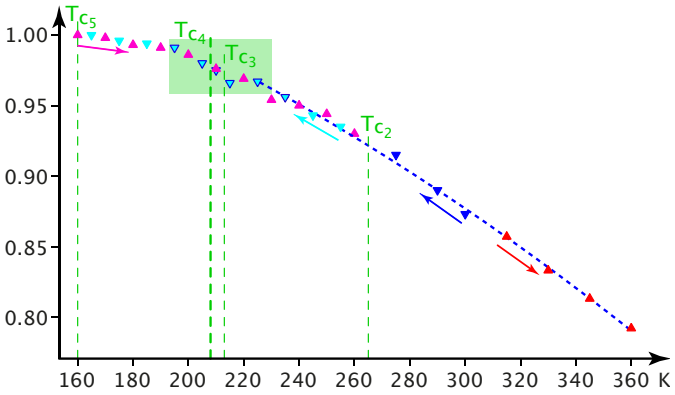

Figure S.41
The thermal evolution of the occupation number of the major Cp-individuum in **1**-B; red ▲, heating from series BH. blue ▼, cooling from series BC, turquoise ▼, cooling from series BD and mauve ▲, heating from series BU. The minor component of Cp disappears at T_{c_5} (compare with Figure S.52). The data points lie quite nicely on an almost linear (blue-dashed) curve. But at T_{c_3} a small plateau and a change of slope (green rectangle) seem to indicate some change of the OD-process, which had previously also been seen by the analysis of the α-values.

A..5.2. 1-B: We had refined lattice parameters at various temperatures from three different crystals (dubbed K2, K3 and K4); their temperature-dependence is graphically represented in Figure 5. The crystals were from the same batch (IB, 20QEA,5) of 15th June 2006 and resembled each other like one egg another; we show crystal K3 in Figure S.5.

We decided that we should obtain a more revealing, though less precise, picture of reality by combining the values from different crystals for computing the functional form of their temperature dependence. Indeed, in Figures S.48, S.42 and 5 it becomes clear that even the lattice parameters from different diffractometers and techniques are quite comparable and that there are few, if any, outliers. In general, the variations are quite linear, except near the phase transition at T_{c_4}, and a line might have been good enough for the purpose (as can be seen from the regression coefficient stated in the Figures). But in other fits (such as those of a and α below T_{c_4}) not even a polynomial of second degree was sufficient and we had to resort to the third-degree persuasion.

In general, the observed values do not follow the analytical curves all too well; so there is some degree of of arbitrariness in the eigenvalues and -vectors of $\boldsymbol{\alpha}$-tensor. One should, therefore, not attribute a too high accuracy to these; but the general trends and shapes (summarised in Figure S.52) are certainly correct. From Figure 5 it is also clear that not all the lattice parameters do change at exactly the same temperature (*e.g.* the angles α and γ). This desynchronisation introduces another doubt when deciding which values to include in a fit. When comparing our results with those of recent paper on magnesium sulphate nonahydrate (Fortes *et al.*, 2017), we can only awe-fully respect their superiority. What could we have done better? Perhaps, powder measurements are simply better for this purpose? (*E.g.* the inclusion of the a value from a powder measurement might rectify the slight inconsistency, between 116 and 100 K, in the tripod of the α-eigenvectors?) Maybe, we did cool or heat our crystals too quickly (meaning that we did not give them enough time to reach some equilibrium)? The thermal history certainly does play a rôle - as we had already pointed out above - so, possibly the answer lies there. But then again, our fits are not so woebegone after all, and single crystals are certainly much superior when it comes to keeping track of any orientational phenomenon. Be this as it may: we are confident that our temperature dependence of the tripods at least do provide some reasonable image of reality.

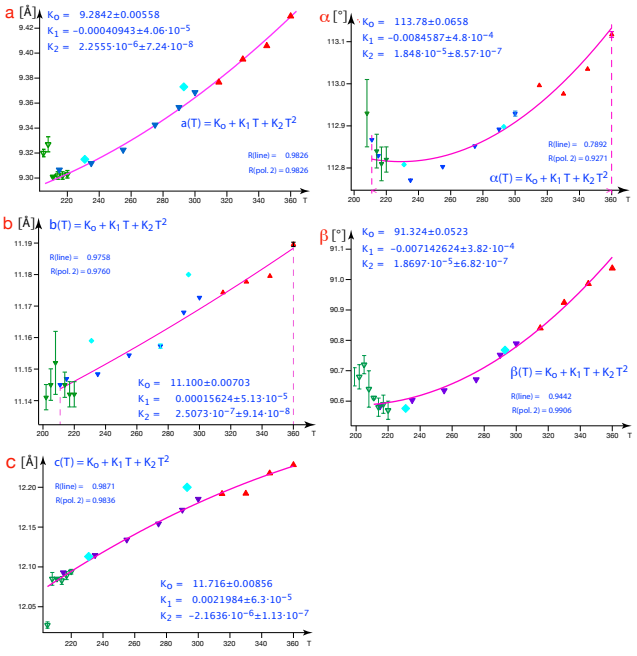

Figure S.42
The fitting of the six lattice parameters as functions of the temperature above T_{c_4} in **1**-B. In each case the type of function is indicated, as well as the regression coefficients. Mauve ▼s refer to crystals K2 and K4, green ▼s to crystal K3, and dark green ◆s to the data collections using MoKα radiation.

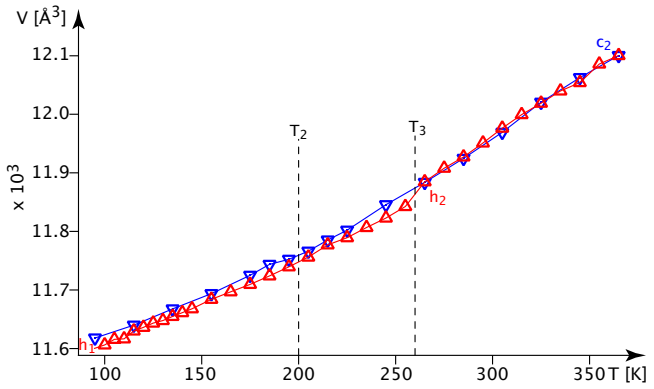

Figure S.43
The volume of the unit cell of the desmotrope **1**-A as a function of increasing temperature (red △s refer to the series *h1* and *h2*, same crystal A5K, but different mounting), then as a function of decreasing temperature (blue ▽s from series *c2* from crystal A5K, following immediately on series *h2*). T_3 is the temperature of a suspected thermal event marking at least a principal, yet isosymmetric change in the wreath of *n*.b.c.s. T_2 marks a clear, yet unexplained fluctuation in the structure of **1**-A.

A comparison of the cyclic behaviour of V(T) in the two desmotropes reveals a small, but significant difference. While V(T) in **1**-B is surprisingly reversible (Figure S.44), that of **1**-A (Figure S.43) is more complex, and it certainly presents a clear bias between T_3 and 95 K. Another difference concerns a number of small fluctuations in **1**-A in the entire temperature range investigated. In the desmotrope **1**-B, there are also some complications between 280 and 240 K, a region in which some minor reorientations of the eigenvectors of the $\boldsymbol{\alpha}$-tensor are observed. The values of the volumetric coefficient of thermal expansion in the two desmotropes are quite comparable indeed: in both polymorphs the β-values at higher temperatures are higher than at low temperatures. In **1**-A (Figure S.49 and S.50) we find a difference of 40 MK^{-1} and **1**-B (Figure S.46 and S.45) one of 50 MK^{-1}.

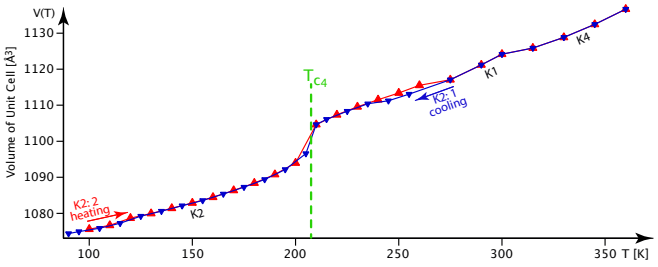

Figure S.44
The volume of the unit cell of the desmotrope **1**-B as a function of decreasing temperature (blue ▼s refer to crystals K2), then as a function of increasing temperature (red ▲s from crystal K2). T_{c_4} is the temperature of the I⟶II transition. The temperatures between 290 and 360 K were from crystals K1 and K4, and were used for both series. The evolution of the volume $V(T)$ at the temperatures between 265 and 90 K demonstrates the near perfect reversibility of the transition at T_{c_4}.

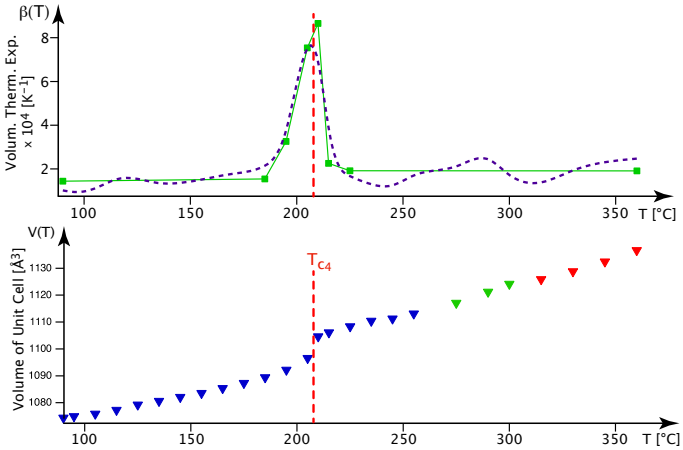

Figure S.45
The volume of the unit cell of the desmotrope **1**-B as a function of decreasing temperature. Blue ▼s refer to crystals K2, green ▼s to K1 and red ▼s to K4. T_{c_4} is the temperature of the I⟶II transition. The volumetric coefficient, β, of thermal expansion was computed as a numerical derivative (dashed dark violet curve) by the IGOR PRO program, Version 9, (WaveMetrics, 2021). The green curve ignores some small fluctuations.

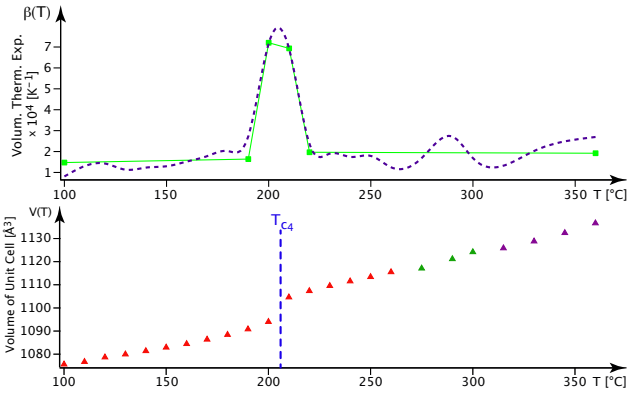

Figure S.46
The volume of the unit cell of the desmotrope **1**-B as a function of increasing temperature. Red ▲s refer to crystals K2, green ▲s to K1 and red ▲s to K4. T_{c_4} is the temperature of the I⟶II transition. The volumetric coefficient of thermal expansion, β, was computed as a numerical derivative (dashed dark violet curve) by the IGOR PRO program, Version 9, (WaveMetrics, 2021). The green curve ignores some small fluctuations.

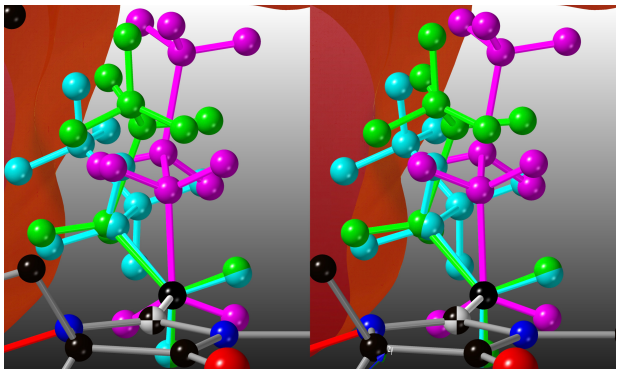

Figure S.47
View of the three conformers of the *n*.b.c.s in the desmotrope **1**-A. An interconversion of the turquoise and green conformers appears cheaper than one between the mauve and green ones.

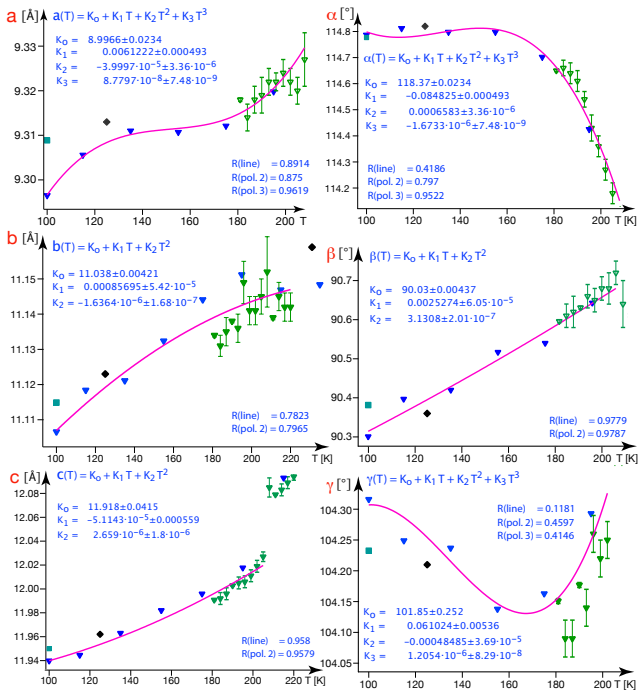

Figure S.48

The fitting of the six lattice parameters as functions of the temperature below T_{c4}. In each case the type of function is indicated, as well as the regression coefficients. Blue ▼s refer to crystal K2, green ▼s to crystal K3, black ◆s to the data collections using MoKα radiation and turquoise square to data from synchrotron LEBAIL-refinements.

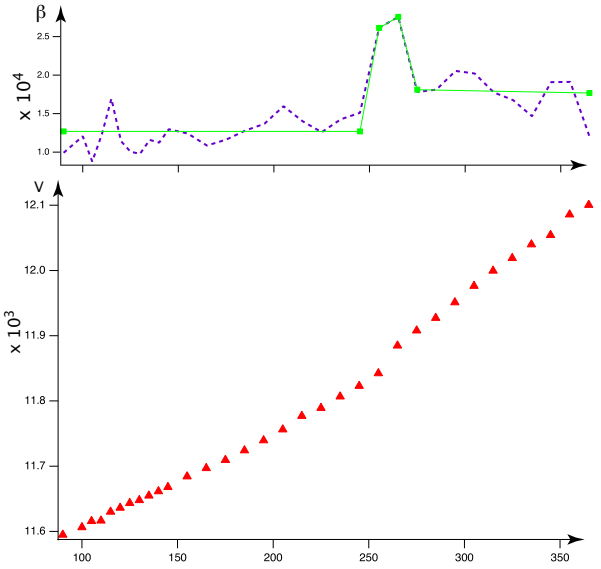

Figure S.49

The volume of the unit cell of the desmotrope **1**-A as a function of increasing temperature, as measured in the series *h1* and *h2*. Red ▲s refer to the crystal A5K. The volumetric coefficient, β, of thermal expansion was computed as a numerical derivative (dashed dark violet curve) by the IGOR PRO program, Version 9, (WaveMetrics, 2021). The green curve was calculated in a similar way, but ignores some small fluctuations.

A..6. Various Comments, Changes, Inspirations and Remarks

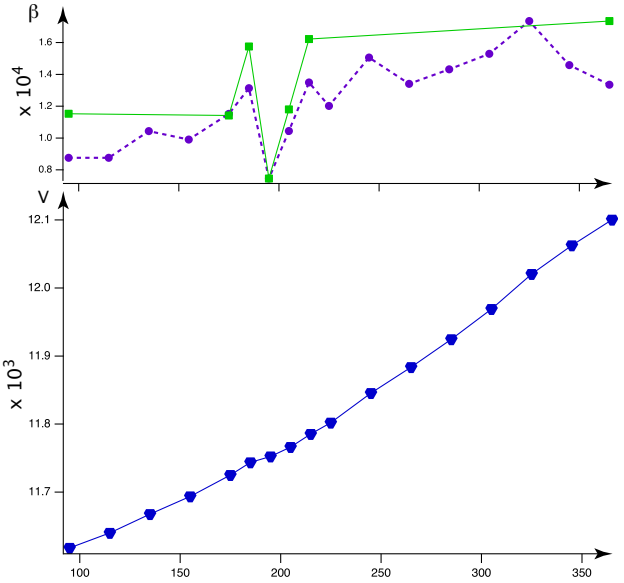

Figure S.50

The volume of the unit cell of the desmotrope **1**-A as a function of decreasing temperature. Blue ▼s refer to the series *c2* from the crystal A5K. The volumetric coefficient, β, of thermal expansion was computed as a numerical derivative (dashed dark violet curve) by the IGOR PRO program, Version 9, (WaveMetrics, 2021). The green curve was calculated in a similar way, but ignores some small fluctuations.

A careful inspection of the Figure S.53 might lead to some insight regarding the difference between the SS-NMR ^{15}N-spectra of the two desmotropes. Indeed, we see that the zig-zag plane of the major *n*.b.c. (mauve) is quite parallel to the plane of the Tet. But more importantly, we saw that both conformers of the *n*.b.c.s do not move much in **1**-A, in particular they do not interconvert into each other at all, at least below T_3 that is.

So, although each and every hydrogen atom of the *n*.b.c. presents a not so negligible interaction with a nitrogen on the Tet, these are stable and do not participate in any time-averaging at all. If one wanted to see modifications of the NMR-spectra, a measurement above T_3 would seem promising.

It appeared interesting to follow (Chattoraj & Sun, 2023)'s example and put our numerous l.p.s to good use for establishing the relative thermal stability of our polymorphs; we obtained a density-crossover-temperature T_d = 1750 K. Since T_d is much higher than even the end of the decomposition range, 533 K, (observed in **1**-B), the conversion between both desmoptropes in molten **1**, as postulated by (Skotnicki *et al.*, 2021), seems somewhat questionable.

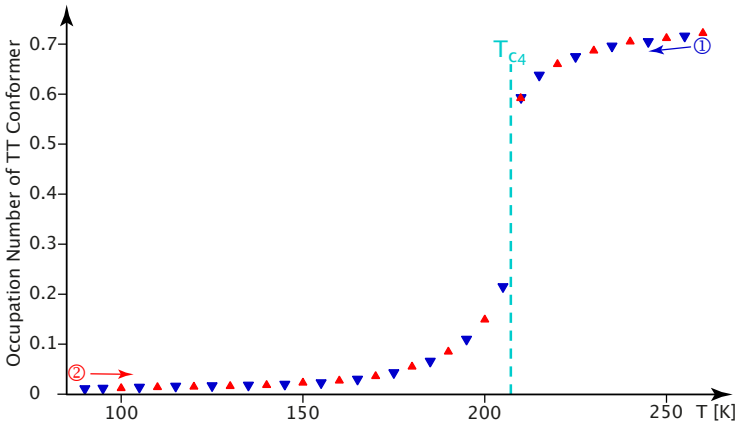

Figure S.51
A cycle of the th. ev. of the occupation number of the TT-chains in **1**-B: first cooling (blue ▼), then heating (red ▲). Data stem *all* from the crystal K2. The reversibility seems quite perfect indeed. Note that the occupation number could well be refined down to 90 K, and yielded significant s.u.s, *e.g.* 0.011(2) at the lowest temperature.

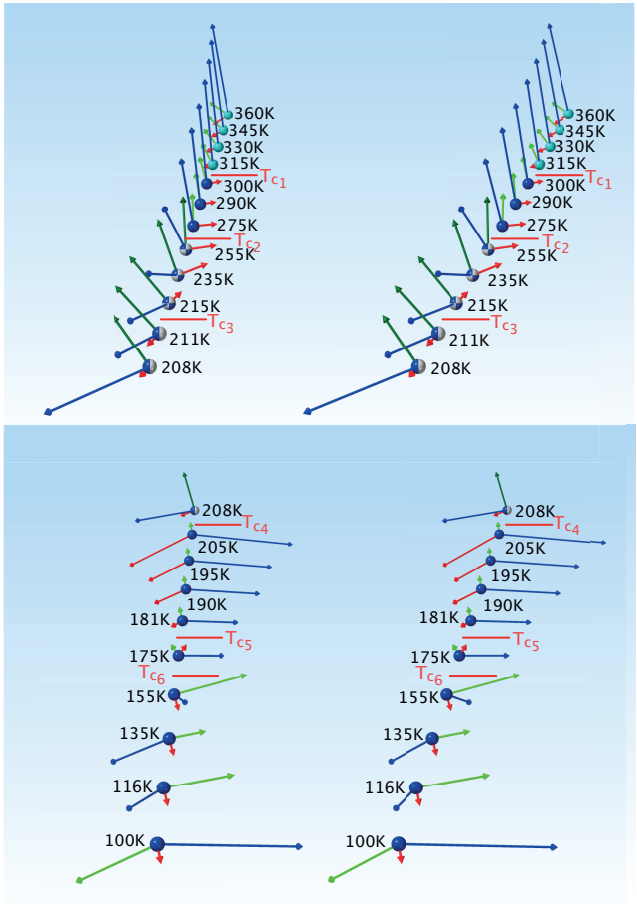

Figure S.52
Finer (than in Figure A.6) or different representation of the th. ev. of the tripods of the α-eigenvectors in **1**-B.

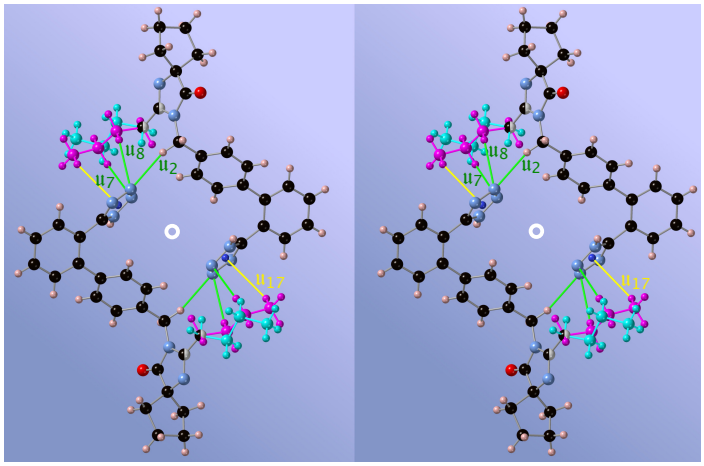

Figure S.53
The ≪open≫ dimer (also called *bagel*) linking two [001]-rods of molecules of **1** in the structure of the desmotrope **1**-A. The link is effectuated by the important PBC $\mathbf{u}_2$ and is further reinforced by the weak C–H···N interactions $\mathbf{u}_7$ and $\mathbf{u}_8$ (all in green) and a C–H···π interaction $\mathbf{u}_{17}$ (drawn in yellow). This convincingly illustrates that the major (mauve) chains mainly participate in interactions in the ≪**a**,**b**≫ plane The angle between the plane of the Tet and the zig-zag-plane of the *n*.b.c.s is 22.1° at 130 K, and the dihedral angles τ_0, τ_1, τ_2 and χ (dihedral angle between the *n*.b.c.s planes of the TT1/TT2) are 33.98, 51.34, 41.211 and 60.0°, respectively. The white circle represents the centre of inversion.

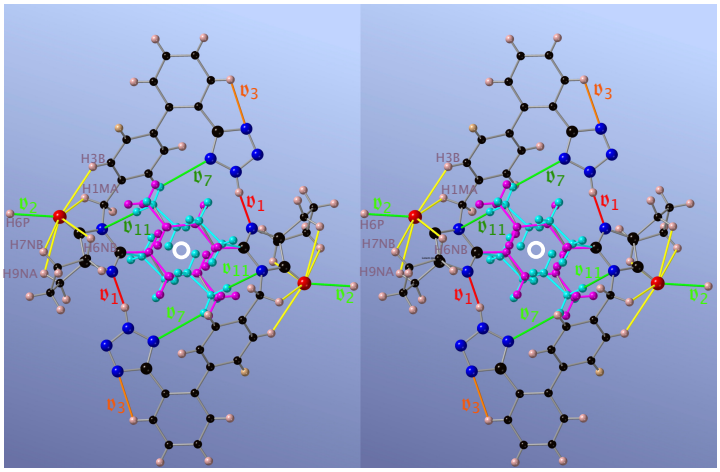

Figure S.55
The ≪closed≫ dimer (also referred to as *Madeleines*) linking two molecules of **1** in the structure of the desmotrope **1**-B. The ≪strongest≫ PBC $\mathbf{v}_1$ is show in red and represents the most crucial interaction for the growth of the Madeleines. Some important intradimer interactions are also indicated in green colour (such as the ominous $\mathbf{v}_7$ which shortens quite abruptly, by 0.2Å, at T_{c_4} = 208 K. The oxygen atom O1N contributes to the stability of the Madeleines by means of five intra-dimer C–H···O1N interactions of length 2.601 to 3.052Å, and to the lateral stability by the PBCs $\mathbf{v}_2$ and $\mathbf{v}_9$. The plane of the drawing is $\pi_M = (10\bar{1})$, and the dihedral angles τ_0, τ_1, τ_2 are 33.67, 27.99 and 24.00°, respectively. The open white circles represent centres of inversion. The drawing depicts the situation at T = 235 K.

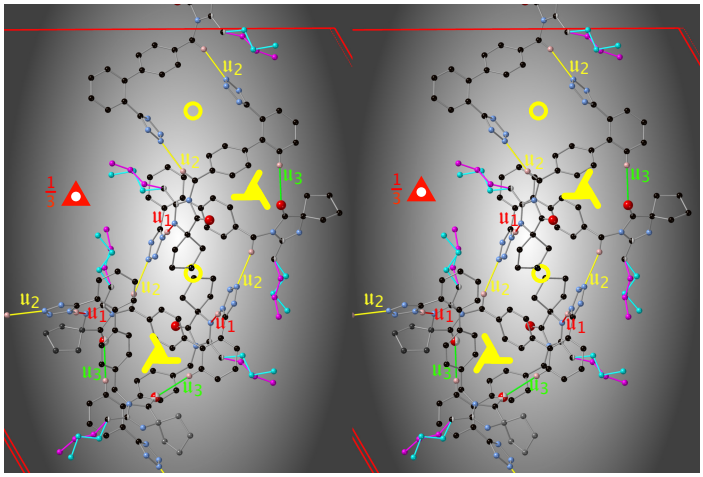

Figure S.54
The dimer linking two rods of molecules of **1** in the structure of the desmotrope **1**-A. The link is effectuated by the PBC $\mathbf{u}_2$ (drawn in yellow); more lateral cohesion is provided by the PBC $\mathbf{u}_3$ (green). The ≪strongest≫ PBC $\mathbf{u}_1$ is show in red and represents the most crucial interaction for the growth of the rod. The orange circles represent centres of inversion and the symbols for the two different screw rotations are quite self-explaining.

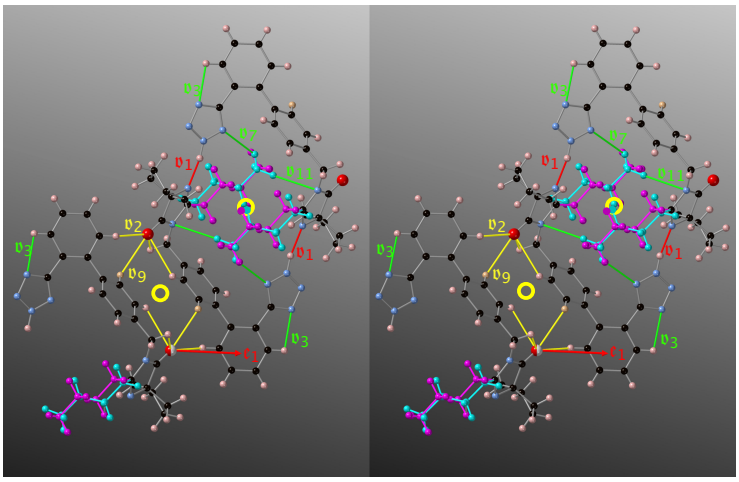

Figure S.56
The ≪closed≫ dimer (also referred to as *Madeleines*) linking two molecules of **1** in the structure of the desmotrope **1**-B, and its interaction with a nearest neighbour. The ≪strongest≫ PBC $\mathbf{v}_1$ is show in red and represents the most crucial interaction for the growth of the Madeleines. The lateral link is effectuated by the PBCs $\mathbf{v}_2$ and $\mathbf{v}_9$ (drawn in yellow); the angle between $\mathbf{e}_1$ and $\mathbf{r}_{O1N}$-$\mathbf{r}_{H6P}$ is 34.032°. Some important intradimer interactions are also indicated in green colour (such as the ominous $\mathbf{v}_6$ which shortens quite abruptly, by 0.2Å, at T_{c_4} = 208 K. The plane of the drawing is $\pi_M = (10\bar{1})$, the *red* vector $\mathbf{e}_1$ is the shortest eigenvector of the tensor of dilatation and the open yellow circles represent centres of inversion. The drawing depicts the situation at T = 235 K.

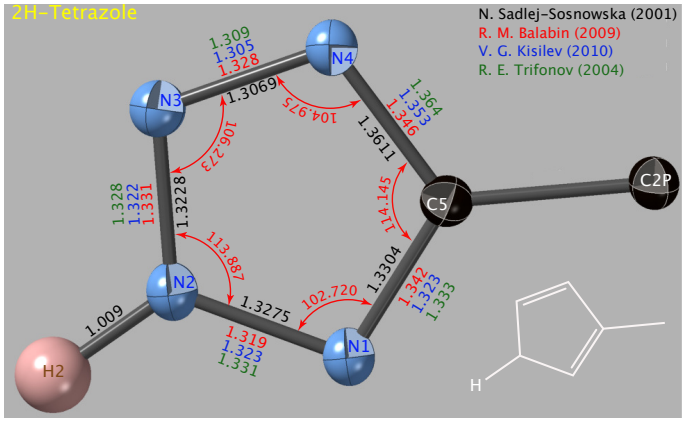

Figure S.57
The distances computed for the 2H-Tetrazole by Sosnowska in 2001 using the 6-1311++G** basis-set, and by Kisilev in 2010 using the method B3LYP/cc-pVTZ and by Balabin in 2009 using MP2(FC)/aug-cc-pVTZ, and by Trifonov in 2004 using B3LYP/6-31G*. The bond angles shown were computed from Balabin's distances.

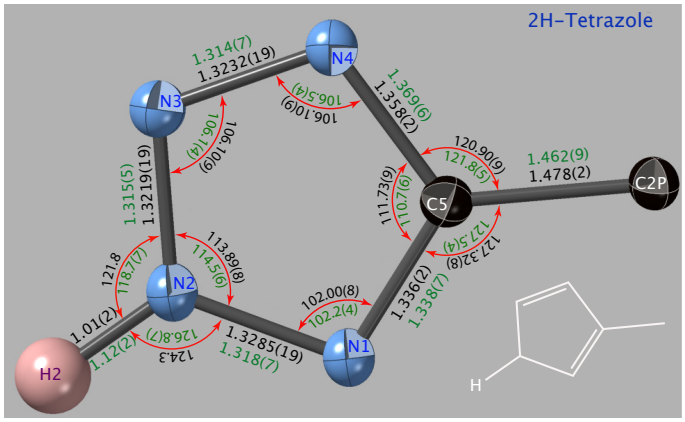

Figure S.58
The geometry of the tetrazole-ring in the desmotrope **1**-B. Black values are from X-rays at 125K and green ones from neutrons at 125K. The least-squares plane of the tetrazole can be described as $(40, 47, \overline{94})$, or accepting a deviation of 4.0°, as $(11\overline{2})$. Also note the quasi-isotropic displacement ellipsoids.

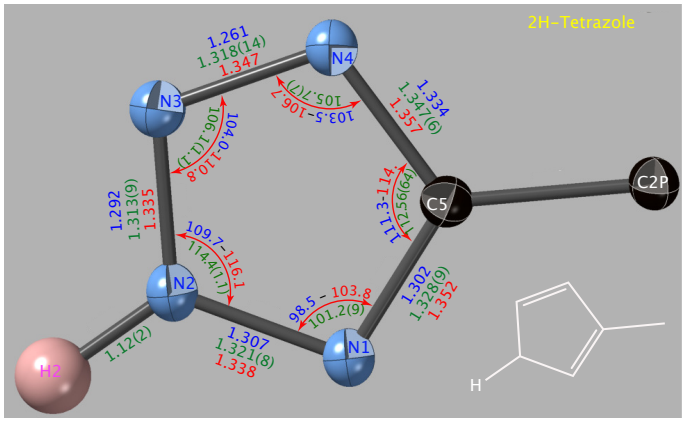

Figure S.59
The geometry of the tetrazole-ring in the desmotrope **1**-B from a search of 30 compounds in the CSD; the entry IDUQIJ was excluded because of ill assignments of atoms. Minimal values are blue, maximal ones red and average ones green.

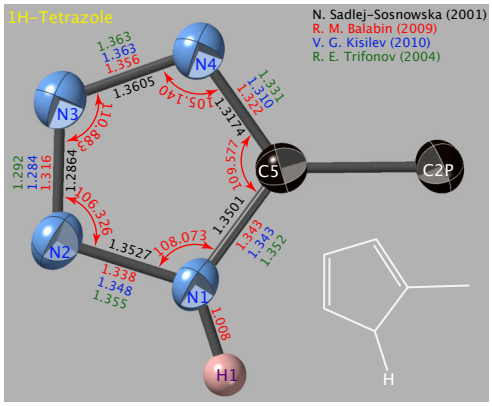

Figure S.60
The distances computed for the 1H-Tetrazole by Sosnowska in 2001 using the 6-1311++G** basis-set, and by Kisilev in 2010 using the method B3LYP/cc-pVTZ and by Balabin in 2009 using MP2(FC)/aug-cc-pVTZ, and by Trifonov in 2004 using B3LYP/6-31G*. The bond angles shown were computed from Balabin's distances.

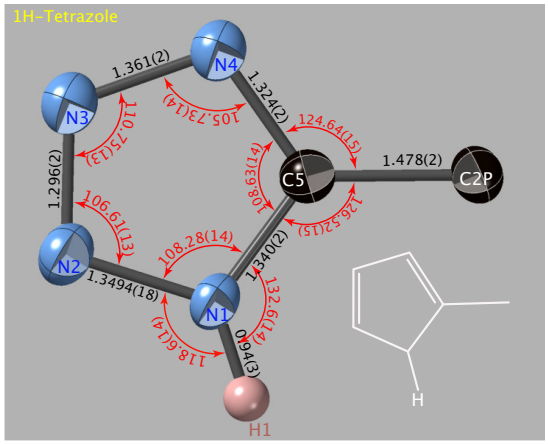

Figure S.61
The geometry of the tetrazole-ring in the desmotrope **1**-A. (From the data collection A1 at T=114K). The least-squares plane of the tetrazole is $(\overline{825}, 673, 1)$ with an SSE of 0.00001Å^2, or $(\overline{18}, 14, 1)$, accepting a deviation of 1.6°. The critical dihedral angles (Kellici *et al.*, 2016) are: τ_o = 36.112°, τ_1 = 52.1084°, τ_2 = 41.525°.

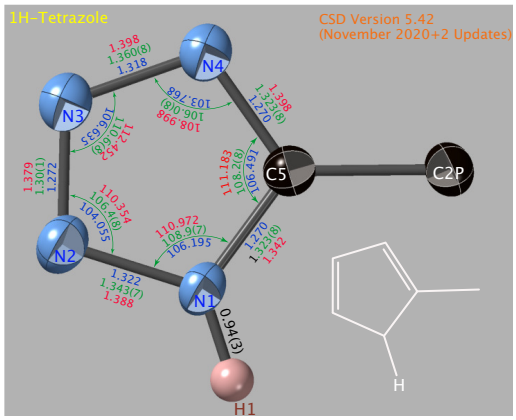

Figure S.62
The geometry of the tetrazole-ring in the desmotrope **1**-A from a search of 169 compounds in the CSD. Minimal values are blue, maximal ones red and average ones green.

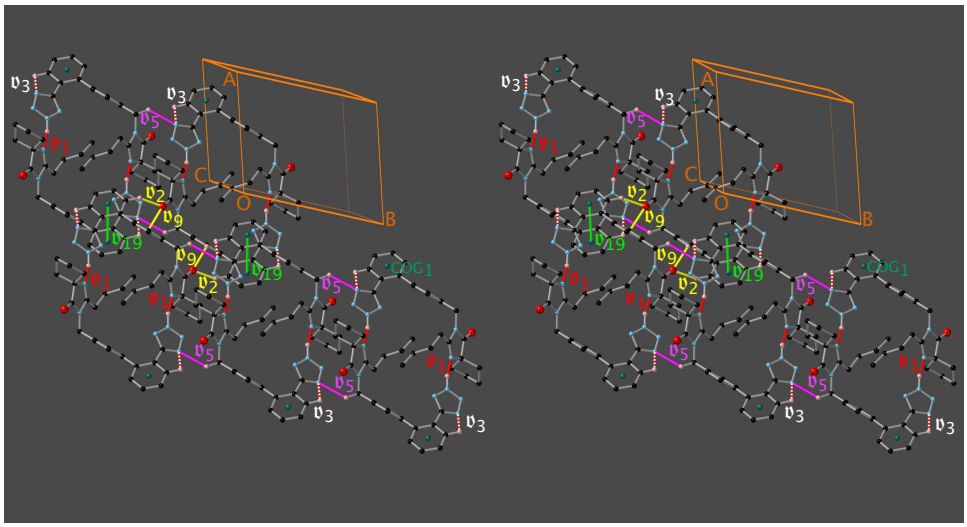

Figure S.63
Part of a $(10\bar{1})$-slice of a crystal of **1**-B at 125 K; the figure shows the interactions most responsible for the *layer-wise* growth of the desmotrope, but also one of the few interactions parallel to $[\bar{3}02]$, *i.e.* perpendicular to $(10\bar{1})$. *Inter*molecular interactions are depicted as full lines, *intra*molecular ones as red-white dashed lines, and, for clearness, only hydrogen atoms involved in interactions are displayed. The labels of the interactions are those given in Table S.15, and COG1 is the centroid of the phenyl C1P,...,C6P. C-H···O are in yellow C-H···N in violet, N-H···N in red, and π-π in green.

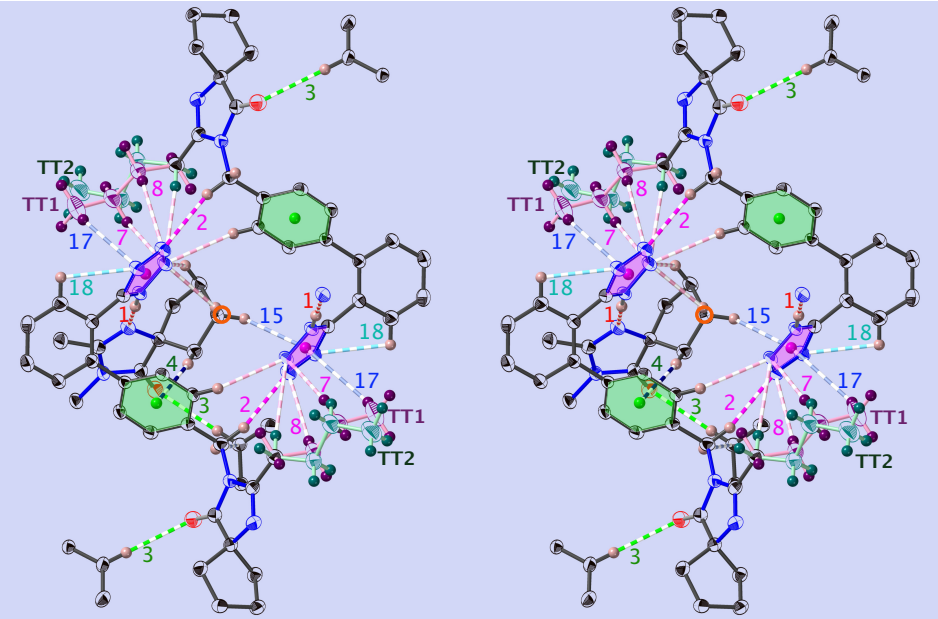

Figure S.64
Completer, stereoscopic version of the Figure 2 of the main text; most of the discussed, important interactions are labelled and displayed. The numbers of the interactions refer to the vectors $\mathbf{u}_j$ in the Table S.14. For clearness, only hydrogen atoms involved in interactions are displayed. The hexagonal, green planes refer to the centroid of the phenyl C1P,....,C6P (COG1), the pink pentagonal planes to that of the tetraazole (COG0). C-H···O are in green C-H···N in violet, N-H···N in red, and π-π in dark blue.

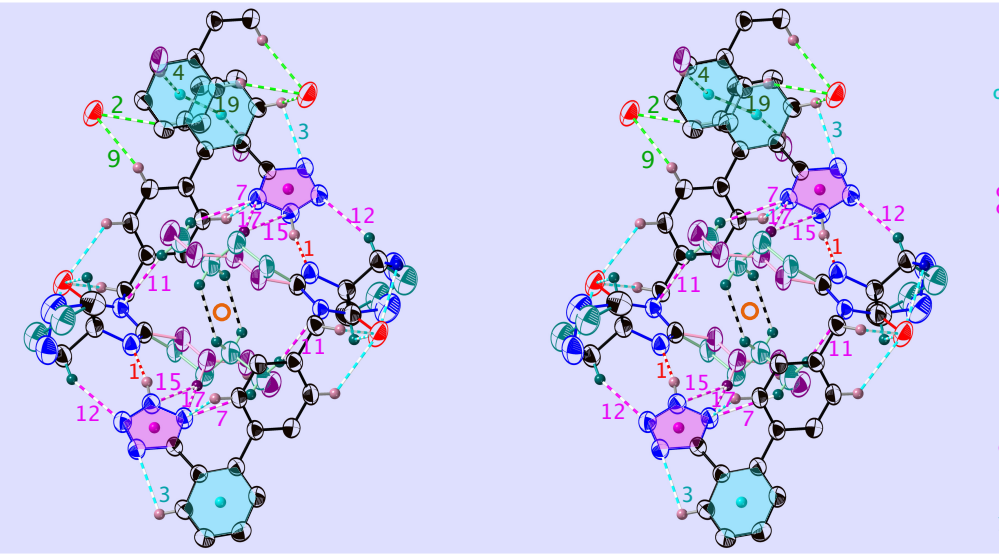

Figure S.65
Completer, stereoscopic version of the Figure 3 of the main text; most of the discussed, important interactions are labelled and displayed. The numbers of the interactions refer to the vectors $\mathbf{v}_j$ in the Table S.15. For clearness, only hydrogen atoms involved in interactions are displayed. The hexagonal, turquoise planes refer to the centroid of the phenyl C1P,....,C6P (COG1), the pink pentagonal planes to that of the tetrazole (COG0). C-H···O are in green C-H···N in violet, N-H···N in red, and π-π in dark green.

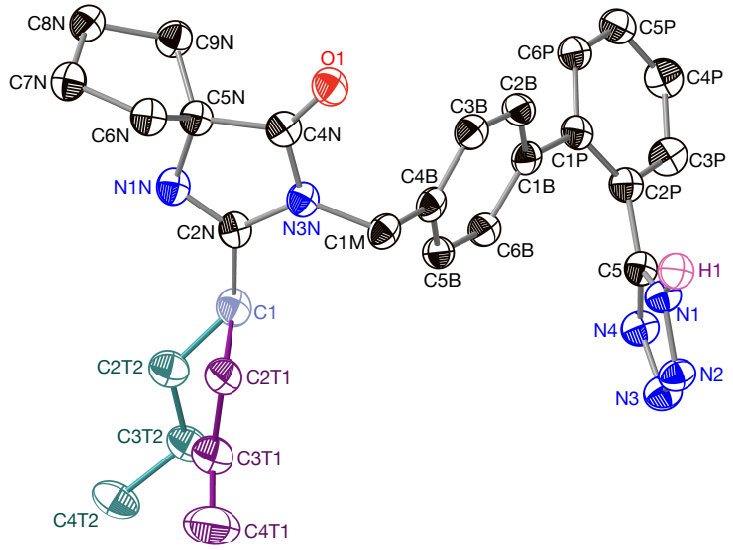

Figure S.66
The molecular structure of the desmotrope A of Irbesartan at T = 114 K; the ADP-ellipsoids enclose a probability of 0.4. For the sake of clearness, only the tetrazole-hydrogen is shown. The *n*-butyl-disorder, *i.e.* between **two** *all-trans* chains (T1:T2= 0.941(3):0.059(3)), are indicated by different colours of two molecules. The atom C1 is shared between the two chains. CAVEAT: some mild SADI and SIMU instructions were used for the *n*-butyl-chains.

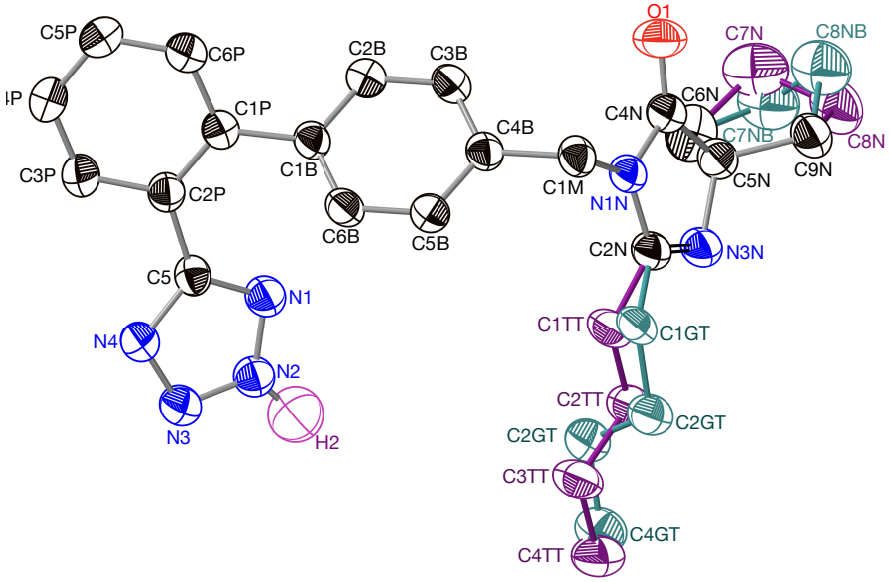

Figure S.67
The molecular structure of the desmotrope B of Irbesartan at T = 255 K; the ellipsoids enclose a probability of 0.4. For the sake of clearness, only the tetrazole-hydrogen is shown. The Cp- (C8N:C8NB=0.935(6):0.065(6)) and *n*-butyl-disorders (TT:GT=0.716(3):0.284(3)) are indicated by different colours of two molecules. CAVEAT: some mild SADI and SIMU instructions were used for the *n*-butyl-chains.

Table S.11
Principal directions of the tensor of thermal dilatation in **1**-B. Approximate directions are closer than 5 °.

T K	Largest Evalue	Approx. Direction	Medium Evalue	Approx. Direction	Smallest Evalue	Approx. Direct.	Shape of α-surface
360	16.890	[$\bar{3}\bar{1}$1]	4.3959	[$\bar{5}\bar{5}\bar{4}$]	-3.6516	[398]	peanut
345	16.339	[$\bar{3}\bar{1}$1]	4.2097	[$\bar{1}\bar{1}\bar{1}$]	-2.1831	[297]	peanut
330	15.665	[$\bar{3}\bar{1}$1]	4.2553	[$\bar{5}\bar{3}\bar{5}$]	-0.9920	[297]	peanut
315	14.843	[$\bar{3}\bar{1}$1]	4.5681	[$\bar{3}\bar{1}\bar{3}$]	-0.0846	[297]	peanut
300	13.861	[$\bar{3}\bar{1}$1]	5.120	[$\bar{7}\bar{0}\bar{9}$]	0.579	[0$\bar{3}\bar{2}$]	fat peanut
290	13.123	[$\bar{3}\bar{1}$1]	5.572	[$\bar{7}\bar{0}\bar{9}$]	0.930	[0$\bar{3}\bar{2}$]	fat peanut
275	11.932	[$\bar{3}\bar{1}$1]	6.271	[$\bar{7}\bar{0}\bar{9}$]	1.382	[0$\bar{3}\bar{1}$]	fat peanut
255	10.516	[$\bar{7}\bar{1}$6]	6.900	[$\bar{3}\bar{1}\bar{2}$]	1.861	[0$\bar{3}\bar{1}$]	erythrocyte
235	10.287	[$\bar{3}$18]	6.564	[$\bar{3}$0$\bar{1}$]	1.834	[$\bar{1}\bar{3}\bar{1}$]	erythrocyte
220	10.855	[$\bar{1}$15]	6.3774	[$\bar{6}\bar{1}\bar{1}$]	0.82444	[$\bar{2}\bar{4}\bar{1}$]	erythrocyte
217	11.002	[$\bar{1}$26]	6.4206	[$\bar{7}\bar{2}\bar{1}$]	0.49088	[$\bar{3}\bar{5}\bar{1}$]	erythrocyte
215	11.104	[$\bar{1}$27]	6.4643	[$\bar{7}\bar{2}\bar{1}$]	0.24647	[$\bar{3}\bar{5}\bar{1}$]	erythrocyte
214	11.155	[$\bar{1}$27]	6.4902	[$\bar{7}\bar{2}\bar{1}$]	0.11809	[$\bar{3}\bar{4}\bar{1}$]	erythrocyte
211	11.314	[$\bar{1}$27]	6.5839	[$\bar{8}\bar{3}\bar{1}$]	-0.29007	[$\bar{4}\bar{5}\bar{1}$]	erythrocyte
208	11.478	[$\bar{1}$28]	6.6992	[$\bar{9}\bar{4}\bar{1}$]	-0.73048	[$\bar{4}\bar{5}\bar{1}$]	erythrocyte
205	41.807	[011]	5.5516	[$\bar{2}\bar{0}\bar{1}$]	-14.664	[33$\bar{1}$]	wasp-peanut
202	38.602	[011]	4.8871	[$\bar{2}\bar{0}\bar{1}$]	-12.79	[33$\bar{1}$]	wasp-peanut
199	35.526	[011]	4.2592	[$\bar{2}\bar{0}\bar{1}$]	-11.002	[33$\bar{1}$]	wasp-peanut
196	32.581	[011]	3.6681	[$\bar{2}\bar{0}\bar{1}$]	-9.3006	[33$\bar{1}$]	wasp-peanut
195	31.63	[011]	3.4793	[$\bar{2}\bar{0}\bar{1}$]	-8.7527	[33$\bar{1}$]	wasp-peanut
193	29.77	[011]	3.1138	[$\bar{2}\bar{0}\bar{1}$]	-7.6837	[33$\bar{1}$]	wasp-peanut
190	27.092	[011]	2.5965	[$\bar{2}\bar{0}\bar{1}$]	-6.1516	[33$\bar{1}$]	wasp-peanut
187	24.553	[$\bar{1}$77]	2.1159	[$\bar{2}\bar{0}\bar{1}$]	-4.7034	[33$\bar{1}$]	wasp-peanut
184	22.154	[$\bar{1}$77]	1.6726	[$\bar{2}\bar{0}\bar{1}$]	-3.3399	[33$\bar{1}$]	wasp-peanut
181	19.896	[$\bar{1}$77]	1.2674	[$\bar{2}\bar{0}\bar{1}$]	-2.0618	[33$\bar{1}$]	wasp-peanut
175	15.817	[$\bar{1}$78]	0.65076	[$\bar{3}\bar{2}\bar{2}$]	0.15239	[210]	wasp-peanut
165	10.427	[$\bar{1}$35]	3.2735	[$\bar{5}\bar{9}$1]	-0.33621	[$\bar{3}$0$\bar{1}$]	peanut
155	7.7271	[$\bar{4}$07]	4.3161	[$\bar{1}\bar{2}\bar{1}$]	-0.80942	[$\bar{3}\bar{1}\bar{1}$]	erythrocyte
135	8.7925	[$\bar{7}\bar{5}$4]	2.0839	[$\bar{1}\bar{3}\bar{2}$]	-0.48174	[$\bar{3}\bar{1}\bar{1}$]	fat peanut
116	8.2691	[$\bar{7}\bar{3}$5]	3.9643	[$\bar{1}\bar{3}\bar{2}$]	1.5804	[$\bar{3}$12]	erythrocyte
100	11.484	[$\bar{6}$56]	6.5142	[$\bar{9}\bar{7}\bar{4}$]	1.8762	[3$\bar{5}\bar{5}$]	erythrocyte

Table S.12
Forms of **1** crystallising from various solvents and pH-values.

Solvent		Method	Reference
Chloroform	A	Excess of A- and B-forms of **1** in 50:50 proportion	(Araya-Sibaja *et al.*, 2019*b*)
Ethyl Acetate	A	was stirred at 25 or 40 °C for 72 h, then the liquid	
Isopropyl Alcohol	A	was removed and the solids dried at 60° for 1 hour.	
Acetone	A	Same outcome for both temperatures.	
Ethanol	A		
Methanol	A		
Nitromethane	B		
Acetonitrile	B		
DMF	B		
Water	B		
DMSO	B		
MeOH	A/B	A for 2 > pH, but B at pH ⩽ 2.	
Water	B	At all 3 < pH < 11 values.	
Methanol	A	SR47436A-Lot 93-06 was recrystallised at room temperature, then filtered through a 200nm nylon filter and let to evaporate at 298K.	(Bauer *et al.*, 1998)
HCl/H_2O, pH=2	B	A slurry of SR47436A-Lot 93-06 in form A was stirred for 36 hours at room temperature, then filtered through a 200 nm filter and left to dry at 298 K.	(Bauer *et al.*, 1998)
Ethanol/water	B	2 mm-sized crystals of B from a mixture of $EtOH/H_2O$ $(80:20)$wt% with a seed-crystal of 100 μm and a temperature-gradient of $-1\,^{\circ}\,h^{-1}$.	(Garcia, 2000)
2-propanol	A	Evaporation at room temperature	(Garcia *et al.*, 2002)
Ethanol	A	Evaporation yields small and twinned crystals	*this work, 2006*
Ethanol/water	A	Diffusion of $EtOH/H_2O$ into water in sealed tube	*this work, 2006*
Ethanol/water	A,B	if 10% ⩽c(H_2O)⩽ 60%	*this work, 2006*
Ethanol/water	B	if c(H_2O)⩾ 60%	*this work, 2006*
Ethanol/HCl	B	if EtOH/HCl = 1:3, T=40C° and pH=0	*this work, 2006*
2-propanol	A	From a solution of **1** by evaporation	(Taulelle *et al.*, 2009)
Ethanol/water	B	From a solution of **1** in $EtOH/H_2O(80:20)$wt%.	(Taulelle *et al.*, 2009)
2-propanol	A	By drying an Irbsartan Isopropanolate obtained by crystallising **1** from 2-propanol.	(Delaney *et al.*, 2012)
Water	B	By slurrying form A in water	(Delaney *et al.*, 2012)
Water	B	By slurrying form A in hot water, and a few drops of hydrochloric acid	P.O. 2006
Ethanol	A&B	Slow evaporation of a solution of **1**	(Delaney *et al.*, 2012)

Table S.13
Solubilities of the forms of **1** in various solvents or solvent-mixtures.

Form	Solvent(s) Vol%	Tempe-rature [K]	$10^5 \cdot x_1$	x_2	g per 100g of solvent	$mg \cdot ml^{-1}$	Reference
A	Acetone	293.60	53	0.99947	0.3913	3.069	(Wang *et al.*, 2007*a*)
A	Acetone	293.15			0.40		(Garcia, 2000)
A	Ethanol	292.70	80.9	0.99919	0.753	5.945	(Wang *et al.*, 2007*a*)
A	Chloroform	292.70	161.5	0.99838	0.5807	8.6468	(Wang *et al.*, 2007*a*)
A	Chloroform	293.15			1.31		(Garcia, 2000)
A	Water	293.15				0.050	(Garcia, 2000)
A	2-Propanol	293.15			0.28		(Garcia, 2000)
A	2-Propanol	291.15	50.0		0.357	2.782	(Taulelle *et al.*, 2006)
A	Methanol	293.15			1.67	0.357	(Garcia, 2000)
A	Dioxane	293.45	63.4	0.99937	0.30855	3.178	(Wang *et al.*, 2007*a*)
A	THF	292.95	229.4		1.3665	12.150	(Wang *et al.*, 2007*a*)
A	DMF	293.15				14.0	CAYMAN Chemicals
A	DMSO	293.15				20.0	CAYMAN Chemicals
B	Water	293.15				0.015	(Garcia, 2000)
?	Water	298.15				0.08(5)	Patel
B	Water					0.00884	Ali Nasr
B	Water					0.012	Mohapatra
B?	Ethanol					0.5	CAYMAN Chemicals
B	EtOH : H_2O 90:10	293.15	6.27	0.7357	0.2642373	0.5633	(Gao & Tian, 2008)
B	EtOH : H_2O 80:20	293.15	3.964	0.5531	0.4468604	0.422	(Gao & Tian, 2008)

Table S.14
Normalised [to d(C—H)=1.089Å, except d(N1—H1) which was refined to 0.977(17)Å] hydrogen bonds (Å, °) in **1**-A at T=90 K. COG0 is the centre of gravity of the tetrazole, COG1 that of the phenyl C1B,⋯,C6B.

D − H⋯A	H⋯A	D⋯A	∠DHA	PBC/HB
N1 − H1⋯N1N^{p2}	1.758(17)	2.7335(17)	176.1(17)	$\mathbf{u}_1$ = [109]
C1M − H1MA⋯N3^{p5}	2.434(2)	3.466(2)	157.7	$\mathbf{u}_2$ = [20$\bar{1}$]
C6P − H6P⋯O1N^{p1}	2.499	3.576(2)	170.1	$\mathbf{u}_3$ = [1$\bar{1}$0]
C9N − H9NA⋯COG1^{p1}	2.625	3.697	167.9	$\mathbf{u}_4$ = [*uvw*]
C8N − H8NA⋯N2^{p1}	2.668	3.496(2)	132.4	$\mathbf{u}_5$ = [*uvw*]
C8N − H8NB⋯N4^{p4}	2.697	3.669(2)	148.5	$\mathbf{u}_6$ = [*uvw*]
C3T1 − H3TB⋯N2^{p5}	2.698	3.399	121.7	$\mathbf{u}_7$ = [$\bar{2}$19]
C2T1 − H2TA⋯N3^{p5}	2.705	3.600	139.1	$\mathbf{u}_8$ = [*uvw*]
C5P − H5P⋯N3^{p3}	2.713	3.291(2)	112.7	$\mathbf{u}_9$ = [018]
C8N − H8NB⋯N3^{p4}	2.715	3.388(2)	119.6	$\mathbf{u}_{10}$ = [11$\bar{2}$]
C5B − H5B⋯N2^{p5}	2.727	3.600	136.9	$\mathbf{u}_{11}$ = [$\bar{4}$1$\bar{6}$]
C5P − H5P⋯N4^{p3}	2.787	3.512	123.8	$\mathbf{u}_{12}$ = [*uvw*]
C1 − H1AB⋯C2P^{p1}	2.798	3.837	159.6	$\mathbf{u}_{13}$ = [*uvw*]
C1 − H1AB⋯C1P^{p1}	2.815	3.633	131.3	$\mathbf{u}_{14}$ = [*uvw*]
C8N − H8NB⋯COG0^{p4}	2.817	3.594	128.2	$\mathbf{u}_{15}$ = [*uvw*]
C1 − H1BC⋯N2^{p5}	2.857	3.893	159.1	$\mathbf{u}_{16}$ = [*uvw*]
C4T1 − H4TB⋯COG0^{p5}	2.944	3.790	134.8	$\mathbf{u}_{17}$ = [$\bar{2}$13]
C3P − H3P⋯N4	2.709(2)	2.984(3)	93.6	$\mathbf{u}_{18}$ = [*uvw*]

Symm. Ops : **p1** $\frac{2}{3} - y, \frac{1}{3} + x - y, \frac{1}{3} + z$ **p2** $\frac{1}{3} - x + y, \frac{2}{3} - x, -\frac{1}{3} + z$
p3 $\frac{1}{3} + x - y, -\frac{1}{3} + x, \frac{5}{3} - z$ **p4** $-\frac{1}{3} + y, \frac{1}{3} - x + y, \frac{4}{3} - z$
p5 $1 - x, 1 - y, 1 - z$

Table S.15
Normalised hydrogen bonds (Å,°) in **1**-B at T=215 K, based on fixed C—H distances of 1.089Å and a refined N2—H2 distance of 0.99(2)Å. COG0 is the centre of gravity of the tetrazole, COG1 that of the phenyl C1P,⋯,C6P.

D − H⋯A	H⋯A	D⋯A	∠D, H, A	PBC/HB
N2 − H2⋯N1N^{j1}	1.766(2)	2.768(2)	169(2)	$\mathbf{v}_1$ = [312]
C6P − H6P⋯O1N^{j2}	2.333	3.288(2)	145.0	$\mathbf{v}_2$ = [011]
C3P − H3P⋯N4	2.488	2.849(2)	97.84	$\mathbf{v}_3$ = [314]
C3TT − H3TA⋯COG1^{j4}	2.499(1)	3.553(9)	162.53(1)	$\mathbf{v}_4$ = [30$\bar{2}$]
C1M − H1MB⋯N4^{j4}	2.580(8)	3.64(1)	165.2	$\mathbf{v}_5$ = [1$\bar{1}\bar{2}$]
C5B − H5B⋯COG0^{j4}	2.592(7)	3.534(2)	144.32	$\mathbf{v}_6$ = [3$\bar{1}\bar{3}$]
C4GT − H4GB⋯N1^{j1}	2.697(1)	3.62(1)	142(3)	$\mathbf{v}_7$ = [5$\bar{8}\bar{4}$]
C1M − H1MB⋯N3^{j4}	2.676(7)	3.57(1)	139.4	$\mathbf{v}_8$ = [20$\bar{1}$]
C2B − H2B⋯O1N^{j2}	2.682	3.478(2)	129.5	$\mathbf{v}_9$ = [111]
C1M − H1MA⋯N4^{j5}	2.827(5)	3.351(4)	109.5	$\mathbf{v}_{10}$ = [02$\bar{1}$]
C4GT − H4GC⋯N3N^{j1}	2.831(1)	3.91(9)	169.9(3)	$\mathbf{v}_{11}$ = [$\bar{4}\bar{7}$3]
C9N − H9NB⋯N3^{j1}	2.885(1)	3.634(9)	125.98(3)	$\mathbf{v}_{12}$ = [$\bar{4}\bar{7}$3]
C9N − H9NA⋯N2^{j5}	2.842(1)	3.430(9)	113.85(3)	$\mathbf{v}_{13}$ = [$\bar{4}\bar{7}$3]
C1GT − H1GA⋯N4^{j4}	2.955	3.506(2)	111.60	$\mathbf{v}_{14}$ = [311]
C2TT − H2TA⋯N2^{j1}	2.717	3.387(2)	119.45	$\mathbf{v}_{15}$ = [311]
C1GT − H1GB⋯N4^{j4}	3.030	3.506(2)	106.93	$\mathbf{v}_{16}$ = [100]
C2TT − H2TA⋯N1^{j1}	2.732	3.424(2)	121.04	$\mathbf{v}_{17}$ = [100]
C3P − H3P⋯O1N^{j3}	3.046(1)	3.739(2)	121.98(1)	$\mathbf{v}_{18}$ = [$\bar{2}$10]
COG1⋯COG1^{j6}		3.813(1)		$\mathbf{v}_{19}$ = [9$\bar{1}\bar{6}$]

Symm. Ops : **j1** −x, 1 − y, 1 − z **j2** 1 − x, 2 − y, 2 − z
j3 x, −1 + y, z **j4** 1 − x, 1 − y, 1 − z
j5 x, 1 + y, z **j6** 1 − x, 1 − y, 2 − z

References

Alkorta, I., Rozas, I. & Elguero, J. (1998). *J. Chem. Soc., Perkin Trans. 2*, pp. 2671–2675.

Allen, F. H., Groom, C. R., Liebeschuetz, J. W., Bardwell, D. A., Olsson, T. S. G. & Wood, P. A. (2012). *J. Chem. Info. Model.* **52**, 857–866.

Araya-Sibaja, A. M., de Campos, C. E. M., Fandaruff, C., Vega-Baudrit, J. R., Guillén-Girón, T., Navarro-Hoyos, M. & Cuffini, S. L. (2019*a*). *J. Pharmaceut. Anal.* **9**, 339–346.

Araya-Sibaja, A. M., Urgellés, M., Vásquez-Castro, F., Vargas-Huertas, F., Vega-Baudrit, J. R., Gullén-Girón, T., Navarro-Hoyos, M. & Cuffini, S. L. (2019*b*). *RSC Adv.* **9**, 5244–5250.

Balabin, R. M. (2009). *J. Chem. Phys.* **131**, 154307–1–154307–8.

Bartolucci, G., Bruni, B., Di Vaira, M. & Giannellini, V. (2007). *Acta Cryst. E*, pp. o1529–o1531.

Bauer, M., Harris, R. K., Rao, R. C., Apperley, D. C. & Rodger, C. A. (1998). *J. Chem. Soc., Perkin Trans. 2*, pp. 475–481.

Bernhart, C. A., Perreaut, P. M., Ferrari, B. P., Muneaux, Y. A., Assens, J.-L. A., Clément, J., Haudricourt, F., Muneaux, C. F., Taillades, J. E., Vignal, M.-A., Gougat, J., Guiraudou, P. R., Lacour., C. A., Roccon, A., Cazaubon, C. F., Brelière, J.-C., Le Fur, G. & Nisato, D. (1993). *J. Med. Chem.* **36**, 3371–3380.

Bernstein, J. (2011). *Crystal Growth & Des.* **11**, 632–650.

Bezard, J.-P. & El-Hajji, M., (1998). Personal communication.

Bhatt, P. M. & Desiraju, G. R. (2007). *Acta Cryst.* pp. 2057–2059.

Blake, A. J., Lin, X., Schröder, M., Wilson, C. & Yuan, R.-X. (2004). *Acta Cryst.* C**60**, o226–o228.

Böcskei, Z., Simon, K., Rao, R., Caron, A., Rodger, C. A. & Bauer, M. (1998). *Acta Cryst. C*, pp. 808–810.

Boutonnet-Fagegaltier, N., Menegotto, J., Lamure, A., Duplaa, H., Caron, A., Lacabanne, C. & Bauer, M. (2002). *J. Pharmaceut. Sci.* pp. 1548–1560.

Bozal, B., Doğan-Topal, B., Uslu, B., Özkan, S. A. & Aboul-Enein, H. Y. (2009). *Analytical Letters*, **42**, 2322–2338.

Bravais, A. (1866). *Études cristallographiques*. Gauthier-Villars, Paris.

Brochier, D. & Pujol, S. (1977). *Cryostat à température variable pour mesures neutroniques ou optiques*. Tech. rep. Institut Laue-Langevin. 77/74.

Brovarets, O. O., Yurenko, Y. P. & Hovorun, D. M. (2014). *J. Biomol. Struct. Dyn.* **32**, 993–1022.

BRUKER INSTR. SERV., (2016). *Program for Running and Interpreting a Data Collection*. Bruker AXS, GmbH, Östliche Rheinbrückenstraße, D-76187 Karlsruhe. V2016.5.0.1.

Campbell, J., Habash, J., Helliwell, J. R. & Moffat, K. (1986). In *CCP4 Newsletter*, vol. 18 of *Information Quarterly for Protein Crystallography*, pp. 23–31. Warrington, England: Daresbury Laboratory.

Campbell, J. W. (1995). *Journal of Applied Crystallography*, **28**(2), 228–236.
URL: *https://doi.org/10.1107/S002188989400991X*

Campbell, J. W., Hao, Q., Harding, M. M., Nguti, N. D. & Wilkinson, C. (1998). *Journal of Applied Crystallography*, **31**(3), 496–502.
URL: *https://doi.org/10.1107/S0021889897016683*

Cazaubon, C., Gougat, J., Bousquet, F., Guiraudou, P., Gayraud, R., Lacour, C., Roccon, A., Galindo, G., Barthelemy, G., Gautret, B., Bernhart, C., Perreaut, P., Breliere, J.-C., Le Fur, G. & Nisato, D. (1993). *J. of Pharmacol. and Exp.Therap.* **265(2)**, 826–834.

Chandrappa, R. K. (2011). *Caractérisation de formulations pharmaceutiques par* RMN *de l'état solide: Polymorphisme et Déformulation*. Master's thesis, Université de Versailles, Saint-Quentin-en-Yvelines.

Chattoraj, S. & Sun, C. C. (2023). *Crystals.* **13**, 270–283.

Cruz-Cabeza, A. J. & Groom, C. R. (2011). *CrystEngComm*, **13**, 93–98.

Custelcean, R. & Jackson, J. E. (2001). *Chem. Rev.* **101**, 1963–1980.

Dale, B. L., Halcovitch, N. R., Peach, M. J. G. & Griffin, J. M. (2019). *Magn. Reson. Chem.* **57**, 230–242.

Delaney, S. P., Pan, D., Galella, M., Yin, S. X. & Korter, T. M. (2012). *Crystal Growth & Design*, **12**, 5017–5024.

Desiraju, G. R. (2008). *Crystal Growth & Design*, **8**, 3–5.

Dolomanov, O. V., Bourhis, L. J., Gildea, R. J., Howard, J. A. K. & Puschmann, H. (2009). *J. Appl. Cryst.* **42**, 339–341.

Donnay, J. D. H. & Harker, D. (1937). *Am. Mineral.* **22**, 446–467.

Elguero, J. (2011). *Crystal Growth & Design*, **11**, 4731–4738.

Eltayeb, N. E., Teoh, S. G., Quah, C. K., Fun, H.-K. & Adnan, R. (2009). *Acta Cryst.* E**65**, o1613–o1614.

FaceIt, (2016). *Program for Viewing and Indexing Crystals*. Stoe & Cie GmbH, Hilpertstraße 10 , 64295 Darmstadt, Deutschland. Version 1.35b p3i.

Filip, L. A., Caira, M. R., Fărcaş, S. I. & Bojiţă, M. T. (2001). *Acta Cryst.* C**57**, 435–436.

Fortes, A. D., Knight, K. S. & Wood, I. G. (2017). *Acta Cryst.* B**73**, 47–64.

Franca, C. A., Etcheverry, S. B., Diez, R. P. & Williams, P. A. M. (2009). *J. Raman Spectrosc.* **40**, 1296–1300.

Friedel, G. (1907). *Bull. Soc. Fr. Miner.* **30**, 326–455.

Gao, Y. & Tian, J. (2008). *J. Chem. Eng. Data*, **53**, 535–537.

Garcia, E. (2000). *Étude de la dissolution et de la croissance de principes actifs*. Ph.D. thesis, Université d'Aix-Marseille III, Aix-en-Provence, Marseille. "Thèse de doctorat dirigée par Veesler, Stéphane, Génie des procédés et physicochimie, Aix-Marseille III 2000".

Garcia, E., Hoff, C. & Veesler, S. (2002). *J. Cryst. Growth*, **237-239**, 2233–2239.

Gauto, D. F., Lebedenko, O. O., Becker, L. M., Ayala, I., Lichtenecker, R., Skrynnikov, N. R. & Schanda, P. (2022). Aromatic ring flips in differently packed ubiquitin protein crystals from MAS NMR and MD. Working paper or preprint.
URL: *https://hal.archives-ouvertes.fr/hal-03863723*

Glendening, E. D. & Weinhold, F. (2021). *Molecules*, **26(14)**, 4110.

Groom, C. R., Bruno, I. J., Lightfoot, M. P. & Ward, S. C. (2016). *Acta Cryst.* B**72**, 171–179.

Haiges, R. & Christe, K. O. (2015). *Dalton Trans.* **44**, 10166–10176.

Hamilton, W. C. & Abrahams, S. C. (1970). *Acta Crystallogr.* A**26**, 18–24.

Hartman, P. & Perdok, W. G. (1955*a*). *Acta Cryst.* **8**, 49–52.

Hartman, P. & Perdok, W. G. (1955*b*). *Acta Cryst.* **8**, 521–524.

Jansook, P., Muankaew, C., Stefánsson, E. & Loftsson, T. (2015). *Pharmaceutical Development and Technology*, **20**(5), 626–632.
URL: *https://doi.org/10.3109/10837450.2014.910811*

Kadro, J. M., Nonomura, K., Gachet, D., Grätzel, M. & Hagfeldt, A. (2015). *Scientific Reports*, **06**, 11654.

Kellici, T. F., Ntountaniotis, D., Kritsi, E., Zervou, M., Zoumpoulakis, P., Potamitis, C., Durdagi, S., Salmas, R. E., Ergun, G., Godkemir, E., Halabalaki, M., Gerothanassis, I. P., Liapakis, G., Tzakos, A. & Mavromoustakos, T. (2016). *Current Medicinal Chemistry*, **23**, 36–59.

Kern, R. (1990). *Croissance de Cristaux*, vol. 6, p. 800. ENCYCLOPEDIA UNIVERSALIS.

Khan, S. & Reshak, A. (2013). *International journal of electrochemical science*, **8**, 9459.

Kiselev, V. G., Cheblakov, P. B. & Gritsan, N. P. (2011). *J. Phys. Chem. A*, **115**, 1743–1753.

Klein, J., Khartabil, H., Boisson, J. C., Contreras-Garcia, J., Piquemal, J.-P. & Henon, E. (2020). *J. Phys. Chem. A.* **124**, 1850–1860.

Langreiter, T. & Kahlenberg, V. (2015). *Crystals*, **5**, 143–153.

Lehmann, M. S. & Larsen, F. K. (1974). *Acta Cryst. A*, **30**, 580–584.

Liossi, A. S., Ntountaniotis, D., Kellici, T. F., Chatziathanasiadou, M. V., Megariotis, G., Mania, M., Becker-Baldus, J., Kriechbaum, M., Krajnc, A., Christodoulou, E., Glaubitz, C., Rappolt, M., Amenitsch, H., Mali, G., Theodorou, D. N., Valsami, G., Pitsikalis, M., Iatrou, H., Tzakos, A. G. & Mavromoustakos, T. (2017). *Biochem. and Biophys. Acta*, **1859**, 1089–1098.

Macrae, C. F., Edgington, P. R., McCabe, P., Pidcock, E., Shields, G. P., Taylor, R., Towler, M. & van de Streek, J. (2006). *J. Appl. Cryst.* **39**, 453–457.

McIntyre, G. J., Lemée-Cailleau, M.-H. & Wilkinson, C. (2006). *Physica B*, **385-386**, 1055–1058.

Mishra, M. K., Ramamurty, U. & Desiraju, G. R. (2015). *J. Am. Chem. Soc.* **137**, 1794–1797.

Nayak, S. K., Sathishkumar, R. & Row, T. N. G. (2010). *Chem. Eng. Comm.* **12**, 3112–3118.

Oszczapowicz, J. & Czuryłowska, M. (1984). *Talanta*, **7**, 559–560.

Oziminski, W. P. & Krygowski, T. M. (2011). *Tetrahedron*, **67**, 6316–6321.

Pandya, J., Verdia, J. & Joshi, N. (2014). *Afinidad*, **LXXI**, 234–238.

Piltz, R. O. (2018). *J. Appl. Cryst.* **51**, 635–645.

Rádl, S., Stach, J., Havliček, J., Tkadlecová, M. & Plaček, L. (2009). *Acta Chim. Slov.* **56**, 559–565.

Ran, J. & Wong, M. W. (2006). *J. Phys. Chem. A*, **110**, 9702–9709.

Rao, S. N. & Babu, K. S. (2011). *Org. Commun.* **4:4**, 105–111.

SADABS, (2012). *Program for scaling an area detector and correcting the absorption*. Bruker AXS, GmbH, Östliche Rheinbrückenstraße, D-76187 Karlsruhe. V2012/1.

Sadlej-Sosnowska, N. (2001). *J. Org. Chem.* **66**, 8737–8743.

SAINT, (2013). *Program for Integrating Reflections from a CCD Detector*. Bruker AXS, GmbH, Östliche Rheinbrückenstraße, D-76187 Karlsruhe. V8.34A.

Sakaki, S., Kato, K., Miyazaki, T., Musashi, Y., Ohkubo, K., Ihara, H. & Hirayama, C. (1993). *J. Chem. Soc. Faraday Trans.* **89**, 659–664.

Schenk-Joß, K., Bonin, M., Ochsenbein, P., Kieffer, J., El-Hajji, M., Lemée-Cailleau, M.-H. & Mason, S. (2011). *Acta Cryst.*. A**67**, C569.

Seelig, J. (1977). *Quart. Rev. Biophys.* **10(3)**, 353–418.

Shape, (2011). *Program for Drawing a Crystal Morphology*. Shape Software, 521 Hidden Valley Road , Kingsport, TN 37663 USA. V7.3.0.

Sheldrick, G. M. (2015*a*). *Acta Cryst.* C**71**, 3–8.

Sheldrick, G. M. (2015*b*). *Acta Cryst.* A**71**, 3–8.

Skotnicki, M. & Hodgkinson, P. (2022). *Solid State Nucl. Magn. Reson.* **118**, 101783.

Skotnicki, M., Jadach, B., Skotnicka, A., Milanowski, B., Tajber, L., Pyda, M. & Kujawski, J. (2021). *pharmaceutics*, **13**, 118.

van der Sluys, P. & Spek, A. L. (1990). *Acta Crystallogr.* pp. 194–201.

Stepanovs, D. (2013). *Mat. Sci. and Appl. Chemistry; Sci. J. Riga Tech. Univ.* **27**, 99–99. 8th Paul Walden Symposium on Organic Chemistry.

Taulelle, P., Astier, J. P., Hoff, C., Pépe, G. & Veesler, S. (2006). *Chem. Eng. Technol.* **29**, 239–246.

Taulelle, P., Sitja, G., Pépe, G., Garcia, E., Hoff, C. & Veesler, S. (2009). *Crystal Growth & Des.* **9**, 4706–4709.

Tóbiás, R., Császár, A. G., Gyevi-Nagy, L. & Tasi, G. (2018). *J. Comp. Chem.* **39**, 424–437.

Tosco, P., Rolando, B., Fruttero, R., Henchoz, Y., Martel, S., Carrupt, P.-A. & Gasco, A. (2008). *Helv. Chim. Acta*, **91**, 468–482.

Travis, K. P. & Searles, D. J. (2006). *J. Chem. Phys.* **125**, 164501.

Trifonow, R. E. & Ostrovskii, V. A. (2006). *Russian Journal of Organic Chemistry*, **42**, 1585–1605.

Troyanov, S. I., Kosterina, E. V., Loose, A., Reehuis, M. & Kemnitz, E. (2003). *Z. Kristallogr.* **218**, 470–474.

Tsuzuki, S., Uchimaru, T., Matsumura, K., Mikami, M. & Tanabe, K. (2000). *Chem. Phys. Lett.* **319**, 547–554.

Wang, L., Wang, J., Bao, Y. & Li, T. (2007*a*). *J. Chem. Eng. Data*, **52**, 2016–2017.

Wang, L., Zhou, L.-N., Bao, Y. & Wang, J.-K. (2007*b*). *Acta Cryst. E*, **63**, o4933.

Wanjari, P. P., Sangwai, A. V. & Ashbaugh, H. S. (2012). *Phys. Chem. Chem. Phys.* **14**, 2702–2709.

WaveMetrics (2021). Igor Pro 9, Data Analysis and Image Processing Software. WaveMetrics, Inc., Lake Oswego, OR, USA. Version 9.

Wilkinson, C., Khamis, H. W., Stansfield, R. F. D. & McIntyre, G. J. (1988). *Journal of Applied Crystallography*, **21**(5), 471–478. **URL:** *https://doi.org/10.1107/S0021889888005400*

Winther, L. R., (2008). The Phase Transition of DMPG and its Dependence on pH.

Zong, Y. J., Jie, W. C. & Jie, W. X. (2018). *J. Anal. Appl. Pyrolysis*, **134**, 93–101.

Zoumpoulakis, P., Daliani, I., Zervou, M., Kyrikou, I., Siapi, E., Lamprinidis, G., Mikros, E. & Mavromoustakos, T. (2003). *Chem. Phys. Lipids*, **125**, 13–25.